FIBRE BRAGG GRATING FOR MICROWAVE PHOTONICS AND SENSING

Guoyu Yu

DOCTOR OF PHILOSOPHY

ASTON UNIVERSITY

JULY 2002

FIBRE BRAGG GRATING FOR MICROWAVE PHOTONICS AND SENSING

Guoyu Yu

DOCTOR OF PHILOSOPHY

ASTON UNIVERSITY

JULY 2002

ABSTRACT

This thesis presents details on the fabrication of microwave transversal filters using fibre Bragg grating arrays and the building of fibre Bragg grating based magnetic-field sensors. Some theoretical background about fibre Bragg gratings, photosensitivity, fibre Bragg grating sensors and filters are presented. Fibre Bragg grating sensors in other industrial applications are highlighted. Some sensing principles are also introduced. Experimental work is carried out to demonstrate a magnetic-field sensor using an established fibre Bragg grating strain sensor. System performance and trade-off are discussed.

The most important part of this thesis is on the fabrication of photonic transversal filter using fibre Bragg grating arrays. In order to improve the filter performance, a novel tap multiplexing structure is presented. Further improving approaches such as apodisation are also investigated. The basis of nonrecirculating filter, some structure and performance are introduced.

KEY WORDS

Fibre Bragg grating, optical fibre sensor, microwave photonics, photonic transversal filter.

TO MY WIFE

YANPING

AND

TO OUR DAUGHTER

CHUYAN

FOR YOUR SINCERE LOVE AND ENCOURAGEMENT.

ACKNOWLEDGEMENTS

Here I must acknowledge the help from members of the Photonics Research Group at Aston University, especially from my supervisor John Williams for his support throughout this work. I appreciate the very helpful contribution you have provided. Your comments have been very valuable. Acknowledgement also due to Wei Zhang, Lin Zhang and Ian Bennion, they generously give their expertise to me throughout my research. Wei Zhang in particular helped me to cope with the various theoretical and experimental problems during these three years. Special thanks to Bert Biggs who is always a great helped when I need equipment. Many other colleagues in our grating group, Karen, Kate, Lorna also help me a lot. They are all very patient when I disrupt them.

Thanks also due to my colleges of transmission people, Paul, Steve and Des. They are always very generous to give precious ideas and willing to share their equipment.

Last, but certainly not least, I wish to thank my wife, yanping, she take care of my daughter by her own to relieve my burden. You have shown great patience during my thesis writing up. In addition, Mum and Dad have given their great concern for my study.

TABLE OF CONTENTS

TABLE OF FIGURES

1 OVERVIEW

1.1 Prologue

Nowadays, optical fibre has found many applications in various area, such as sensing, medical, illumination [1], signal processing and telecommunication. Especially in telecommunication field, the demand for increased capacity of transmission of information seems unstoppable. Scientists and engineers continuously pursue new technology for achieving this goal. Fibre optic communication systems are capable of carrying enormously large amounts of information due to improvement of optical fibre together with the new invention and development of optical components.

Optical fibre, which acts as the transmission line carrying the light beam loaded with information, is the heart of an optical communication system. The dramatic improvement in the transmission characteristics of optical fibres, including attenuation as well as dispersion characteristics brings about the revolution of fibre optic system.

Fibre Bragg grating (FBG) is such an optical component that facilitates the optical sensing and communications system [2] [3]. Since the side writing technique was invented [4], more and more research interest has been shown, not only for making high performance gratings but also for various applications. For example, chromatic dispersion compensation can be achieved by employing chirped gratings in high-speed optical transmission system [5]. The problem of the signal degradation due to transmission media dispersion arises with the improvement of optical fibre's loss characteristic and the increasing of data transmission speed. Dispersion compensating fibre (DCF) was designed to make up for this detriment. A section of DCF was designed to have dispersion equal to that of the transmission fibre but of opposite sign. The

problem with this scheme is that sufficient length of DCF is needed, make this plan not cost-effective [8].

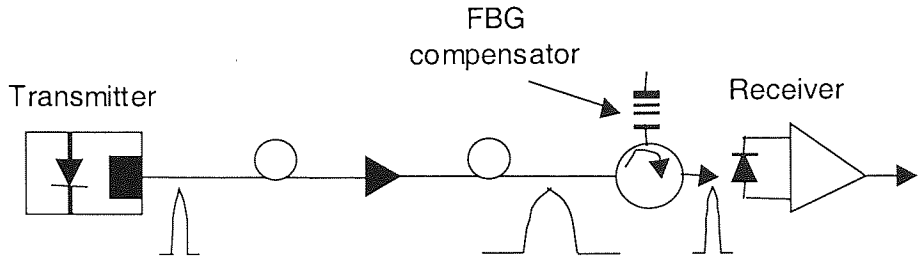

Figure 1- 1. Diagram of dispersion compensation using chirped fibre Bragg grating.

In 1987, Outllette [5] proposed the using of linearly chirped FBG as dispersion compensator. A basic configuration for a dispersion compensator is shown in Figure 1- 1. Here the grating is connected to the fibre link output by means of a low loss optical circulator and must provide a group delay versus signal frequency characteristic opposed in slope to that of the fibre link. In the case of linearly chirped gratings, the grating modulation strength or coupling coefficient must be also varied or apodised along the grating length to avoid significant sidelobes in the grating reflectivity and thus to reduce oscillations in the group delay versus frequency characteristic of the grating [6]. Assuming transmission fibre length to be L_f , having a dispersion of D. $\Delta\lambda$ is the bandwidth of light injecting into this fibre. The group delay generated from this fibre is:

$$\Delta\tau = L_f \cdot D \cdot \Delta\lambda$$

Equation 1- 1

While for a linearly chirped grating with a chirp of C (expressed in nm/m), the group delay is:

$$\Delta\tau = \frac{2 \cdot \Delta\lambda \cdot n_{eff}}{C \cdot c}$$

Equation 1- 2

Where n_{eff} is the fibre core's effective refractive index. c is the light speed in free space. Combining Equation 1- 1 and Equation 1- 2, we derive the length of transmission fibre can be dispersion compensated by a one-metre-long grating with a chirp C:

$$L_f = \frac{2 \cdot n_{eff}}{D \cdot C \cdot c}$$

Equation 1- 3

Assuming that a 10cm grating have a 0.08nm/m chirp. It can compensate for a 0.5nm bandwidth, 1550nm signal transmitting over a standard fibre (D=17ps/nm/km) of 72km.

On the other hand, when a grating is designed to compensate for a dispersion of certain length of fibre, it must be ensured that the grating should be long enough to cover the entire signal spectrum $\Delta\lambda$($\Delta\lambda=L_{grating} \cdot C$). Note that the above conclusions were based on the condition that no grating apodisation is used. But in practice, these gratings used for dispersion compensation are apodised, as mentioned before, so that a slightly longer grating length should be used due to the truncation of grating length arising from grating apodisation.

Add/drop multiplexers can be implemented to add on or dropped signals from Wavelength division multiplexing (WDM) network [7]. WDM system is the leading technology for the next generation high-speed optical fibre systems. In such a system, accessing the individual wavelength channels is necessary. These technologies include arrayed waveguide gratings. This offers an integrated multiple add-drop filter with low dispersion. However it still has many of the disadvantages common to planar technology, such as polarisation dependence and higher insertion loss compared with a fibre approach. There are several schemes been reported on optical add-drop multiplexer (OADM) employing FBG device. The straightforward set-up is as Figure 1- 2.

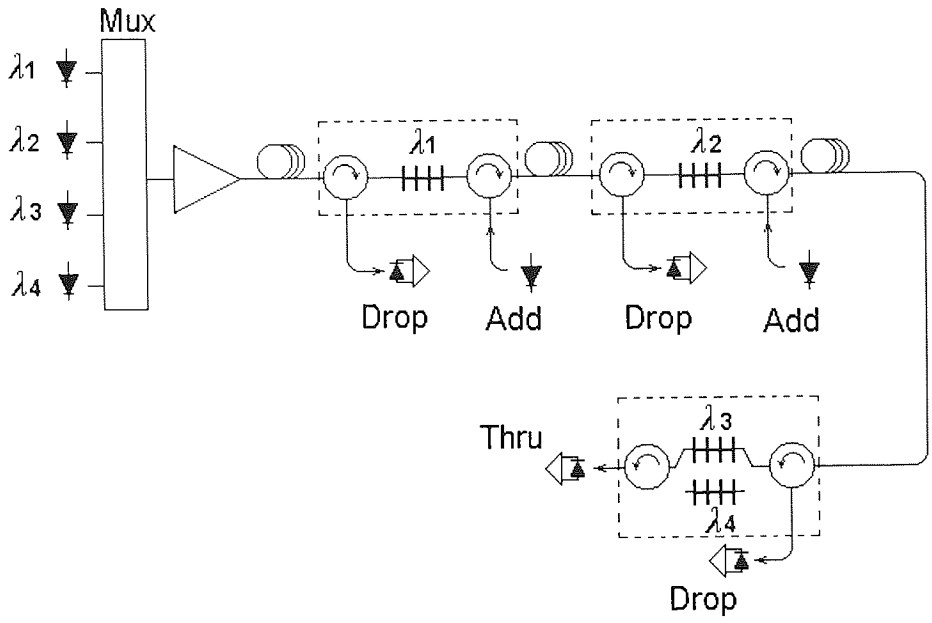

Figure 1- 2. Optical add/drop with the aid of optical circular. ([8]).

This scheme has the advantage of low insertion loss (2 dB for add-drop channels) and highest isolation of the drop and add channels (>50 dB). However, it has economic disadvantage. Each add/drop will need two optical circulators, which is definitely not cost effective.

Another Mach-Zehnder type set-up is shown in Figure 1- 3, two FBG with same wavelength are written in each arm of a Mach-Zehnder structure. For use in drop case (upper picture of Figure 1- 3), the input signal are fed to port one. Signal of wavelength λ_2 is dropped from port 2. Other signals of λ_1, λ_3 and λ_4 exit from port 4. Although avoid using circulators, this structure requires several UV-writing steps to properly balance the gratings and phases in both arms. This is to ensure that in drop case, the dropped signals from each arm are in phase at output. While at add case, the added signal is placed just in the middle of adjacent channels (see lower picture of Figure 1- 3).

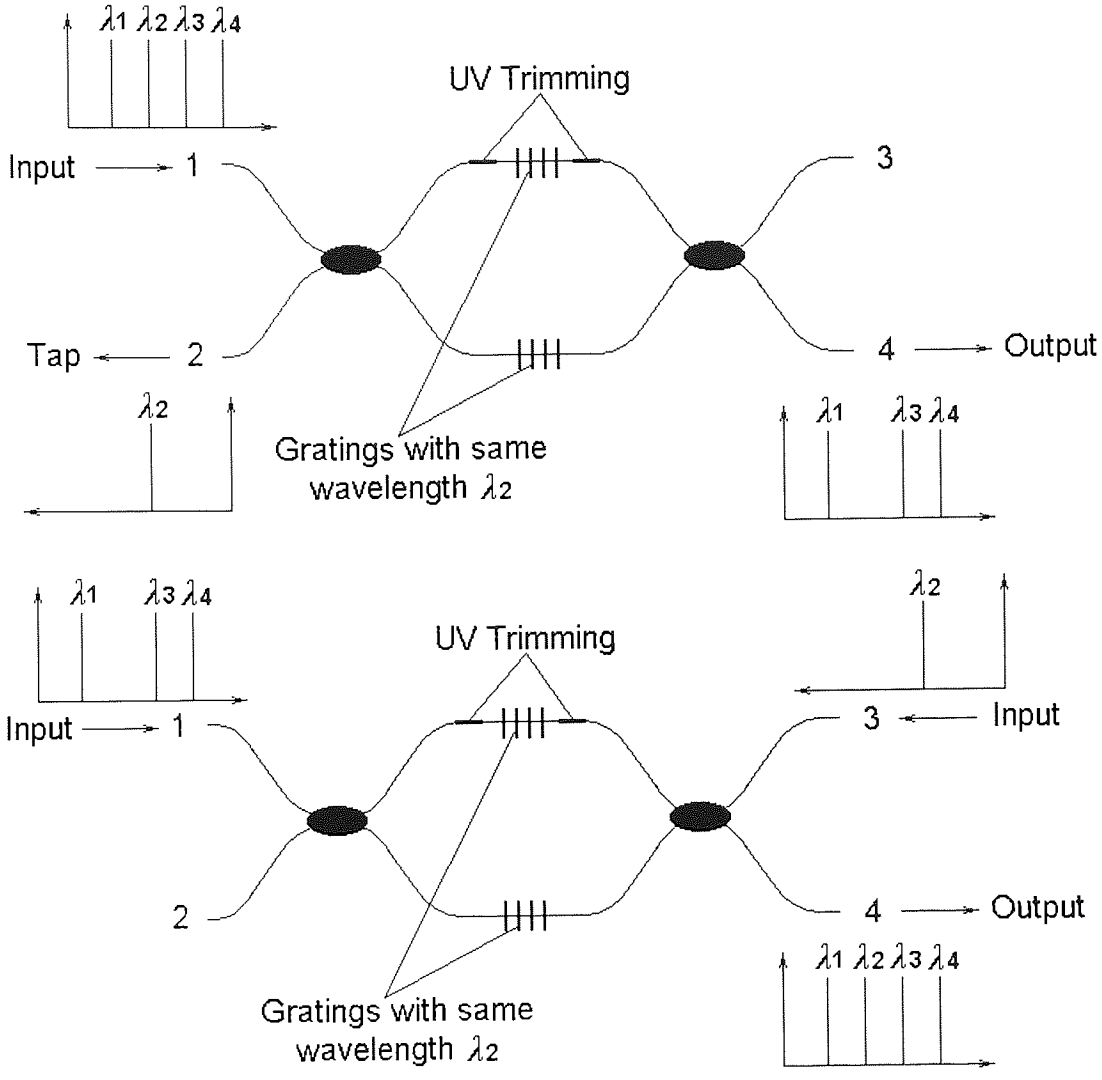

Figure 1- 3. Optical add/drop using Mach-Zehnder structure. ([9])

Another interesting scheme was reported using fused coupler technology, as shown in Figure 1- 4, an OADM is fabricated which is based on a 100% coupler (launched light entirely exits in crossed port) where a strong grating is written in the coupling region. The advantages of this one-coupler device over that two-coupler device are: First, it has low insertion loss. A 100% coupler is used to ensure maximum output. While the two-coupler scheme has a minimum of 6 dB insertion loss due to the use of two 3-dB coupler. Second, this scheme allows easier implementation since it use less branch thus alleviate the UV trimming process.

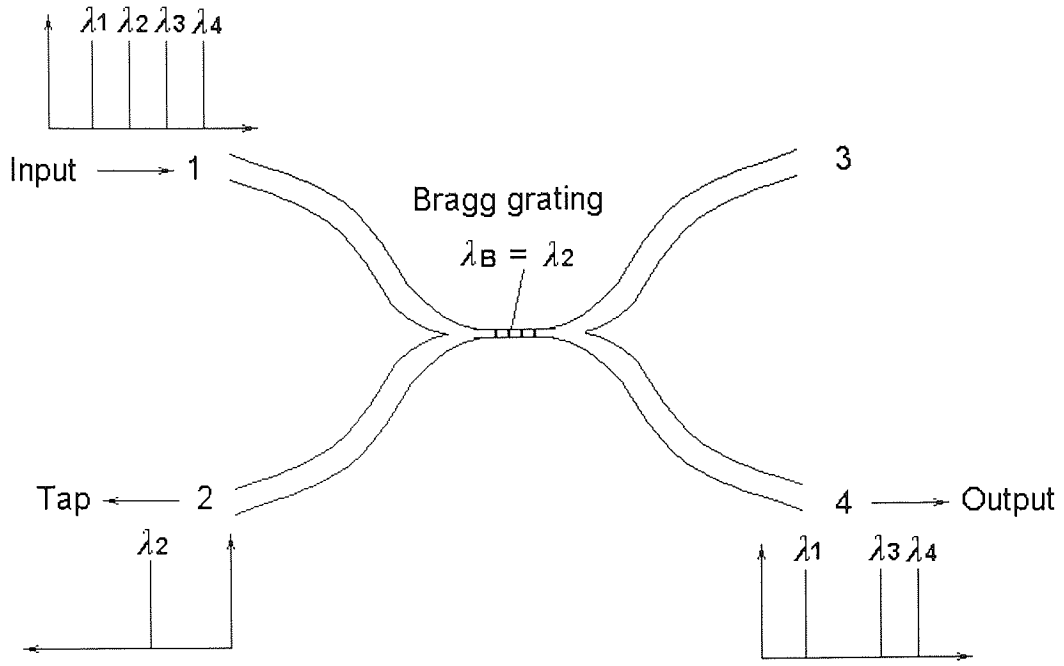

Figure 1- 4. Optical add/drop with fused coupler. ([10])

Next-generation wireless networks also need fibre's transmission capacity in order to grow. The idea is to modulate microwave/millimetre wave signal onto optical carrier. This so-called fibre-radio concept allows the distribution of signals among a large number of base stations and central office over optical fibre. The idea is to keep the signal processing at the central node so that base stations become simple transponders that are small, cheap to produce, and capable of being mounted virtually anywhere. Together with optical wavelength division multiplexing (WDM) technique, the low loss and large bandwidth merit of optical fibre can be exploited. In addition, it will simplifies the distribution of RF signals to provide personal digital cellular service in previously blind area, such as buildings, underground malls and highway tunnels [11]. This is a relatively new and exciting area. Increasing research coming to every aspect to complete this technology, such as photonic beamforming [12], fibre radio networks [11], microwave photonic devices [13], optical generation of microwave and millimetre wave signals [14], microwave photonic signal processing [15] etc. It is worth noticing that several groups have presented microwave photonic signal processing using FBG [16], [17], [18]. This new component brings new solution to this technology.

1.2 Thesis Overview and Aims

This thesis is concerned with mainly the applications of fibre Bragg grating in sensing and microwave photonic systems. The main technological advances presented can be summarised as follows:

- Developing of high-resolution fibre Bragg grating static and dynamic sensing system, static and dynamic magnetic-field sensing system.
- Detailed study of trade-offs involved in these sensing systems.
- Measurement of grating time-delay response. Estimation of RF power degradation in systems employing fibre Bragg grating.
- Development and improvement of high performance fibre Bragg grating based transversal filter.

In Chapter 2, it is firstly, essential to provide some background information on fibre Bragg gratings. A brief description of coupled mode equation of the propagation of light within fibre Bragg grating is presented. Through this, some useful definition and parameters are given. Mechanism of photosensitivity and grating fabrication procedure is also described. Apodisation is included because most high performance gratings need to be apodised to yield better extinction ratio and improved time delay response. This chapter concludes with the introduction of fibre-optic delay-line signal processing which was utilised later on in the work of FBG array based microwave photonic transversal filter.

Chapter 3 focuses on the fibre Bragg grating sensing system. At the beginning, static strain measurements are described in detail. The principles of static sensing, relation between optical path difference of Mach-Zehnder interferometer and source coherence length and thermal drift compensation are addressed. A magnetic-field sensor was developed based on this strain sensor using a magnetostrictive transducer. The magnetostrictive characteristic, mechanical loading of this transducer was also studied since this will bring us a more accurate modelling of this magnetic-field sensor.

Chapter 4 presents in-depth studies of fibre Bragg gratings used in microwave photonic systems. The study of a non-recirculating delay-line filter is the most important aspect of this chapter. From filter reconfiguration to pulse apodisation, improvement of the filter performance was achieved. A novel

scheme of tap multiplexing is introduced. There were some introductions on non-grating-type recirculating filter. The simulations of filter response are given and some discussions are present. In the end of this chapter, suppressed carrier effect is studied.

Chapter 5 provides thesis conclusion, appendices and list of publications.

2 BACKGROUND

2.1 Chapter Overview

The purpose of this chapter is to introduce some background knowledge which are relevant to fibre Bragg Grating (FBG) fabrication, FBG sensor and delay-line filter. In 2.2, equations describing uniform grating's reflection characteristic were derived using couple mode theory. Then grating's time delay and dispersion characteristic were expressed. In section 2.3, photosensitivity was introduced although this mechanism is not fully understood. Following this, FBG fabrication method using holographic and phase mask technique have been introduced. FBG sensors were introduced in 2.5. Last, some basis on delay-line filers was present.

2.2 Basic Grating Theory

A FBG is a periodic perturbation of the refractive index along the fibre length, which is formed by exposure of the core to an intense UV optical interference pattern. The refractive index variation is considered to be:

$$n(z) = n_0\{1 + \sigma(z) + 2h(z)[\cos(2K_0 z + \phi(z)]\}$$

Equation 2-1

where n_0 is the effective average refractive index of fibre core, $h(z)$ describes the amplitude variation of the induced refractive index modulation, $\sigma(z)$ is the background refractive index variation, $K_0=2\pi/\Lambda_0$ is the reference Bragg wavevector (Λ_0 is the reference Bragg period), and $\phi(z)$ is the slowly varying grating phase. For a broadband beam, when incident on the fibre Bragg grating, a number of wavelengths are reflected and all others are transmitted, as shown in Figure 2-1. Typically, uniform grating has a transmission and reflection profile like that shown in Figure 2-2.

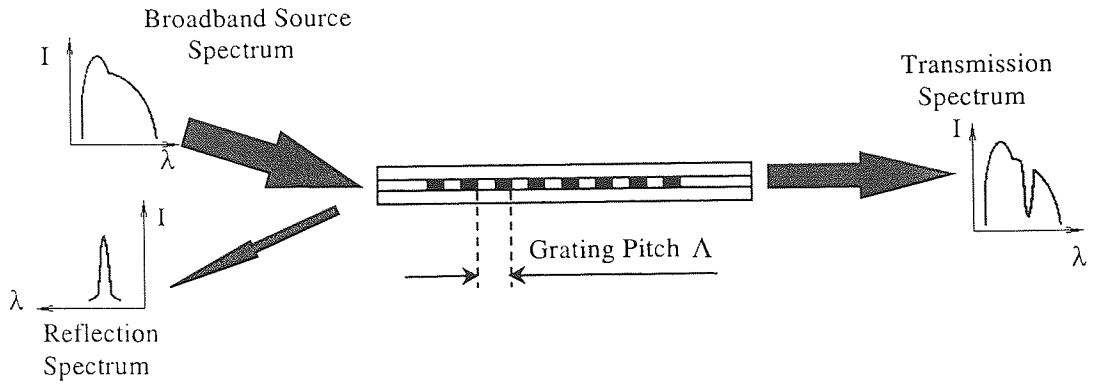

Figure 2-1. Grating reflection and transmission when illuminated by a broadband source.

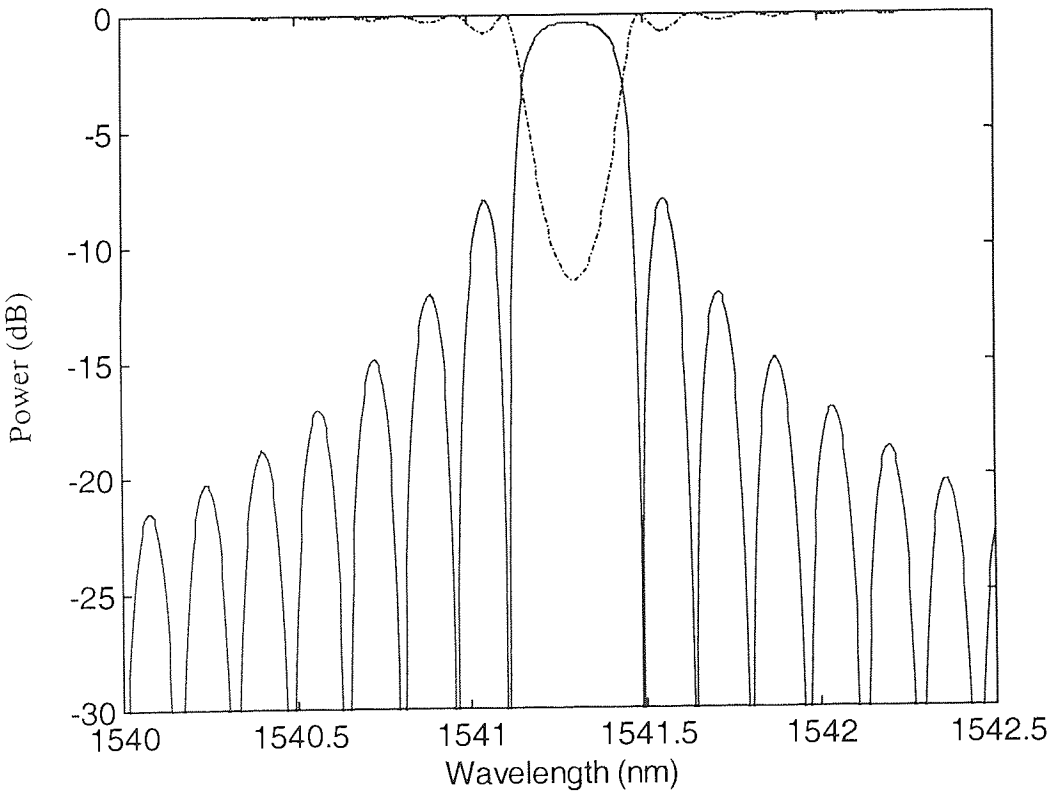

Figure 2-2. Simulation of Spectral profiles of a typical linear grating in transmission (broken line) and reflection (Solid line), (λ_B=1541.3nm, κ=400, L=5 mm) .

The reflection characteristics of a uniform fibre Bragg grating can be calculated using the coupled-mode theory [19] [20]. The electric field distribution along the grating can be expressed in term of two counter-propagating waves as:

$$E(z) = u(z)e^{-i[(\pi/\Lambda_0)z+(1/2)\phi(z)]} + v(z)e^{+i[(\pi/\Lambda_0)z+(1/2)\phi(z)]}$$

Equation 2-2

where $u(z)$ and $v(z)$ are slowly varying amplitudes of the forward and backward travelling waves, respectively. The evolution of the amplitude $u(z)$ and $v(z)$ are described by a set of two coupled differential equations [21],

$$\frac{du(z)}{dz} = [\delta(z)u(z) + \kappa(z)v(z)]$$
$$\frac{dv(z)}{dz} = [\delta(z)v(z) - \kappa(z)u(z)]$$

Equation 2-3

where

$$\delta(z) = \Delta + \frac{\pi}{\Lambda_0}\sigma(z) - \frac{1}{2}\frac{d\phi}{dz}$$

Equation 2-4

$$\kappa(z) = \frac{\pi}{\Lambda_0}h(z)$$

Equation 2-5

$$\Delta = n_0 k_0 - \frac{\pi}{\Lambda_0}$$

Equation 2-6

the parameters Δ and $\delta(z)$ represent the wavenumber detuning from the reference wavenumber π/Λ_0 and the local detuning along the grating, respectively, and $\kappa(z)$ represents the local coupling constant. The boundary conditions of this particular scattering geometry are $u(0)=1$ and $v(L)=0$.

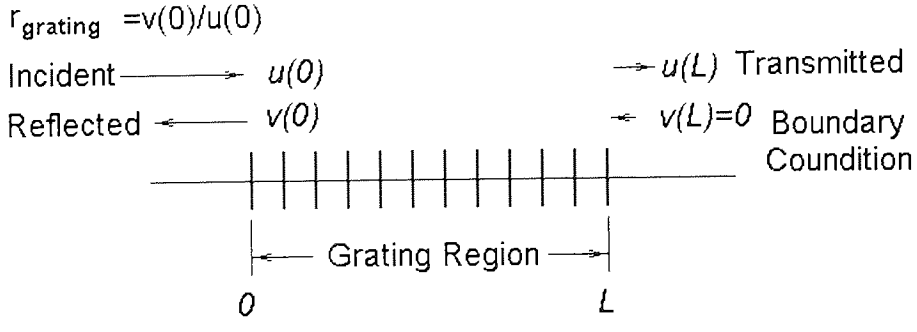

Figure 2-3. Schematic diagram of a single-mode Bragg grating.

To reduce the coupled-mode equations (Equation 2-3) into a single differential equation, we introduce a local reflection coefficient *r(z)* defined as [19]

$$r(z) = \frac{v(z)}{u(z)}$$

Equation 2-7

Differentiating Equation 2-7 and taking into account Equation 2-3 results in a single differential equation, known as *Ricatti* differential equation

$$\frac{dr(z)}{dz} = +i\{(2\delta(z)r(z) + \kappa(z)[1 + r^2(z)]\}$$

Equation 2-8

subject to the boundary condition *r(L)*=0. The quantity of interest is *r(0)*, which corresponds to the total reflection coefficient of the grating. The reflection coefficient of the grating is given by

$$r_E = \frac{E_b}{E_f} = r(0)e^{+i\phi(0)} = |r_E|e^{+i\phi}$$

Equation 2-9

where E_b and E_f are the backward- and forward-propagating electric fields. The grating reflectivity is finally given by

$$R = r_E r_E^* = r(0)r^*(0)$$

Equation 2-10

The solution of these equations is well-established [22]. The reflectance of the grating *R(L,λ)* as a function of wavelength and grating length is given by

$$R(L,\lambda) = \frac{\kappa^2 \sinh^2(SL)}{\delta\beta^2 \sinh^2(SL) + S^2 \cosh^2(SL)} \qquad \kappa^2 > \delta\beta^2$$

Equation 2-11

and

$$R(L,\lambda) = \frac{\kappa^2 \sin^2(QL)}{\delta\beta^2 - \kappa^2 \cos^2(QL)} \qquad \kappa^2 < \delta\beta^2$$

Equation 2-12

where κ is the coupling coefficient, L is the grating length and the mode propagation constant, β, is given by:

$$\beta = 2\pi n_{eff} / \lambda$$

Equation 2-13

where n_{eff} is the mode effective index and λ is the free space wavelength. $\delta\beta$ is a measure of the detuning of the light from the exact Bragg resonance and is expressed as:

$$\delta\beta = \beta - m\pi / \Lambda$$

Equation 2-14

where m is an integer.

The variables S and Q are given respectively by

$$S = (\kappa^2 - \delta\beta^2)^{1/2}$$

Equation 2-15

$$Q = (\delta\beta^2 - \kappa^2)^{1/2}$$

Equation 2-16

The normalised transmission of a grating, assuming no loss is given by $T = 1-R$. The maximum reflection for a uniform grating occurs when $\delta\beta=0$, i.e. the Bragg condition is satisfied,

$$p\lambda = 2n_{eff}\Lambda$$

Equation 2-17

where p is an integer. The strongest interaction is the fundamental Bragg order, i.e. $p=1$, and is the one usually considered. For $\delta\beta=0$ and Equation 2-12 simplify to give a maximum reflectivity of [22].

$$R_{max} = \tanh^2(\kappa L)$$

Equation 2-18

Equation 2-18 indicates that for increasing κL the peak reflectivity of the grating rises to unity, accompanied by an increase in the amplitude of the sidelobes. This is illustrated in Figure 2-4.

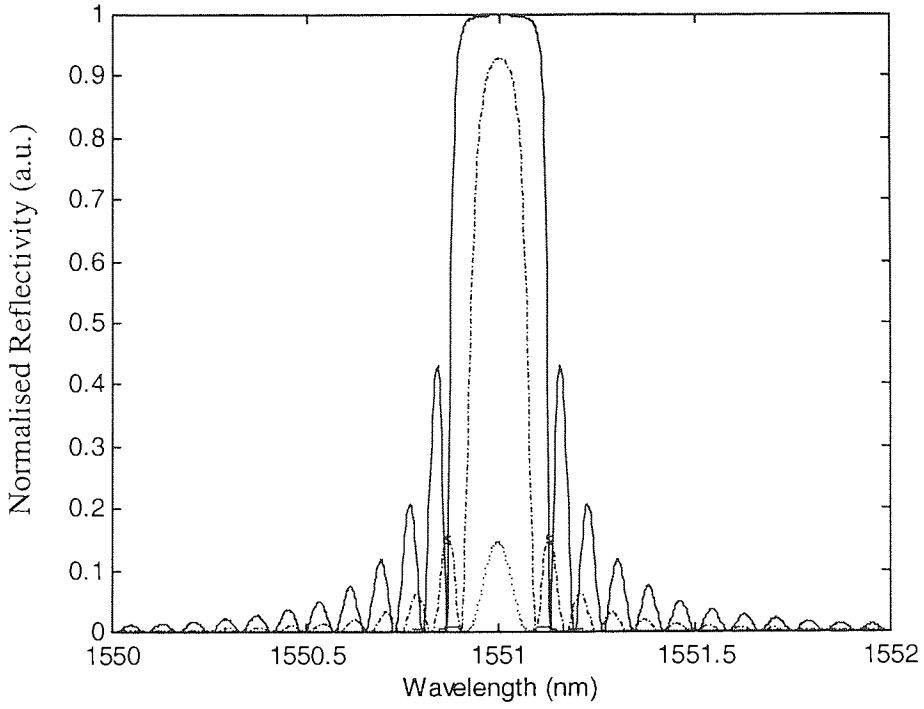

Figure 2-4. Uniform grating reflectivity with κL values of 0.4 (dotted), 2 (dash dotted), 4 (solid).

It follows that the reflectivity of a grating may be increased by manipulation of the coupling coefficient or by writing a longer structure.

The full bandwidth of the grating, $\Delta\lambda$, measured between the zeros on either side of R_{max} is expressed as [22]:

$$\Delta\lambda = \frac{[(\kappa L)^2 + \pi^2]^{1/2}}{\pi n_{eff} L} \lambda_B^{\ 2}$$

Equation 2-19

the full-width half-maximum bandwidth is approximately given by [22]

$$\Delta\lambda_{FWHM} = \lambda_B S\left[(\delta n / 2n_{core})^2 + (\Lambda / L)^2\right]^{1/2}$$

Equation 2-20

where $s \approx 1$ for strong gratings with near 100% reflectivity, $s \approx 0.5$ for weak gratings.

The coupling coefficient, κ, for a uniform sinusoidal modulation of the refractive index throughout the core can be expressed as:

$$\kappa = \frac{\pi \delta n \eta}{\lambda_B}$$

Equation 2-21

where η is the fraction of the fibre mode power contained by the fibre core, i.e. the fraction of light that can interact with the grating. If the grating is written uniformly throughout the core, η can be approximated to [22]:

$$\eta = 1/V^2$$

Equation 2-22

where V is the V-value of the fibre.

Grating phase and time-delay can also be obtained from complex amplitude r. If we denote $\theta_r = phase(r)$, then at a local frequency ω_0 we may expand θ_r in a Taylor series about ω_0. Since the first derivative $d\theta_r/d\omega$ is directly proportional to the frequency ω, this quantity can be identified as a time delay. Thus, the delay time τ_r for light reflected off a grating is [21]:

$$\tau_r = \frac{d\theta_r}{d\omega} = -\frac{\lambda^2}{2\pi c}\frac{d\theta_r}{d\lambda}$$

Equation 2-23

τ_r is usually given in units of nanoseconds. In this equation, λ is the central wavelength of reflected light. c is speed of light. $d\theta/d\lambda$ represents the first derivative of the grating's phase response with relevant to wavelength.

From Figure 2-5, we see that for uniform gratings both the reflectivity and the delay are symmetric about the Bragg wavelength λ_B. it has a minimum value at this Bragg wavelength and increase rapidly around the band edge. The maximum delay appears at the spectral location of the first minima of the grating' s reflection spectrum.

Since the dispersion D_r (in ps/nm) is the rate of change of delay with wavelength, we find

$$D_r = \frac{d\tau_r}{d\lambda} = -\frac{2\pi c}{\lambda^2}\frac{d^2\theta_r}{d\omega^2}$$

Equation 2-24

In a uniform grating, the dispersion is zero near λ_B, and increases rapidly near the band edges and side-lobes of the reflection spectrum (see Figure 2- 6). For wavelengths outside the band-gap, the boundaries of the uniform grating (at

$z=\pm L/2$) act like abrupt interfaces, thus forming a Fabry-Perot-like cavity. The nulls in the reflection spectrum are analogous to Fabry-Perot resonance, that is at these frequencies light is trapped inside the cavity for many round-trips, thus experiencing enhanced delay.

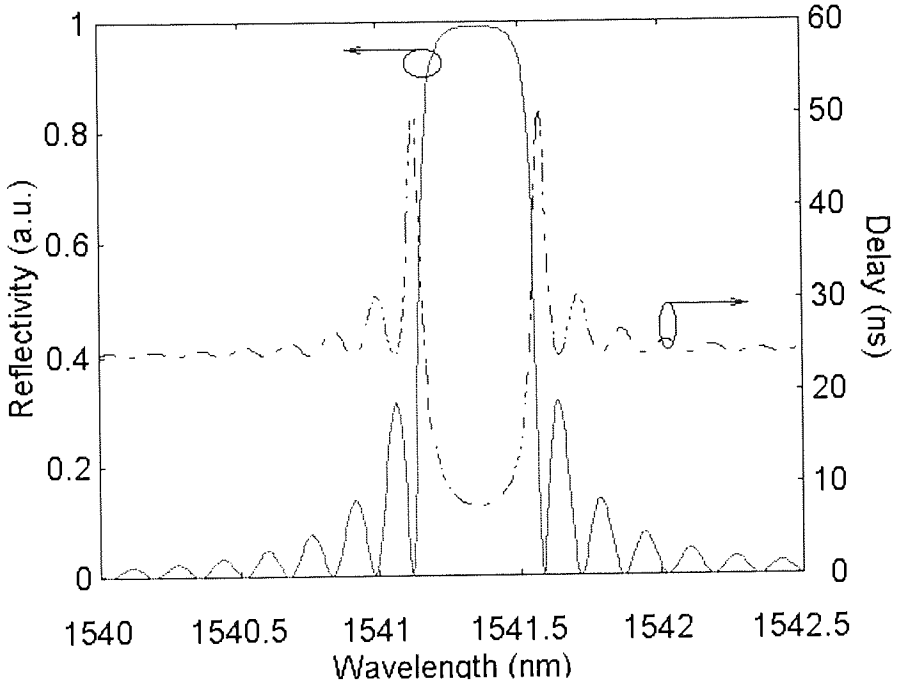

Figure 2-5. Reflection and time-delay spectrum of a uniform fibre Bragg grating.

From the time delay response in Figure 2-5, we realise that grating is a dispersive device. In addition, it was known that dispersive element might limit the system bandwidth by introducing varying delay according to different signal wavelength. This is the case for microwave photonic system using FBG element. The grating's reflectivity and time delay response was used to estimate microwave photonic system bandwidth later in Chapter 4.

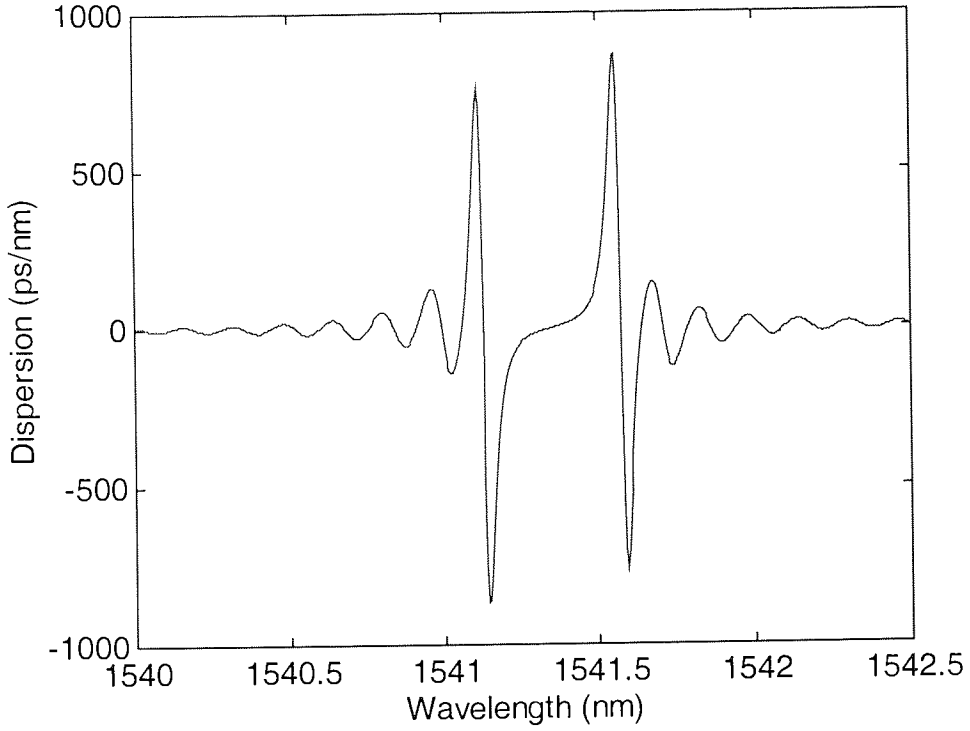

Figure 2- 6. Dispersion of the same fibre Bragg grating as in Figure 2-5.

The above expressions of FBG's reflection, time-delay and dispersion are suitable only for uniformed unapodised gratings. They cannot be applied to chirped gratings. Chirped gratings may be analysed in a number of different ways. These techniques express the grating coupling coefficient and phase as functions of distance along the fibre in a set of couple-mode equations, which are then solved numerically. Solutions have been obtained by (i) reducing these sets of equations to a single *Riccatti* differential equation and (ii) the iteration of a pair of coupled-mode integral equations. An alternative approach involves considering the non-uniform grating as a series of short periodic structures. These smaller devices can then be characterised by different transfer matrices and the overall response is obtained by numerical matrix multiplication [23,24].

A chirped grating has a wider reflection bandwidth than a uniform device. This can be realised by inscribing a structure in which the Bragg condition varies continuously (or quasi-continuously) along its length. The Bragg condition can be expressed as:

$$\lambda_B(z) = 2n_{eff}(z)\Lambda(z)$$

Equation 2-25

Therefore, a chirped structure may be realised by varying either $n_{eff}(z)$ or $\Lambda(z)$ (or both) with position z along the grating. An example of a structure in which the period varies linearly over its length is shown in Figure 2-7. In this case, the shorter wavelength λ_1 is reflected by the leading edge of the grating, whereas λ_2 traverse the structure until being reflected at the far end. Therefore, the longer wavelengths experience an additional time delay with respect to the shorter wavelengths. This delay, τ_D, can be approximated by:

$$\tau_D = \frac{2n_{eff}L}{c\Delta\lambda}$$

Equation 2-26

where $\Delta\lambda$ is the difference between the wavelengths reflected at either end of the grating. This time delay can be utilised to compensate for the effects of fibre dispersion in optical fibre telecommunications systems.

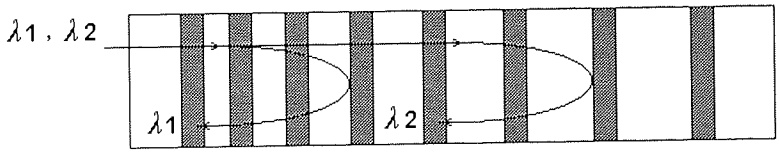

Figure 2-7. Working diagram of chirped fibre Bragg grating.

The same effect can be achieved by linearly varying $n_{eff}(z)$ over the grating length. However, the maximum achievable index change is 2×10^{-3}, this correspond to a wavelength change of 2nm around 1550nm.

2.3 Photosensitivity

Photosensitivity is the essence of fibre Bragg grating fabrication. It is well known that a germanium-doped silica fibre shows photosensitivity. Although the microscopic mechanisms of this photosensitivity are not fully understood, the origin of the photosensitivity utilised for grating-fabrication in germanosilicate fibre lies predominantly with defects associated with oxygen deficiencies in the chemical structure of the fibre. Just like other circumstances in physics, there

were hypothesis suggesting this photosensitivity progress and experimental results supported these guesses.

Hand and Russell [25] explained the index variation in germanosilicate fibres induced by UV light. They reckoned UV light photoionise some defects of the germanosilicate glass. The electrons released from these defects move through the glass matrix and to be trapped at other defect sites. The resultant colour centres are responsible for changes in the UV absorption spectrum of the glass. Several support for this model for the photosensitivity comes from experiments [26,27].

While the colour centre model provides an applicable approximation of photosensitivity observed in H_2 loaded germanosilicate fibres. Another formalism- the densification model [28,29,30] partly explains photosensitivity observed in non-H_2 loaded germanosilicate glasses. It was supported by the transmission electron microscopy (TEM), interferometric microscopy and atomic force microscopy measurement. The amplitudes of the periodic corrugations appearing at the surfaces of these samples in which gratings had been written have been measured. Then Poumellec *et al* assumes that these corrugations result from both permanent and elastic strains [30]. It enables one to calculate the respective contributions of densification and photoelastic effect to the change in the refractive index. Working is still going to resolve the intriguing issue of the associated mechanisms.

Germanosilicate fibres were proven the most photosensitive [31]. Three dynamical behaviours have been observed in germanosilicate fibres. In fibres of low germanium concentration (<10%), the dynamics of the grating inscriptions correspond to type I photosensitivity except for writing at a high intensity [32]. In fibres with a germanium concentration of 20% or higher, type II A photosensitivity is observed for long exposure time. Poignant *et al* [33] have observed that the kinetics of type II A grating growth in a formerly hydrogen loaded fibre could be appreciably increased when the exposure is performed after a time delay of ~10-40 days from the removal of the fibre out of the pressure chamber [33]. Similar enhancement in the kinetics of grating II A growth can be observed when a strain is applied to the fibre at the time of the grating fabrication [34], or when the inscription is performed in a fibre previously annealed at 1100 °C. It is reported that type II A gratings formed in

germanosilicate fibres are much more stable than type I gratings [35]. A type II (damage) grating results even at a low germanium concentration when a high fluence per pulse source (1 pulse at a fluence of ~1 J/cm^2) [32].

Increasing the photosensitivity is an ongoing issue. Germanium-Boron codoped fibre has been demonstrated to be successful in producing large index modulations of the order of 10^{-3} [36]. It has been shown that hydrogen is a good defect former in germanium-doped glass [37]. It was first demonstrated by Ouellette [38] that hot hydrogen-treated fibres have enhanced photosensitivity for second-harmonic generation. Hydrogen has also been shown to permanently increase the photoinduced change in index of the germania-silica system in planar waveguides [39]. Since hydrogen remains chemically bonded within the material using this method, hot hydrogen treatment has the advantage of permanently enhancing fibre photosensitivity. Another technique for increasing photosensitivity of optical fibre is "flame-brushing" [40]. It consists of subjecting the fibre to the flame from a hydrogen-oxygen burner at a temperature up to ~1700°C. At this high temperature, hydrogen diffuses into the core much faster than at room temperature. This treatment renders the fibre permanently photosensitive, similar to the hot hydrogen treatment, and has the advantages of photosensitising the fibre locally. Lemaire *et al* [41] demonstrated an effective photosensitisation method based on high-pressure hydrogen loading. In this method, fibres are soaked in H_2 at a pressure in the range of 20-750 atmospheres and a temperature in the range 20-75°C for a period of several days. Large values of photoinduced Δn (0.01) can be achieved. The dissolved H_2 does not increase absorption at 240nm. It seems that increased photosensitivity derives from UV-initiated reactions of the H_2 with doped glass matrix forming Si-OH groups and oxygen-deficient Ge defects. The UV-induced Δn in H_2 loaded fibres is permanent. Any unreacted hydrogen remaining when UV exposure is completed diffuses back out of the fibre. The presence of unreacted hydrogen temporarily increases the fibre refractive index and thus leads to shifts in the written grating wavelength. However accelerated heating at an appropriate temperature (60°C) for 12 hours can effectively stabilise the grating wavelength.

Some specific applications require germanium-free fibres. For example, gain stabilisation, in which case gain dependence on wavelength is flatter near 1.5 μm in an Er^{3+} aluminosilicate fibre than in the germanosilicate counterpart [42]. Fortunately photosensitivity can be founded in several other rare-earth doped fibres such as Tin [43], Cerium [44], Europium [45] and Tantalum [46]. In addition, oxynitride fibre has been demonstrated photosensitive with exposure to a 193nm-excimer laser [47]. These fibres have the advantage of more resistant to gamma-radiation than germanosilicate fibre [48]. Such benefit can be explored in the application of FBG sensors in hostile environment.

2.4 Fabrication Principles

The formation of photo-generated gratings in germania-doped optical fibre was first reported in 1978 [49]. In the original experiments, the grating was formed by the standing-wave interference pattern set up by counter-propagating beams of light at 488nm or 514.5nm from an argon-ion laser. However the writing efficiency of this method was poor and the written Bragg wavelength was confined to that of the counter-propagating beams. Meltz [50] reported a side-writing technique created a Bragg grating directly in the fibre core using a holographic interferometer illuminated with a coherent ultraviolet source. The UV radiation is split into two equal intensity beams and then recombined to produce an interference pattern within the core, normal to the fibre axis. Focusing the beams on the fibre with a pair of cylindrical lenses can increase the intensity of the pattern. The Bragg wavelength is independent of the writing laser used and the writing efficiency is high [51]. This technique can be used to write both linear and chirped gratings into several types of fibre [22].

2.4.1 Holographic Technique

The first demonstration of this technique was by Meltz *et al* in 1989 [50]. The gratings initially fabricated, using this method, were written into germanosilicate fibre by a frequency doubled tuneable excimer-pumped dye laser operating at 244nm. These initial structures had reflectivities of 50-55% and were about 4.4 mm in length. While these gratings were not particularly strong, the technique offered a way of writing a grating at any given wavelength by exposing the side

of the fibre to the required UV interference pattern. It was also found that this technique was several orders of magnitude more efficient than those outlined by Hill *et al* [49]. A schematic of the holographic set-up is shown in Figure 2-8 (a).

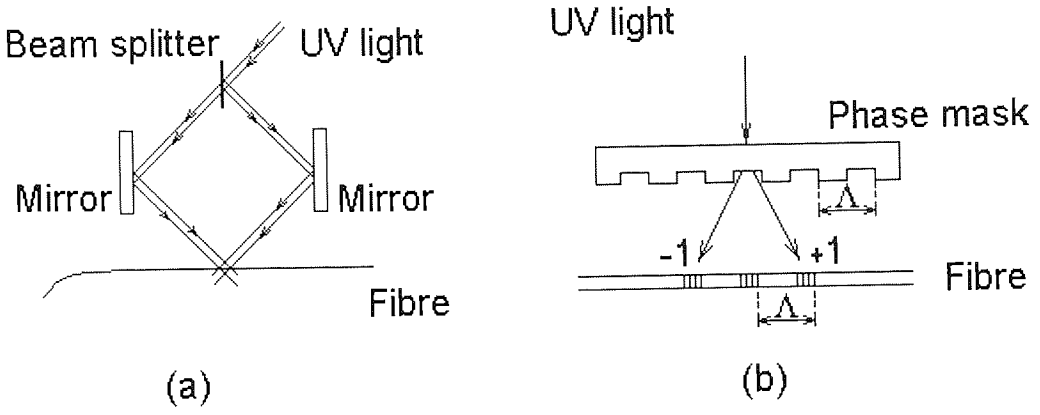

Figure 2-8. Schematic of the side-writing method for inscribing uniform FBGs.

In this experimental arrangement, the output from an UV laser source was split by a 50:50 beam-splitter. These beams are then incident on two mirrors, which were angled such that the laser light would converge at the fibre. Two lenses were employed to focus the beams onto the fibre while an aperture is used to select the central portion of the profile of the beam.

The wavelength at which the light is mostly reflected, i.e. the central wavelength of the grating spectrum, is determined by the period of the structure:

$$\lambda_B = 2n_{eff}\Lambda ,$$

Equation 2-27

where n_{eff} is the effective index of refraction of the fibre core. The period of the device is dependent on the UV writing wavelength (λ_{UV}) and the angle between the two interfering beams [50]. This relationship is expressed by:

$$\Lambda = \lambda_{uv} / 2\sin(\theta / 2)$$

Equation 2-28

where Λ is the period of the photo inscribed FBG, λ_{UV} the writing wavelength and θ is the angle between the two interfering beams.

Therefore, the Bragg wavelength of a structure can be determined by changing the wavelength of the writing beams or the angle between them. It follows that,

for any given inscription method, the easier it is to alter the interference angle between the beams, the more flexible that technique is.

The interference angle can be altered in either of two ways. Small changes may be accomplished by moving the fibre forwards or backwards with respect to the convergence point and then rotating the mirrors to maximise the overlap area on the fibre. Large changes are brought about by varying the distance between the mirrors and the beam splitter, hence varying the interference angle. This latter technique is both stable and simple. It offers excellent flexibility for writing gratings of the highest performance at any given wavelengths.

2.4.2 The Phase Mask Technique

For a number of reasons, this technique has now largely replaced the holographic method, particularly in bulk grating fabrication where reproducibility is a key factor [52,53]. It involves UV exposure through a near-fibre contact phase mask, see Figure 2-8 (b). A phase mask is a length of fused silica, which has had a one-dimensional periodic (Λ_{PM}) surface-relief pattern etched onto it, typically by electron beam lithography. UV light, which is incident normally on the phase mask, passes through it and is diffracted by the periodic corrugations. In practice, light is transmitted into the zero order typically less than 5%. Approximately 40% of the light are diffracted into the ±1 orders. The light from these diffracted orders then interferes to inscribe a grating at a wavelength of:

$$\Lambda = \Lambda_{PM} / 2$$

Equation 2-29

Therefore, the period of the grating is independent of the writing wavelength.

The phase mask writing technique has a number of advantages. It simplifies the fabrication process, yet enable fabrication of good performance gratings. Compared with holography technique, it provides easier alignment, reduced stability requirements on the photo-imprinting apparatus and lower coherence requirements on the laser beam.

The obvious disadvantage to this technique is its written wavelength inflexibility. A separate phase mask is required for each different Bragg wavelength. This limitation can be overcome in several ways. [54, 55, 56].

In previously mentioned techniques, the fibre lies parallel to the phase mask. However, if the UV source has sufficient spatial coherence, it is possible to place one end of the fibre against the mask and the other end at some distance, *r*, away. The inscribed Bragg wavelength is then given by:

$$\lambda_B = 2n\Lambda(1 + r^2 / L^2)^{1/2}$$

Equation 2-30

where Λ is the period of the fibre grating and *L* is the length of the phase mask. This method is suitable for fine-tuning and can alter the written wavelength by approximately 2nm. A pre-strain method can also be used to modify grating pitch. The two ends of fibre are clamped and certain strain is applied. The grating pitch is smaller when the strain is released. Even with the application of these methods, a phase mask is limited to the production of gratings within a fairly fixed wavelength region.

The phase mask technique can also be used to fabricate gratings with very controlled spectral characteristics. For example, the spectral response of a typical uniform grating, as discussed earlier, has secondary side-lobes on both sides of the main reflection peak. This response is undesirable in certain applications such as wavelength division multiplexing. However, if the amplitude of the index modulation along the length of the fibre is given a bell-like functional shape, rather than just being constant, these secondary minima may be suppressed. This procedure of adjusting the amplitude profile of the index modulation is called apodisation. Compared with holographic technique, phase mask method is more suitable for grating apodisation and this has been demonstrated by several reports [57,59,60].

2.4.3 Grating Apodisation

It is already known that the reflection spectrum of an apodised, weak grating follows closely the Fourier transform of the applied apodisation profiles result in enhanced side-lobe suppression and superior grating performance. Various apodisation profiles have been considered theoretically and experimentally in

order to smooth the reflection spectrum and linearise the dispersion characteristics of chirped gratings [57,58]. Also, there are several methods reported for the apodisation of FBG. One involves varying the degree of exposure along the length of FBG [59]. This induces a variation in the average refractive index, thus apodising the FBG profile. This technique allowed the writing of a linearly chirped grating, which had a reflectivity of 40 dB down on its peak reflectivity. This is an improvement of over 20 dB on a unapodised structure with similar bandwidth and peak reflectivity. The disadvantage associated with this technique is that an unwanted chirp results from the uneven of refractive index change along the FBG. Another approach is to introduce longitudinal stretching of the fibre during FBG fabrication [60]. In this way, the grating's fringe visibility at both side of the grating reduces, while the fringe visibility at the centre maintains. In addition, the grating apodisation can be implemented using an apodised phase mask with locally varying diffraction efficiency [61]. This technique has the advantage of good reproducibility.
A phase mask dither technique is used in our lab. It combines the advantages of other techniques without the sacrificing of flexibility. The phase mask is fixed onto a Piezo-transducer and is dithered using a triangle wave. The grating-writing efficiency is related to the degree of phase mask shaking. When the UV beam is scanning at both sides of the gratings, the shaking amplitude is maximum and zero at the grating centre. This technique is simple yet flexible. Different apodisation profiles, such as Gaussian, Truncated Cosine and Raised Cosine apodisation has been used by researcher in our group. In general, with less truncation of the profile, a smaller cut-off at both edges resulted; a sharper function top is produced. However this might unnecessarily truncated gratings (reduce their effective length) and, in some applications, could impose severe limitations in the writing process (e.g., required physical length longer that the available phase mask length or prohibitively long exposure times).

2.5 Fibre optic and FBG sensors

Optical fibre sensor development has been very rapid since it was proposed. In 1977, Bucaro *et al* [62] reported an acoustic sensor. It was a fibre optic interferometric structure illuminated by a laser source. Sensitivities increased

with the length of sensing fibre. This sensor can be built into various geometry, which was its principle advantage.

Together with this acoustic sensor, other fibre optic sensors can be found in reports. Smith *et al* [63] demonstrate a magnetic sensor in 1978. The principle of this sensor is to apply magnetic field longitudinally to a fibre, producing a rotation in the direction of linear polarisation, thus perturb the output intensity. In 1980, Yariv and Winsor [64] reported a magnetic sensor using nickel magnetostrictive transducer which would change its size when it was put into magnetic field, thus stretching the sensing arm of an interferometer. This kind of scheme was demonstrated by Dandridge [65] to have a sensitivity as high as 8×10^{-8} G/m. In 1981, fibre optic gyroscope was reported by Bohm [66]. A single-mode-fibre loop was illuminated by a linear polarised light. The rotation of the loop about its axis results in a phase change between two counter-propagating light beams, which would lead to a rotation dependent intensity output. Other sensors like microbend sensor [67], hydrophone [68], accelerometer [69] were also reported around this time.

The invention of fibre Bragg grating brings about a new family of fibre optic sensor-FBG sensor. Compared with conventional fibre optic sensor, FBG sensor can give absolute measurement due to its wavelength encoding nature. In addition, they are compact in size because long fibre loops are not necessary. Intense research has been carried out since then. Applications have been found in almost every sensing area of conventional fibre optic sensor, such as strain, temperature, magnetic field [70], chemical [71], displacement [72], current [73] etc. Nearly all fibre Bragg grating sensors work on the principle that the measurand induces a change in the Bragg wavelength. A great advantage of Bragg sensors is that they can be used to make distributed measurements, by deploying an array of gratings, of different wavelengths, along a length of fibre. Distributed sensing is now used commercially [74,75] in many applications. A typical one being the measurement of strain in composite structures, where the gratings can be embedded when the structure is made. In the next few sections, FBG sensing principles are introduced and several FBG sensors are highlighted for us to have a concept of FBG sensing and find the difference of their sensing principle from that of fibre optic sensor. They provide

the evidence that FBG sensors will have good commercial value due to their wide application.

2.5.1 Strain Sensing

A strain sensor can be built with a FBG illuminated by a broadband source and interrogation device. Figure 2- 9 (a) shows that a certain portion of source spectrum was reflected when the sensor is intact. While, Figure 2- 9 (b) shows that the reflected beam moved to a longer wavelength if the sensor is subjected to axial extension. The strain response change is due to both the elongations of the sensor and the change in fibre index due to photoelastic effects. The Bragg wavelength shift with strain can be expressed as [12]:

$$\delta\lambda_B = \lambda_B \cdot \xi \cdot \delta\varepsilon$$

Equation 2- 31

where $\delta\varepsilon$ is the applied strain, ξ is the grating's normalised strain responsivity at constant temperature which has a reported value of $0.74 \times 10^{-6}\ \mu\varepsilon^{-1}$ [11]. This responsivity gives a measure of the grating shift with strain of 1nm per 1000 με at 1.3μm. The maximum axial tensile strain that can be measured using Bragg grating is limited by fibre strength. Silica is 23 times stronger under compression than under tension, and wavelength tuning of a single-frequency, erbium-doped, Bragg grating fibre laser over a 32nm range in the erbium fluorescence bandwidth has been achieved through compression tuning of a Bragg grating [76].

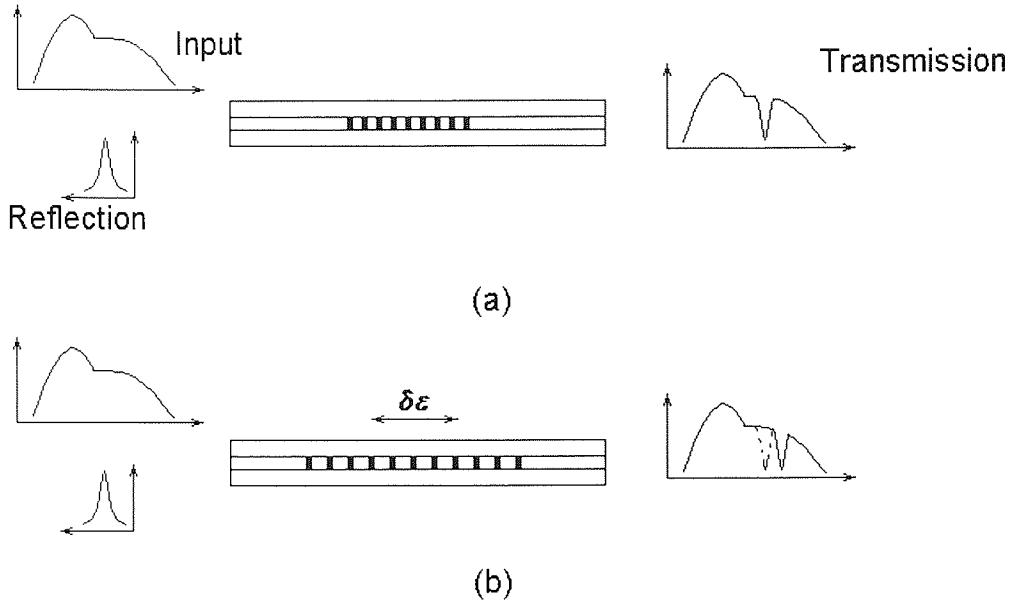

Figure 2- 9. Grating resonance wavelength shift due to strain.

2.5.2 Temperature Sensing

For a temperature change of ΔT, the corresponding wavelength shift $\Delta\lambda_B$ is given by

$$\delta\lambda_B = \lambda_B \cdot \kappa \cdot \delta T$$

Equation 2- 32

The normalised thermal responsivity at constant strain is 6.67 $\times 10^{-6}$ °C^{-1} [14]. A wavelength resolution of ~1pm (0.001 nm) is required (at λ_B~1.3 μm) to resolve a temperature change of ~0.1°C, or a strain change of 1 *μstrain*. Although this wavelength resolution is attainable using laboratory instrument, such as spectrum analysers and tuneable lasers, the ability to resolve changes on this order using small, packaged electro-optics units is a challenge, and this has been the focus of a considerable amount of research work.

2.5.3 Sensor Multiplexing

For various civil structures, such as bridges, highways, dams, buildings and power plants, the cost of replacements and maintenance is very high. The cost due to loss of use will be even more if a structure is damaged prematurely. With such great value in these investments, more and more efforts are made to

monitor and assess the condition of valuable structures, aiming to increase the structure's reliability and lifetime, decrease the cost of maintenance.

Fibre optic sensors find increasing applications in this area. This is mainly due to the formerly described advantages, especially in large part, because of the capability of multiplexing a large number of FBG sensors onto a single fibre for quasi-distributed measurement. In addition, for this purpose, the FBG sensors have great superiority over conventional sensors. FBG sensors of different resonant wavelength are cascaded along a single fibre to perform this distributed measurement. This technique can be found in some reports, such as structural sensing [77,78] and medical sensing [79]. Thus, the development of efficient multiplexing technique can make FBG sensors more competitive than conventional sensors in a broad range.

Generally speaking, the multiplexing techniques used by conventional fibre-optic sensors can also be applied to FBG sensors. A number of multiplexing schemes for FBG sensors, including WDM (wavelength division multiplexing), TDM (time division multiplexing) and their combinations have been reported [80,81,82], in which WDM plays an important role due to the wavelength-encoding feature of FBG.

The mixed use of WDM and TDM has serial and parallel forms. The schematic diagram of serial WDM/TDM multiplexing method is shown in Figure 2- 10 (a). The reflected pulses from each grating reach detector successively. The interrogation device is configured to respond to the reflected signals only during a selected time window, so that a single WDM set of sensors is selected for interrogation.

A similar approach with a high accuracy PZ stretcher has been demonstrated for temperature measurement [83]. The idea is to interrogate sequentially the sensing FBG by tuning the resonance wavelength of a fibre laser. As the line-width of the fibre laser is very narrow, a measurement accuracy of 0.1°C has been achieved.

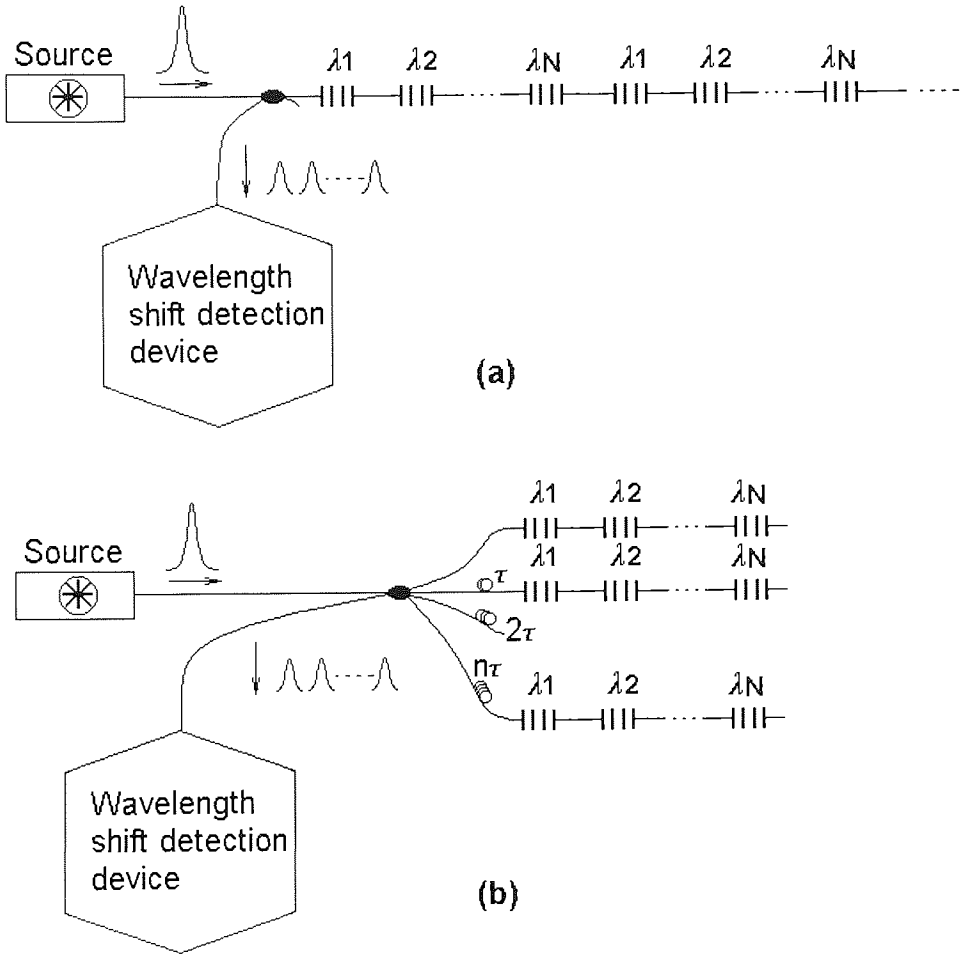

Figure 2- 10. WDM/TDM of FBG sensor. (a) Serial topology (b) Parallel topology.

The serial topology described above has the problem of so-called "Spectral-shadowing cross-talk". It occurs because a downstream FBG's spectrum having to pass twice through an upstream FBG. If the two grating 's centre wavelengths are slightly different (such as the λ_1 gratings in Figure 2- 10 (a)), it appears as though the downstream FBG is shifted in the direction of the actual FBG. Therefore, it causes ambiguity. A simple method allows simultaneous interrogation of all the sensors by matching a receiving FBG to a corresponding sensing FBG with a parallel topology as shown in Figure 2- 10 (b).

2.5.4 Distributed sensing

Distributed sensing are widely explored in smart structure applications. Smart structures are those materials implanted with sensing devices, which can determine the information about the structure. In 1994, Measures *et al* [84]

reported the FBG sensor application for large concrete structures. The scheme is shown in Figure 2- 11. FBG point sensors were distributed on the critical points where subject to heavy strain. The strain information was fed back to central office to obtain the bridge health condition.

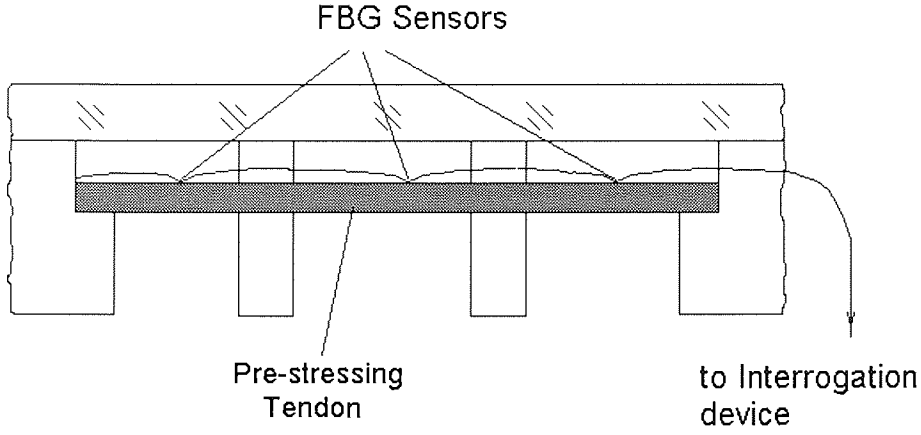

Figure 2- 11. Distributed sensing of a bridge using FBG sensor

Another interesting application is on the electric power transmission. Due to the weather changing, such as heavy snow and strong winds, an extra load on transmission lines may lead to them breaking down. Especially when the lines pass the rural areas, inspection of the line condition is a big problem. Therefore, a distributed measurement system is needed to monitor the changing load on the power line. A multiplexed FBG system with more than 10 sensors distributed over a distance of 30 km has been demonstrated [85].

2.5.5 Hydrophone

A FBG can be used in a hydrophone as Figure 2- 12 [86]. The FBG is used in the transmission mode. Laser light is launched into the FBG and its wavelength tuned to the slope of the transmission spectrum of the FBG. If sound pressure is applied to an FBG fibre, the fibre is physically lengthened or shortened due to the elasticity of the fibre and the refractive index of the fibre is modified because of the photoelasticity. These two physical effects give rise to a change in Bragg reflection wavelength of an FBG. The shift in Bragg reflection wavelength due to the sound pressure is generally small and is considered to be in proportion to the pressure applied. Since the transmission spectrum curve

of the FBG moves without changing its shape as the pressure is applied, the change in transmittance at the laser light wavelength is also considered proportional to the pressure.

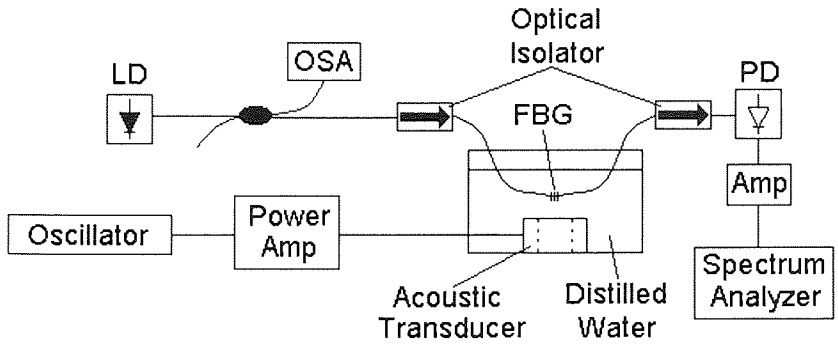

Figure 2- 12. System set-up of a hydrophone using fibre Bragg grating.

2.5.6 Chemical Sensing

Petroleum hydrocarbons are designated as hazardous substances. Their leaks in pipelines and storage tanks are very dangerous, may lead to significant pollution of the environment and even to catastrophic results if are not well detected. Therefore, the development of fibre optic sensors for fast-response sensing of petroleum hydrocarbon leakage is an important objective.

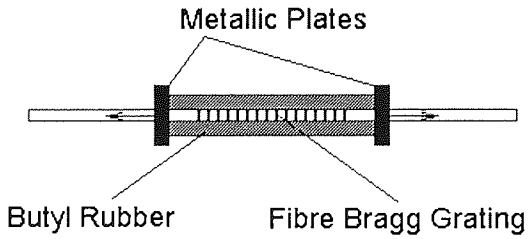

Figure 2- 13. Configuration of FBG based petroleum-leaking sensor.

A fibre Bragg grating chemical sensor has been reported for petroleum hydrocarbon detection [87]. In this work, a FBG is attached to a special polymer, butyl rubber, which expands with petroleum hydrocarbon absorption. The sensor structure is as shown in Figure 2- 13. This force created by the polymer expansion produces an axial strain and shifts the fibre Bragg grating wavelength. In this experiment, a cylindrical sample of the material is placed in a vessel filled by petroleum.

2.5.7 Voltage Sensing

FBG voltage sensing can be achieved based on the inverse piezoelectric effect reached under an applied voltage [88]. The experimental set-up is shown in Figure 2- 14. A ceramic disc is used to produce radial deformation when it is applied a voltage, this deformation provide strain on the sensing grating. An oscilloscope is used to monitor the analogue output of the wavelength demodulation system. The applied voltage is obtained from a high-voltage power supply, and is monitored with an oscilloscope.

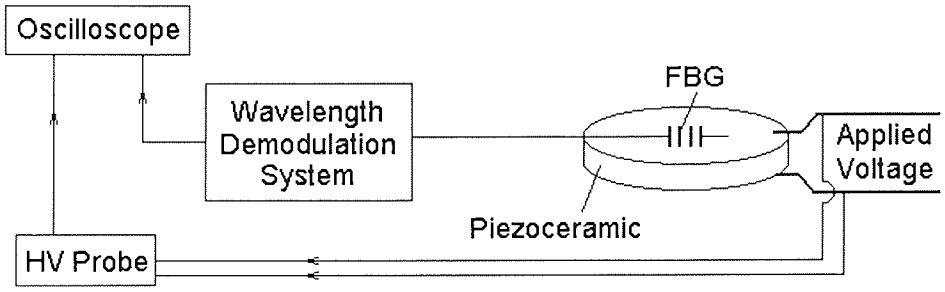

Figure 2- 14. Diagram of high-voltage sensing using FBG sensor.

2.5.8 Corrosion Sensor

There are also reports on the fibre Bragg grating corrosion sensors [89,90,91]. To measure the axial strain in the fibre Bragg grating when the metal coating is corroded by the environment, a preloading on the fibre is performed before a metal film is deposited. The procedures in manufacturing a fibre corrosion sensor that use a single, uniform fibre Bragg grating is shown in Figure 2- 15 (a). Figure 2- 15 (b) shows that this fibre Bragg grating has a preloading on both sides. Subsequently, a metal coating is on the partial section of the fibre Bragg grating as shown in Figure 2- 15 (c). After releasing the preloading, the section with a metal coating will have a residual strain on it. This leaves a free section of Bragg grating, as shown in Figure 2- 15 (d). Finally, the free section is coated (Figure 2- 15 (e)). The principle of this corrosion sensor is that environmental corrosion changes the coating thickness, thus the residual strain inside the metal coating and then the cause a Bragg wavelength shift. The

temperature variation is obtained from the free section so that the environmental temperature effect can be compensated.

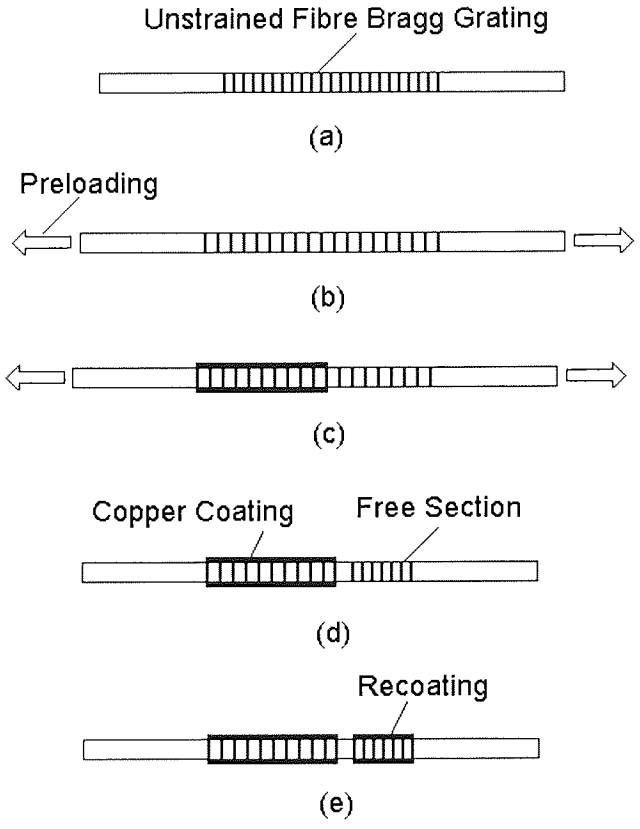

Figure 2- 15. Sensor structure of FBG based corrosion sensor.

2.6 Interrogation Techniques

Interrogation is the precision measurement of the FBG wavelength shift induced by the measurand. This is an important part for achieving good sensor performance. The general requirements for an ideal interrogation method are as follows:

1) High resolution with large measurement range: typically a wavelength-shift detection resolution from sub-picometre to a few picometres for most applications.
2) Cost effective: most of an interrogation system should be compatible with conventional optical or electrical sensors.

3) Compatible with multiplexing: an interrogation scheme should be able to cope with multiplexing topologies, which can make the whole system cost effective.

According to the operating principles of the devices used for wavelength-shift detection, these techniques can be classified as edge filter, tuneable filter and interferometric scanning, which are described in the following sections.

2.6.1 Broadband Filter and Edge Filter

The most straightforward method for interrogation of FBG sensor is based on passive broadband filter as shown in Figure 2- 16 (a). This method is based on the use of a broadband filter, which has a linear relationship between wavelength shifts and the output intensity changes of the filter. By measuring the intensity change, the wavelength shift induced by the measurand is obtained. The measure range is proportional to the detection resolution. A relatively limited sensitivity is obtained using this approach due to the slow rising of the filter transition band. A "sharp" edge filter (Figure 2- 16 (b)) can improve the sensitivity but at the price of decreased measure range.

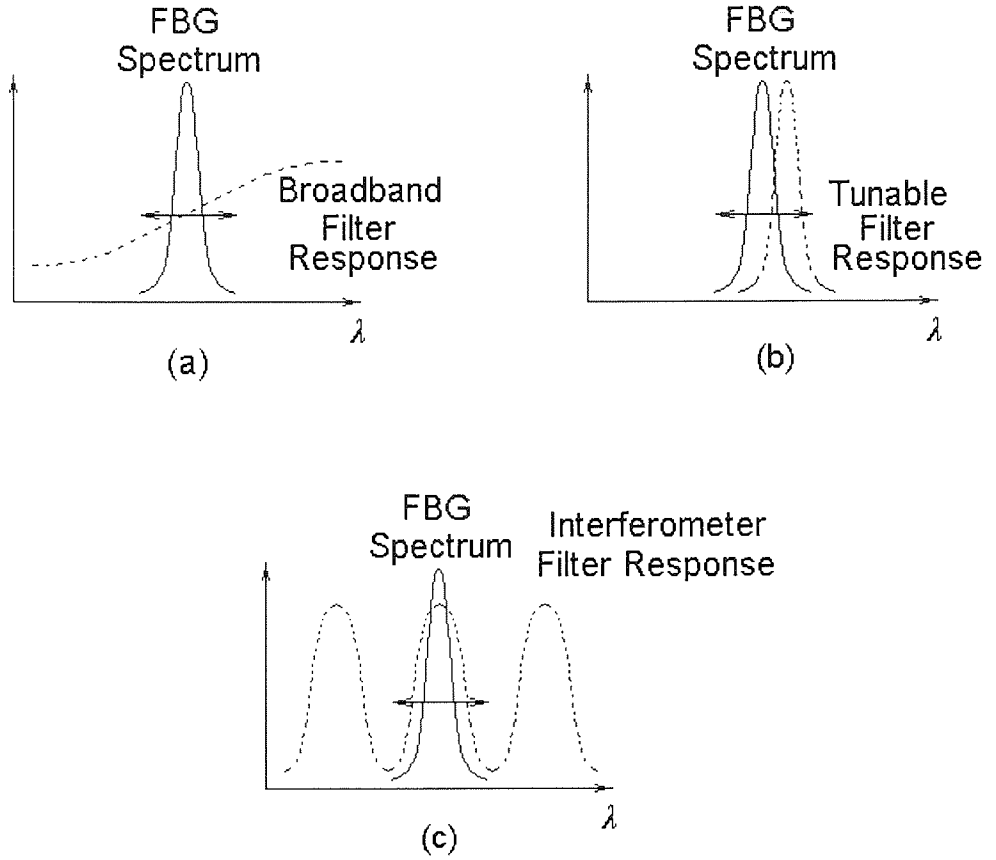

Figure 2- 16. Interrogation principle

A simple interrogation system based on a linear edge filter has been demonstrated for strain measurement [92]. A block diagram of this system is shown in Figure 2- 17. In order to eliminate the influences of intensity fluctuations of the light source and the fibre link, the ratio between the signal intensity, I_F, and the reference intensity, I_R, is used, given by [92]

$$\frac{I_F}{I_R} = A\left(\lambda_B - \lambda_0 + \frac{\Delta\lambda}{\sqrt{\pi}}\right)$$

Equation 2- 33

where A and λ_0 are the gradient and the starting value of the edge filter. λ_B and $\Delta\lambda$ are the Bragg wavelength and the line-width of the FBG respectively. The response of linear edge filter is just like the broken line in Figure 2- 16(a). With strains on sensing FBG, the wavelength of reflected beam will change in either direction. The output intensity is a correlation of the FBG response (solid line in

Figure 2- 16(a)) with that of linear edge filter. This system has several advantages, such as low cost, fast response, and ease of use. A resolution of a few tens of με has been demonstrated with a measurement range of several mε. In order to increase the optical power and hence signal-to-noise ratio, a tuneable fibre laser based on two FBG has been incorporated into this system. A strain resolution of 5 με with a frequency response of 13 kHz has been demonstrated [92].

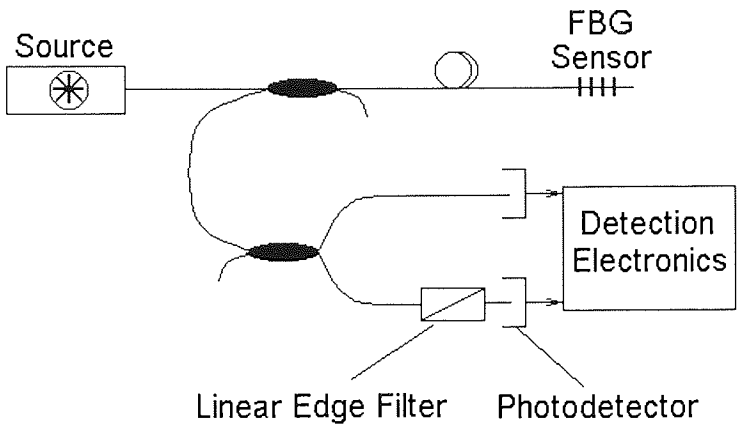

Figure 2- 17. Block diagram of FBG sensing system using edge filter interrogation.

2.6.2 Tuneable Filter

A tuneable filter can be used to measure the wavelength shift of the FBG. The output is a convolution of both the spectrum of the tuneable filter and that of the FBG, as shown in Figure 2- 16 (b). When the spectrum of the tuneable filter matches that of the FBG, the convolution equals one, i.e. a maximum output occurs. By measuring this maximum point and the corresponding wavelength change of the tuneable filter, the wavelength shift of the FBG is obtained. Normally, such an approach has a relatively high resolution.

2.6.3 Interferometric Scanning

A scanned white light interferometer can be used to detect the FBG wavelength shift induced by strain or temperature, see Figure 2- 18. This interferometric method has been demonstrated having high-resolution for dynamic and quasi-static strain measurement [93,94]. The interferometric detection technique is a

filtering method with a raised cosine transfer function whose phase term is dependent upon the input wavelength. In this case, the interferometer output can be modulated through the modulation of the imbalance between the interferometer arms to allow the phase reading technique to be implemented.

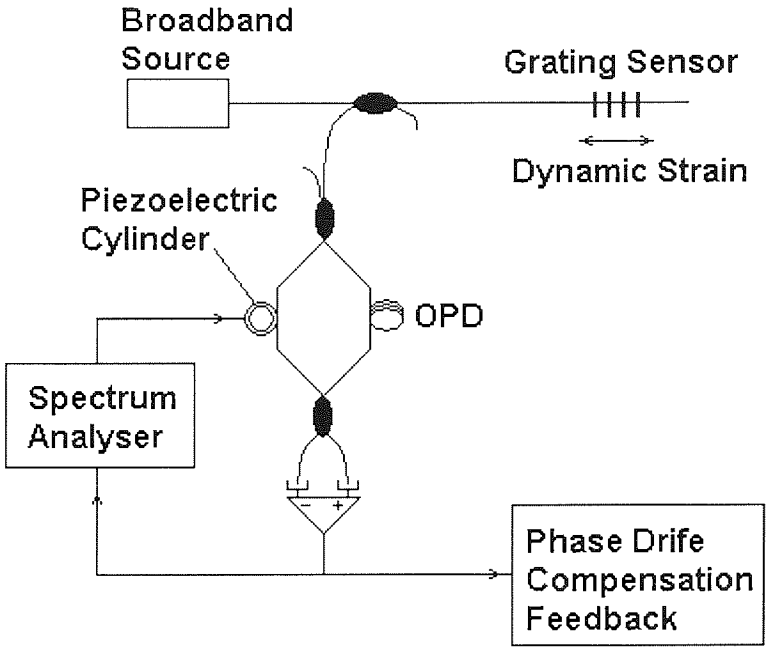

Figure 2- 18. FBG sensor with interferometric interrogation.

Light from a broadband source is coupled to the FBG sensor. The reflected light is tapped off and fed to an unbalanced Mach-Zehnder interferometer. The reflected light becomes the source light into the interferometer and wavelength shifts induced in the FBG sensor resemble a wavelength-modulated source. The unbalanced interferometer behaves as a spectral filter with a raised cosine transfer function. The response of interferometer and sensing FBG is shown in Figure 2- 16 (c). The wavelength dependence on the interferometer output can be expressed as:

$$I(\lambda) = A\{1 + K\cos[\psi(\lambda) + \phi(t)]\}$$

Equation 2- 34

where A is proportional to the input intensity and system losses. K is the interference visibility. $\phi(t)$ represents an environmentally induced phase drift as a result of variation in d and n. d is the length imbalance between Mach-Zehnder interferometer fibre arms. n is the effective refractive index fibre core.

λ is the wavelength of the returned light form the sensor. For a well-shielded fibre interferometer, $\phi(t)$ is a slowly varying random parameter. $\psi(\lambda)$ consists of two parts:

$$\psi(\lambda) = \varphi(\lambda) + \Delta\varphi(\lambda)$$

Equation 2- 35

where

$$\varphi(\lambda) = \frac{2\pi nd}{\lambda}$$

Equation 2- 36

is the aggregate optical phase of the light passing through the interferometer, and

$$\Delta\varphi(\lambda) = \frac{2\pi nd}{\lambda^2}\Delta\lambda = \frac{2\pi nd}{\lambda}\gamma\varepsilon$$

Equation 2- 37

is the added optical phase due to the variation of wavelength, where

$$\gamma = \frac{1}{\lambda}\frac{\Delta\lambda}{\varepsilon}$$

Equation 2- 38

is the normalised strain to wavelength shift responsivity.

Normally phase reading technique is used to ensure high sensitivity detection. A reference grating is used to stabilise the system. A phase metre is employed to compare this constant phase with that from signal of sensing grating.

2.7 Optical Fibre Delay Line Signal Processing

The use of optical fibre to carry microwave and millimetre wave is an ongoing research focus. Many issues to commercialise this technique have been addressed by various research groups. Processing microwave and millimetre wave signal in optical domain is one of these research areas. Fibre-optic delay line structures can perform a wide range of photonic signal processing tasks. This section gives some background on the fibre-optic delay-line filter and their structures.

2.7.1 Basic Concepts

To perform the various signal-processing operations, we need to employ the following elements:

Time Delay

The output is delayed by a unit of time corresponding to the input signal. That is, for a discrete-time input signal *f (k)*, the output is *f (k-1)*; where *k* is an integer. Block diagrams and the impulse response diagrams are shown in Figure 2-19 (a). Note that the Z^{1} inside the block diagram represents a unit time delay. Fibre lengths provide precise time delays that can be used to perform the time-delay function. Assuming a refractive index of about 1.5 for the fibre, the propagation delay is about 5 ns/m.

Tapping

Tapping is splitting a portion of input signal from its main streams. Various mechanisms, such as directional couplers or bends, can be used to accomplish tapping. The output of tapping element is a constant multiple, *K,* of the input. See Figure 2-19 (b).

Time Advance

Opposite to time delay, time advance is to advance the output signal one unit of time than input signal (see Figure 2-19 (c)). Note that this element has only mathematical meaning.

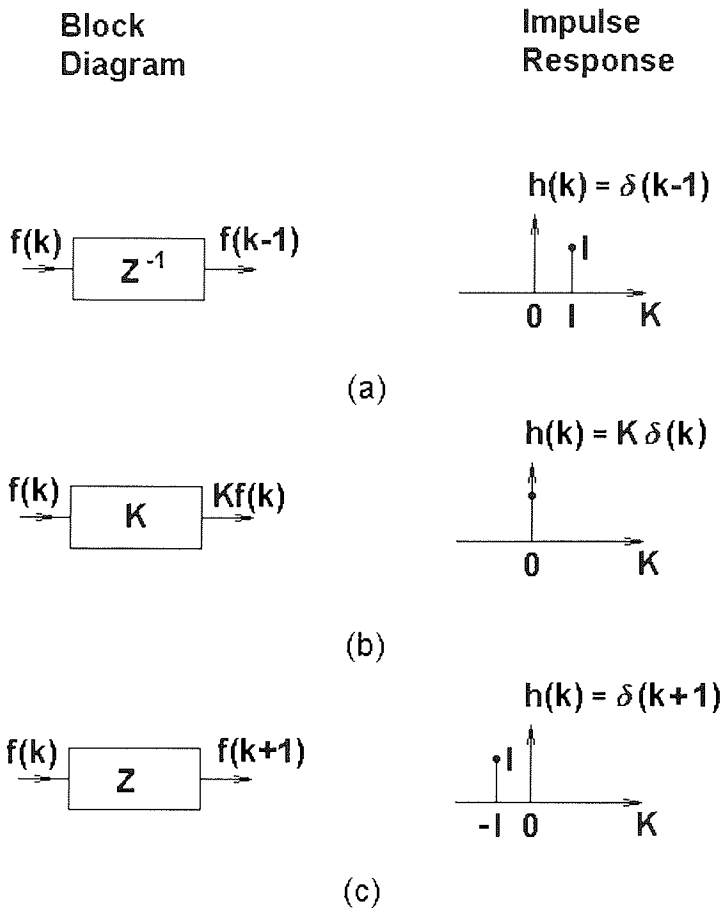

Figure 2-19. Elementary concepts for signal processing. (a) Time-delay element. (b) Tapping element. (c) Time-advance element.

Summing Element

A summing element adds incoming signals together (Figure 2-20 (a)). A directional coupler can be used to do the summing operation.

Branching Element

A branching element split the incoming signal into several parts (Figure 2-20 (b)). Optical 1xN splitter can be used to perform branching.

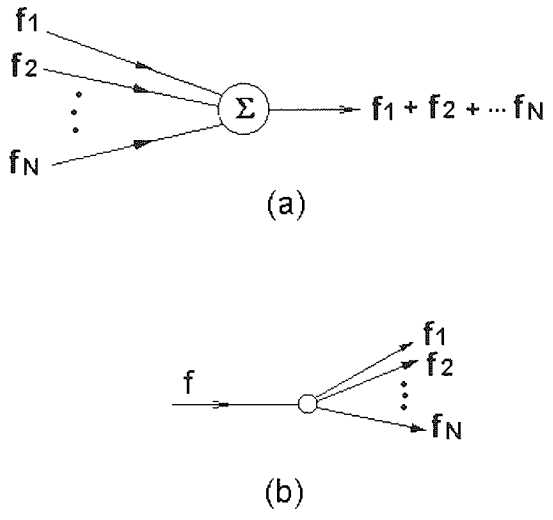

Figure 2-20. Summing and branching elements. (a) Summing element. (b) Branching element.

2.7.2 Signal flow chart

In order to analyse complex fibre optic system, a graphical approach can be used [95,96]. This method has been adapted from signal-flow charts for electrical systems. Here optical components are drawn in signal-flow charts and represented in planar form in which there are no crossings between the signal-flow paths, thus allowing us to apply Mason's Law to fibre optic system.

Mason's law

The characteristic of microwave signal is mainly determined by the interference of microwave signal and optical carrier inside the fibre optic transmission line. In order to obtain accurate analytical solution, a rigorous theoretical analysis must be able to describe the input-output relationship of the modulated optical fields. The main difficulty of this analysis is its high degree of complexity when dealing with large-scale optical structures such as ladder networks. A more suitable method is frequency domain analysis based on the S-matrix concept. However, the spectral distribution of the optical source must be considered in order to calculate the output optical power reaching the photodetector.

Optical networks are an extension of traditional microwave circuits and it is possible to use the electrical S-parameters theory in the optical regime. However, some specific aspects should be noticed in optical networks, for example the polarisation and the coherent properties of the optical signal. Using the S-matrix method, we assumed that the signal is perfectly coherent. However, as we know standard single-mode-fibre support two polarisation state and there may exist power coupling inside optical components.

Accurate analysis is necessary when optical carrier interference can take effect. In the case of incoherent optical signal processing networks, the microwave behaviour is dependent only on microwave envelope interference effects. So the analysis can be greatly simplified by using signal flow chart method and we need consider only the propagation of light intensities inside the network rather than optical fields. As for the basic optical components such as optical couplers and fibres, we can take them as bulk elements. The input-output relations can be determined using only intensity expressions. Thus, the signal flow chart technique can be used very conveniently to obtain the microwave transfer function.

The two basic optical components of fibre delay line structure are the single mode optical coupler and the optical fibre. The intensity input-output relationship of a symmetric optical coupler is a 2×2 matrix given as

$$\begin{bmatrix} I_3 \\ I_4 \end{bmatrix} = \gamma \begin{bmatrix} 1-\kappa & \kappa \\ \kappa & 1-\kappa \end{bmatrix} \begin{bmatrix} I_1 \\ I_2 \end{bmatrix}$$

Equation 2- 39

where γ represents the total loss and κ is the intensity coupling coefficient. For a relatively short length of single-mode optical fibre, they can be considered no loss and dispersion. Thus, the modulated optical signal, which propagates through the fibre, will suffer only a phase shift

$$I_{out} = I_{in} e^{-j\beta L}$$

Equation 2- 40

A linear optical transfer function H_{jk} between the node j and the node k in the photonic signal-flow chart can be obtained using Mason's law [95]. According to Mason's law the transfer function between two nodes in the signal-flow chart is given by

$$H_{jk} = \frac{\sum_i^N P_{jk_i} \Delta_{jk_i}}{\Delta}$$

Equation 2- 41

Where N is the total number of possible optical transmission paths from optical node j to node k, P_{jki} is the optical transmittance of the ith path from node j to node k in the signal-flow chart, p_{mr} is the mth possible product of r nontouching optical loop gains, and Δ is given by

$$\begin{aligned}\Delta &= 1-\left(-1^{r+1}\right)\sum_m\sum_r P_{mr} \\ &= 1-\sum_m P_{m1}+\sum_m P_{m2}-\sum_m P_{m3}+\cdots \\ &= 1-(sum\ of\ all\ optical\ loop\ gains) \\ &\quad +(sum\ of\ all\ gain\ products\ of\ two\ nontouching\ optical\ loop) \\ &\quad -(sum\ of\ all\ gain\ products\ of\ three\ nontouching\ optical\ loop) \\ &\quad +\cdots\end{aligned}$$

Equation 2- 42

With $\Delta_{jki}=\Delta$ evaluated with all optical loops touching P_{jki} removed.

Δ is the graph determinant and Δ_{jki} is the cofactor of the *ith* forward transmittance path. An optical loop is a closed optical transmittance path in which the nodes can only be touched once per traversal. Lightwaves in a loop must be travelling in only one direction. Two loops are considered to be nontouching if they do not have any common nodes.

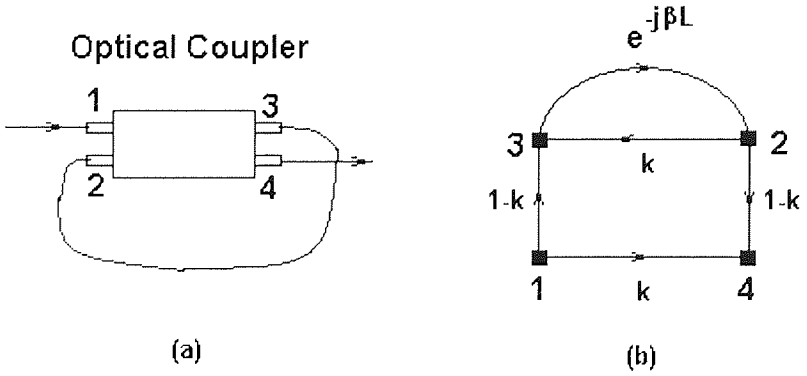

Figure 2- 21. A recirculate optical coupler and its corresponding signal flow chart.

As an example of this signal flow chart method, we analysis a recirculate optical coupler. The schematic diagram and its signal flow chart are shown in Figure 2-21.

First, we find the optical paths. There are altogether two paths from input node 1 to output node 4. They are listed as following:

$$P_1 = (1)(4) = k$$
$$P_2 = (1)(3)(2)(4) = (1-k)^2 e^{-j\beta L}$$

Equation 2- 43

There is only one optical loop is this structure. It is:

$$L_1 = (3)(2)(3) = ke^{-j\beta L}$$

Equation 2- 44

The determinant of this graph can be decided as:

$$\Delta = 1 - ke^{-j\beta L}$$

Equation 2- 45

The cofactors of each path can be derived as below:

$$\Delta_1 = \Delta \quad (path1\ doesn't\ touch\ the\ loop)$$
$$\Delta_2 = 1 \quad (path2\ touch\ the\ only\ loop)$$

Equation 2- 46

reporting Equation 2- 43 to Equation 2- 46 into Equation 2- 41, We can get the following transfer function:

$$H(\omega_{RF}) = \frac{k + (1-2k)\exp(-j\beta L)}{1 - k\exp(-j\beta L)}$$

Equation 2- 47

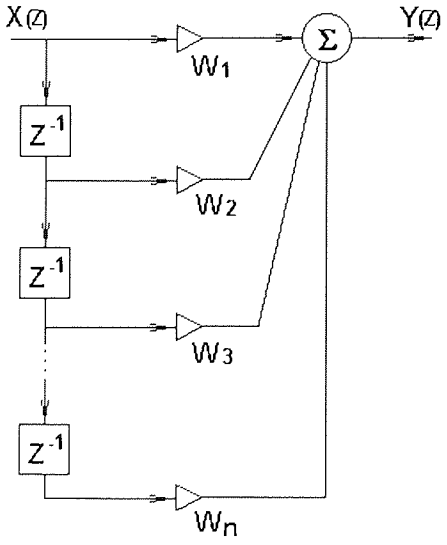

Figure 2- 22. Signal flow chart of a transversal filter.

Now we turn our attention to a transversal filter whose signal flow chart is shown in Figure 2- 22. The optical paths are:

$$P_1 = w_1 Z^0$$
$$P_2 = w_2 Z^{-1}$$
$$\cdots$$
$$P_N = w_N Z^{N-1}$$

Equation 2- 48

There is no loop in this filter. Therefore, the determinant Δ of this graph is 1. Applying Mason's law as in Equation 2- 41. We can obtain the following transversal filter transfer function:

$$H(z) = \sum_{n=0}^{N-1} W_n Z^{-n}$$

Equation 2- 49

As we have know that Z^{-1} represents a unit delay. In this microwave photonic system:

$$Z^{-1} = e^{-j\beta L}$$

Equation 2- 50

Where β is the propagation constant and equals to $(2\pi/\lambda)n$. L is the unit delay length. Therefore, we can derive the following expressions:

$$\beta L = \frac{2\pi n}{\lambda} L$$

Equation 2- 51

Considering that λ=c/f, we obtain the following expression:

$$\beta L = 2\pi f \left(\frac{nL}{c} \right)$$

Equation 2- 52

nL/c =T =1/f_s, f_s represents sampling frequency. So we get:

$$Z^{-1} = e^{j2\pi(f/f_s)}$$

Equation 2- 53

Substituting Equation 2- 53 into Equation 2- 49, we acquire the following transversal filter transfer function:

$$Y(z) = \sum_{n=1}^{N} W_n e^{j2\pi L_n (f/f_s)}$$

Equation 2- 54

Equation 2- 54 is the fundamental of our FBG type transversal filter. All the filter frequency response simulation is based on this equation.

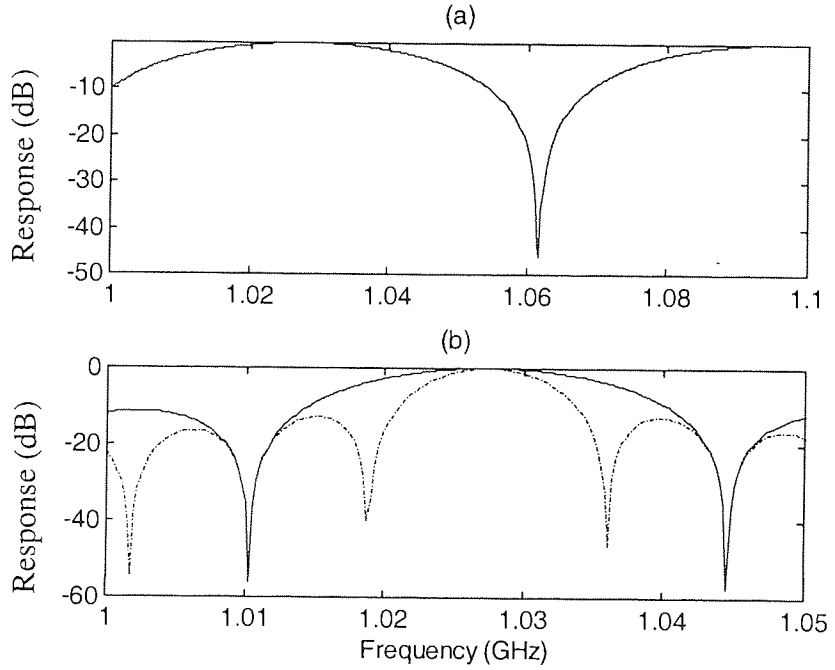

Figure 2- 23. Filter frequency response with (a) two taps and (b) four taps (solid line), eight taps (broken line). The unit delay length is 2.8m.

We can see some of the simulation results from Equation 2- 54. As shown in Figure 2- 23. The simulation was performed using Matlab software. The code can be found in Appendix B. First we assign a vector of frequency range from 1 GHz to 1.2 GHz. Then we set unit delay length to be 3 metres. The frequency response was derived after the running of this program and we plot frequency response against frequency. Then we can zoom in to achieve more detail. When the filter has only two taps, the filter frequency response has very broad passbands (36.5 MHz in this instance), and very large dip in-between (over 50 dB). It is obvious that this filter can be used as notch filter to perform band rejection. When the number of taps is increased, as in (b) of Figure 2- 23, the passbands become narrower and sidelobes appear. So this structure can be used as a bandpass filter.

2.7.3 Basic Fibre-Optic Filter Structures

Basic recirculating and nonrecirculating fibre-optic delay-line filter structures are introduced in this section. Complicated higher order filter are usually consists of basic recirculating and nonrecirculating delay-line filters, which make use of basic elements such as time delay and branching described above. FBG can also be used to build recirculating and nonrecirculating filters and they have several advantages over fibre-optic filters originate from their wavelength encoding nature. More detailed discussion of these structures will be given in the following sections.

Recirculating Delay Line Filter

The fibre type recirculating delay line filter consists of a splitter and a loop of fibre to feedback part of the signal around (see Figure 2-24 (a)). Signals injected into the filter recirculate around the loop giving outputs on each transmission. The unit delay length is equal to the length of fibre loop. The splitting ratio of the coupler controls the portion of light to be feedback. The frequency response of this filter was derived using Mason's law [96], as shown in Equation 2- 47. The length of optical fibre loop L determines the free spectral range (FSR) of this filter. A simulation of Equation 2- 47 using different optical loop length is shown in Figure 2- 25. We can see that a longer optical loop length brings a shorter FSR.

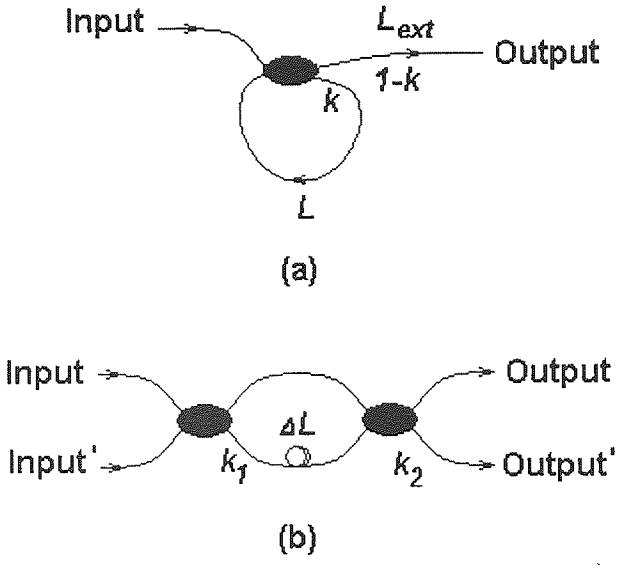

Figure 2-24. Basic delay-line structures: (a) recirculating delay line with delay T and (b) tapped delay line with tap intervals T=ΔL*n/c.

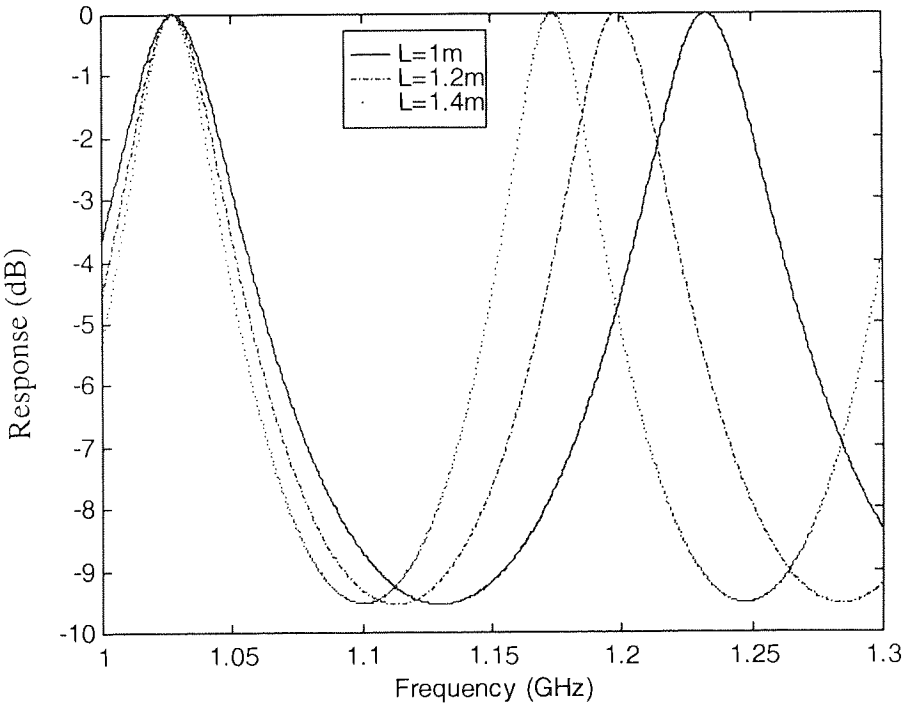

Figure 2- 25. Filter frequency when using different optical loop length.

The filter's extinction ratio is determined by the coupler's splitting ratio κ. As we can see in Figure 2- 26, when the splitting ratio is more than 0.5, the filter has

less extinction ratio. When the coupler's splitting ratio is less than 0.5, the filter has a narrower rejection band and can be used as a band-rejection filter.

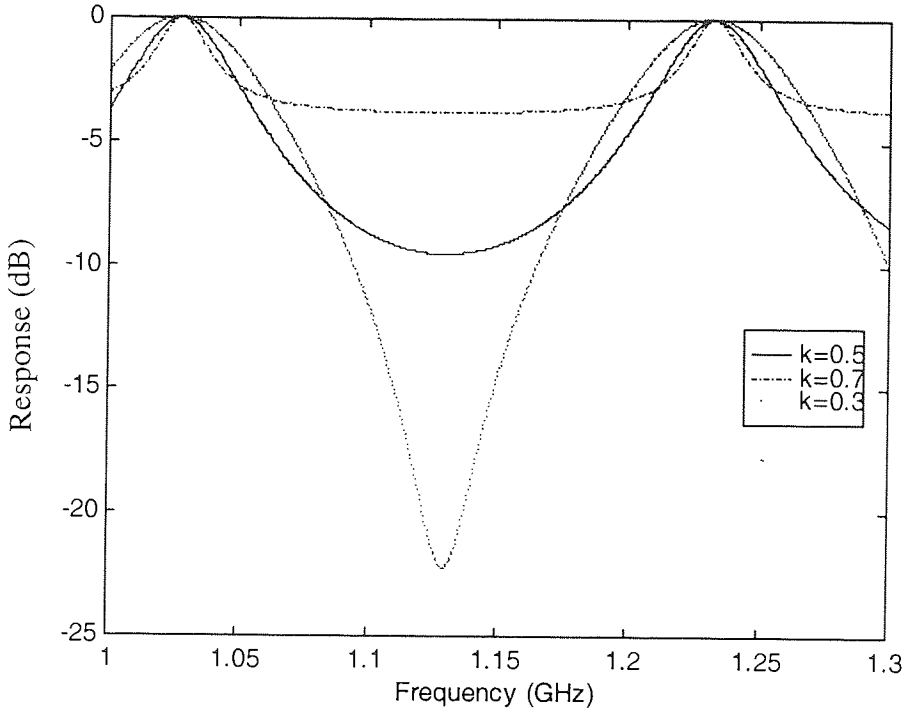

Figure 2- 26. Filter frequency response showing different filter extinction ratio when the coupler is assigned different splitting ratio.

Nonrecirculating Delay Line Filter

The nonrecirculating (tapped) delay-line structure consists of a fibre which has taps distributed along its length. Each tap has an incremental length of fibre. Signals injected into one end of the filter are successively sampled, weighted, and summed. The tapping can be achieved using directional couplers. An example as shown in Figure 2-24 (b), this nonrecirculating filter is made of two directional couplers. The outputs of the first coupler are sent to the second coupler where they are combined after a time-delay T, that is the delay-time difference ΔL between the two feed-forward fibre lines. The frequency response of this structure can be expressed as [96]:

$$H = \exp(-j\beta L_{ext})\left[(1-k_1)(1-k_2)\exp(-j\beta\Delta L)+k_1 k\right]$$

Equation 2- 55

Some simulation results can be seen in Figure 2- 27 and Figure 2- 28.

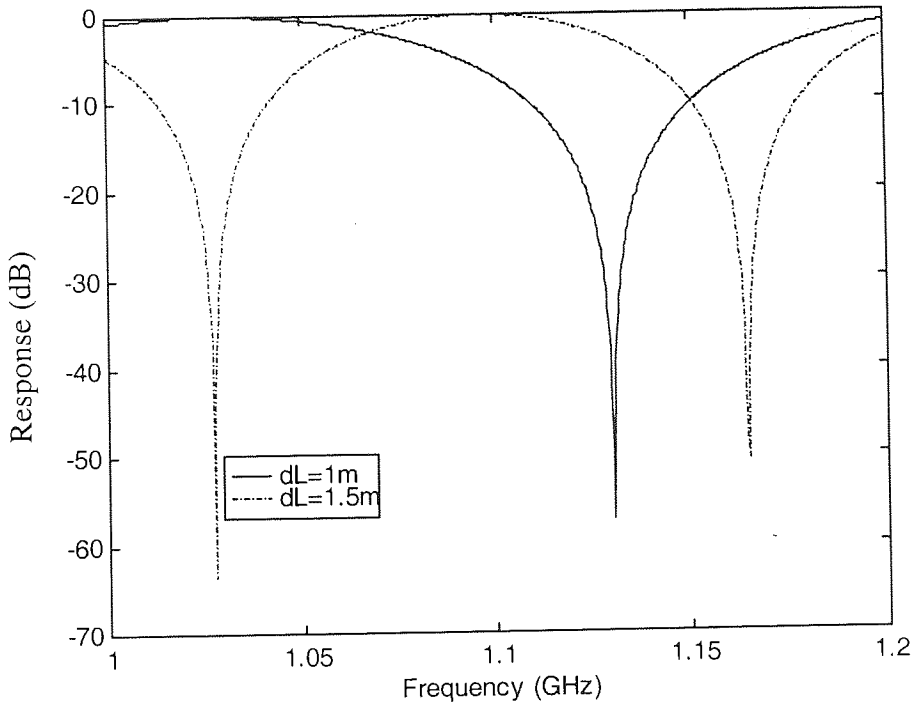

Figure 2- 27. Frequency response of unbalanced Mach-Zehnder filter with different imbalance length (Solid line: *ΔL=1m*, Broken line: *ΔL=1.5m).*

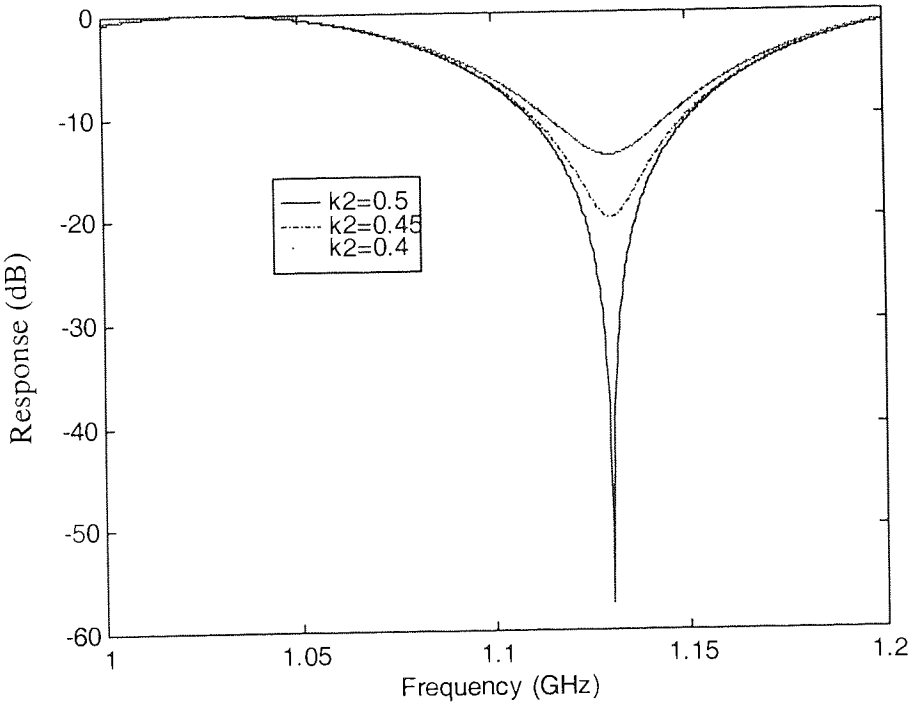

Figure 2- 28. Frequency response of unbalanced Mach-Zehnder filter with different splitting ratio (Solid line: *k_2=0.4*, Dash dotted line: *k_2=0.45m, Dotted line: k_2=0.4).*

We can see that the spectral location of band rejection is related to the imbalance length of this unbalanced Mach-Zehnder ΔL that means that filter tuneability can be achieved through the variation of ΔL.

Similar to recirculating filter, the filter's extinction is related to splitting ratio. In Figure 2- 28, we assume that one of the splitter keeps constant splitting ratio (k_1=0.5). Varying another splitter's splitting ratio we derive that this filter has a best extinction ratio when these two splitters are all 3dB splitters. With any deviation of the splitting ratio results a degradation of band rejection.

The nonrecirculating filter has the advantages of apodisation capacity, linear phase and better stability. More detailed study of nonrecirculated filter can be found in Chapter 4 where we use fibre Bragg grating array to build transversal filter.

2.7.4 FBG Implementation Of Recirculating And Nonrecirculating Filters

The recirculating and nonrecirculating fibre-optic delay-line filters described above are made of just fibres and couplers. FBG can be used to build these structures and provide more degrees of flexibility.

Zhang *et al* [97] reported a recirculating FBG based filter. Instead of using a coupler to split the light and feed it back, this device employed a weak grating (grating reflectivity varied according to the operating wavelength) to partially reflect the light. This simple structure provides the tuneability of notch depth. In addition, the FSR of the filter can be achieved by using cascaded uniform of different Bragg wavelength instead of a single chirped grating. The experimental diagram is shown in Figure 2-29.

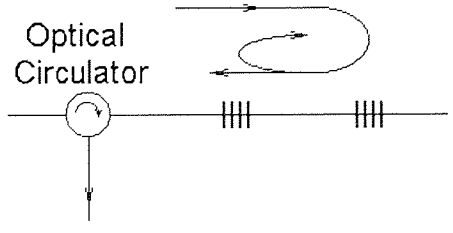

Figure 2-29. FBG based recirculating filter.

Nonrecirculating FBG based filter is also demonstrated [98]. The schematic diagram is shown in Figure 2-30.

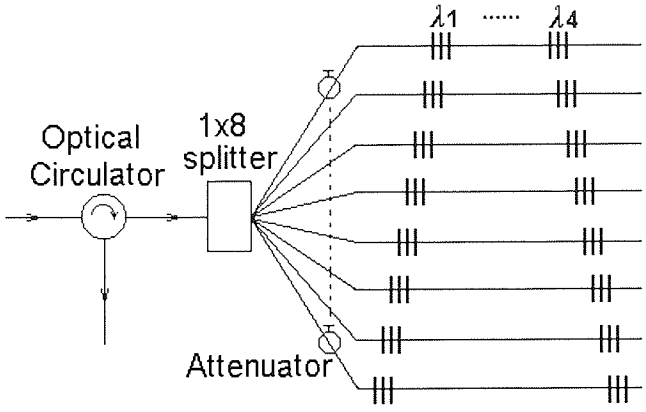

Figure 2-30. FBG based nonrecirculating filter.

The light is equally split into eight parts, incrementally delayed in each arm. The attenuators provide the tap weighting. Compared with all-fibre type filter, this FBG filter is more flexible on providing tap weighting, tuneability and reconfiguration [98].

Another scheme is to build these nonrecirculating filters using a chirped fibre Bragg grating and a laser array [99,100,101]. As in Figure 2- 31, the reconfiguration and apodisation is fulfilled through the adjustment of the laser intensities. The advantage is that short sampling time (good time-domain resolution) can be achieved. Since the delays are achieved through the optical carrier.

The drawbacks of this structure compared with our grating array scheme are:

- It uses a large optical bandwidth, which is a defect for WDM applications.
- Inflexible for tap apodisation. The apodisation can only be fulfilled through the adjustment of laser intensity. The response speed is limited by the tuning speed of tuneable laser.

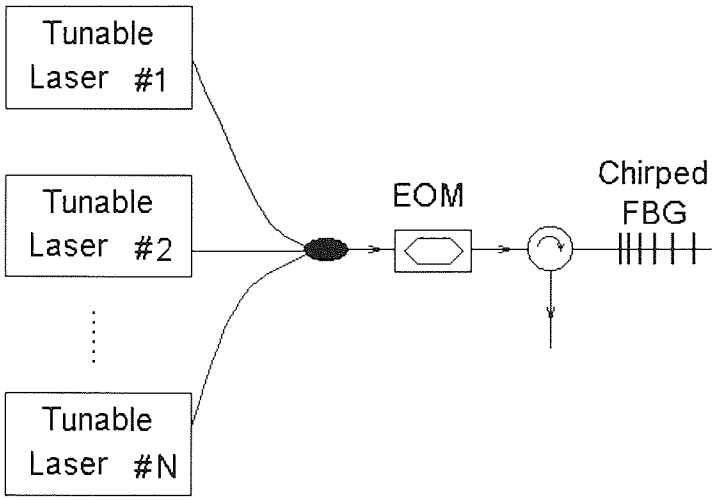

Figure 2- 31. Transversal filter with laser array and a chirped FBG.

2.8 Chapter summary

The aim of this chapter was to provide fundamental concepts of fibre Bragg gratings and some background introduction of delay-line filter. In the next two chapters, experimental details are given on the specific strain, magnetic-field sensing and microwave transversal filters using FBG. The introduction of other technologies here helps the understanding of the relation between our research with other applications, the advantages and trade-offs.

3 FIBRE BRAGG GRATING STRAIN AND MAGNETIC-FIELD SENSOR SYSTEMS

3.1 Chapter Overview

This chapter describes works on fibre Bragg grating strain and magnetic-field sensing. The works carried out to experimentally set up a static strain sensor with interferometric interrogation. Then a magnetic-field sensor was built with the facilitation of this strain sensor.

The magnetic-field sensor developed in this experiment has the characteristic of high sensitivity. In addition, it inherits the multiplexing potential from FBG sensor. The on-coming issues and disadvantages are also been presented in context.

3.2 Introduction

Fibre Bragg grating sensors have become a topic of very intense research interest since they were demonstrated for strain and temperature sensing in 1989 [102]. The main reason is that FBG sensors have several distinct advantages over other fibre optic sensors, including unique wavelength division multiplexing capacity [103] and absolute measurement [104]. Despite the advantages they can offer, the progress of commercialise FBG sensors has been slow due to the proven reliability records and manufacturing costs of the conventional electro-mechanical sensor [105]. However, FBG sensors seem to be an ideal candidate for realising 'Smart structures' where sensors are embedded in (or attached to) the structure for achieving a number of distributed sensing objectives [106]. Such applications include health monitoring [107], shape control and vibration sensing [108], hydrophone [109], high pressure [110], and acceleration measurement [111]. Generally, FBG sensor technology is near to maturity after 10 years of research and development. Efforts are now

turned to realise cost-effective FBG sensor systems and to explore more potential applications. Recently, research and development on FBG sensors have shown that they can be used for the measurement of a variety of parameters. A few FBG sensors are commercially available and they are installed in large-scale practical applications [112,113,114].

The several advantages of FBG sensors over traditional electrical strain gauges when used for distributed strain sensing include (1) compact size (typically 125 μm in diameter), which is ideal for embedding into composites without perturbation to the characteristics of the structure. (2) Easy multiplexing character, unlike strain gauges, which need a large amount of wiring. (3) Immunity to electro-magnetic interference and potential capability of surviving in harsh environments. (4) Good resistance to corrosion when used in open structures, such as bridges and dams. (5) Long lifetime (25 years or more with annealing). These features have made FBG sensors very attractive for quality control during construction and heath monitoring after building. The main disadvantage of FBG sensor is its 'cross-sensitivity', that is, sensitivity to both strain and temperature, which needs much attention to isolate these perturbations.

3.3 Strain Sensing System Set-up

3.3.1 Grating preparation

The gratings used in this experiment were fabricated by Dr. Lin Zhang. The reference grating has a Bragg wavelength of 1521nm, transmission of -10.6dB, bandwidth of 0.20nm. The sensing grating has a central wavelength of 1541nm with -21dB transmission and 0.33nm bandwidth. The laser used for the fabrication of gratings is a CW argon-ion laser. The output wavelength is 244nm with an intracavity-frequency-doubling crystal. The beam is focused onto the fibre by a cylindrical lens. The lens is mounted onto a motorised translation stage and fully controlled by Group developed LabVIEW software[1]. The grating's transmission (or reflection) profile was obtained through an optical

[1] Software developed by Dr. John Williams.

spectrum analyser (OSA). The fibre used was a hydrogen loaded, boron-germania co-doped fibre to achieve high reflectivity. These uniform gratings were fabricated using holographic method, which has a length of 5mm. Figure 3-1 and Figure 3-2 is the measured sensing grating and reference grating reflection spectrum. They were measured just before the signal was injected into photodetector. Note that there are some oscillations on each side of the main grating reflection. These are caused by the unbalanced Mach-zehnder interferometer interference, which has a raised cosine transfer function. Later, these oscillation fringes were used to control the optical path difference of Mach-Zehnder interferometer.

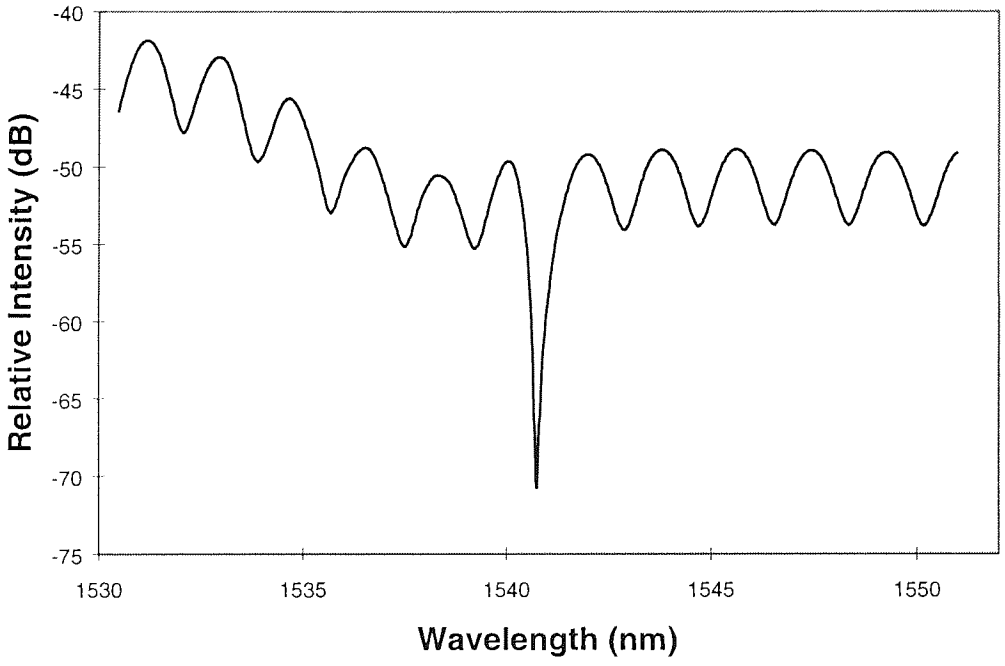

Figure 3-1. Sensing grating spectrum.

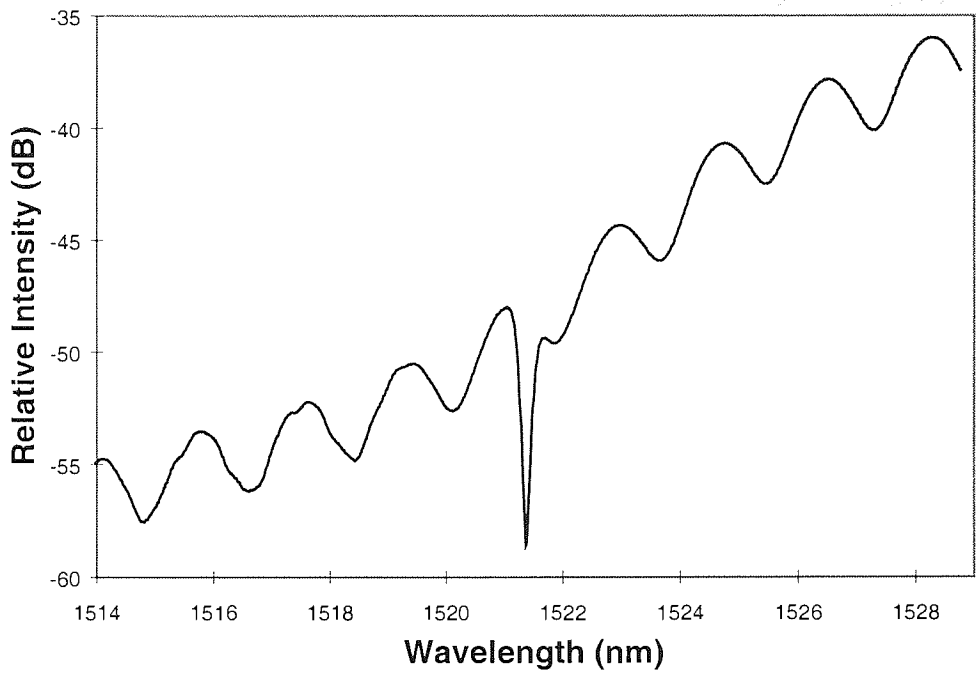

Figure 3-2. Reference grating spectrum.

3.3.2 Fabrication of fibre optic Mach-Zehnder

The Mach-Zehnder used in this experiment was a self-made fibre optic type interferometer. It consisted of two 3dB couplers, a fibre stretcher, a piezoelectric transducer (PZT) cylinder and two fibres of three metres long. The stretcher consisted of two moveable posts, adjusted by a tuning handle. Two fibre ends were clamped onto these two posts. The other fibre was attached on the PZT using Loctite instant adhesive. Since fibre coating couldn't resist the corrosion of this adhesive, the fibre was stripped at the place of adhesion. A length of 15cm was left at each end for splicing. Each end was splice onto one coupler separately. So did the fibre stretcher. The PZT, the fibre stretcher together with the fibres was packed into a box to minimise the environmental affection. The Optical Path Difference (OPD) can be adjusted by stretching one of the arms using the fibre stretcher. The arm having stretcher on is 1.65 mm (optical path) shorter than the other arm. By tuning the stretcher, this arm can be equal length of the other and even 2.65 mm (optical path) longer. Note that certain OPD should be fixed before packaging.

3.3.3 Coherent Length Of FBG Vs. OPD Of Mach-Zehnder Interferometer

For a Mach-Zehnder structure, the phase difference $\Delta\varphi$ of two interferometer arms is

$$\Delta\varphi = \frac{2\pi}{\lambda} OPD$$

Equation 3- 1

where OPD is the optical path difference of the unbalanced interferometer. In order to get the phase change due to the wavelength difference $\Delta\lambda$, we differentiate Equation 3- 1:

$$\Delta\varphi' = -\frac{2\pi}{\lambda^2} \cdot OPD \cdot \Delta\lambda$$

Equation 3- 2

We can know from Equation 2- 34 that the interferometer output are sinusoidal modulated. So the 3dB bandwidth of a fringe represents that the phase change $\Delta\varphi'$ in Equation 3- 2 is equal to π.

$$\therefore \Delta\lambda = \frac{\lambda^2}{2 \cdot OPD}$$

Equation 3- 3

Equation 3- 3 is useful in calculating the OPD. The central wavelength λ of a fringe can be measured using an OSA. The 3-dB bandwidth can be derived by using two cursors marking the points 3 dB down from the central point. In this experiment, several period of this oscillation were used in order to obtain averaged value of $\Delta\lambda$. The interference condition for this system is that the OPD of the interferometer must be smaller than the coherence length calculated later from Equation 3- 3.

3.3.4 Thermal Drift Compensation

Although very sensitive to dynamic strains, the resolution of interferometric technique will be degraded for quasi-static strain measurement due to thermal drifts induced optical phase perturbation. This can lead to inaccurate readings. In this experiment, a technique to compensate for this drift using a PI

(Proportional, Integral) control technique and a reference grating had been adopted.

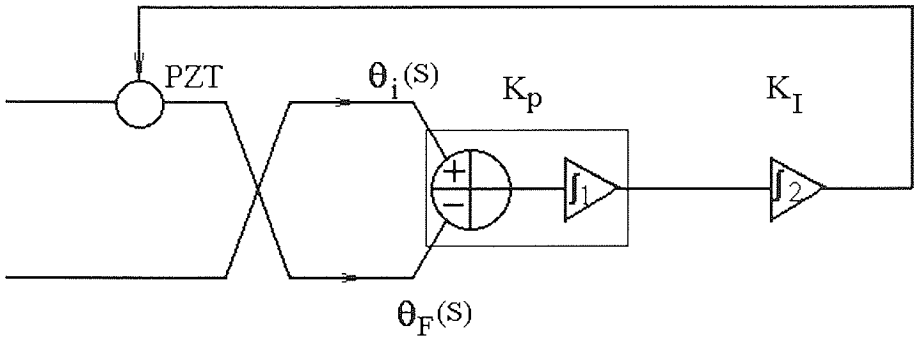

Figure 3-3. Schematic diagram of PI control.

The feedback system use PI feedback control technique is shown in Figure 3-3. Proportional control multiplies the error signal (the difference between actual and desired phase) by a user-specified gain factor K_p and used it as a corrective signal. Integral control accumulates the error signal over time, multiplies the sum by a gain factor K_I and uses the result as a corrective signal. Since this technique also acts upon past errors, the correction factor does not go to zero allowing steady-state errors to be eliminated.

For a second order system the natural frequency ω_n is directly proportional to system bandwidth BW and inversely proportional to rise time t_r. So increase K_p and K_I will increase ω_n, thus increase to system bandwidth BW and rise time t_r. However if K_p and K_I are too large, damping ratio ξ will approach zero and we say the system is undamped. This will cause system oscillation. So every component gain must be carefully set.

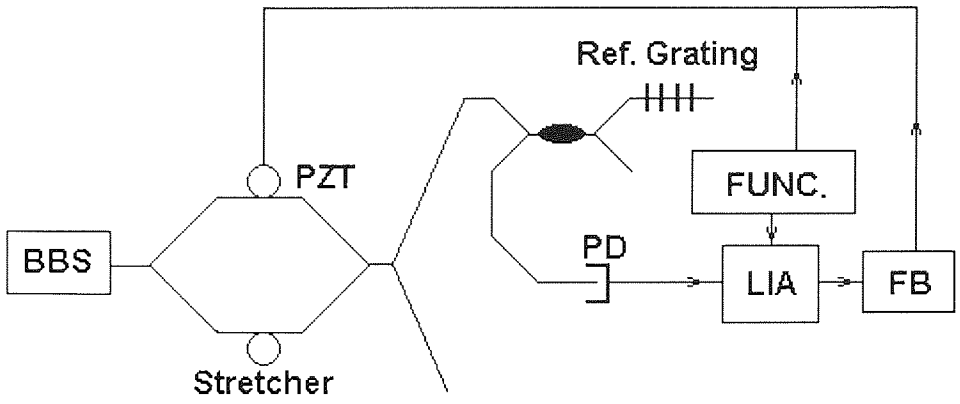

Figure 3-4. Schematic diagram of drift compensation using a reference grating. BBS: Broad Band Source. PZT: Piezoelectric Transducer. PD: Photo Detector. FUNC: Function Generator. FB: Feedback. LIA: Lock-in Amplifier.

In order to null the environmental perturbation, a reference grating was also used. In Figure 3-4, the light from the reference grating was changed into electronic signal with the same electronic frequency as the ramp modulation. The ramp signal is sent into the feedback through the modulation key. The phases of the two signals are compared and the error signal is multiplied by a gain factor K_1 in a proportional integrator. The output from the proportional integrator is further accumulated by a second integrator, which has a gain factor K_2. Then a signal to correct the phase perturbation is feedback to the PZT. The PZT enlarges or contracts to compensate for the phase perturbation.

3.4 System Set-up

The schematic diagram for strain sensing is shown in Figure 3-5. The optical source used was an erbium-doped fibre (EDF) superfluorescent broadband source. Its output was approximately 0.5mW within a 62nm FWHM bandwidth (1514-1576nm). The reflected power from the reference and sensing gratings is 1.03μW and 347nW respectively. The reflected power difference between the two gratings is due to not only their own reflectivity variations but also the power level differences of the broadband source at their respective wavelengths. A source with a smaller, flatter bandwidth and higher power would clearly have improved the system. The fibre source is injected into an unbalanced fibre Mach-Zehnder interferometer.

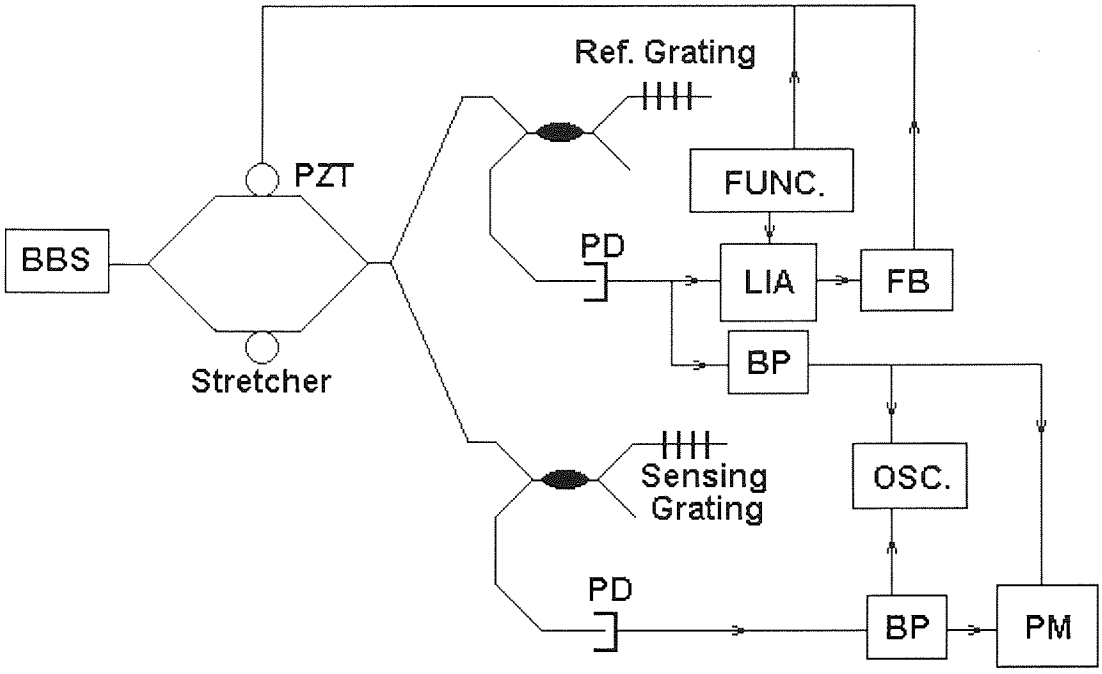

Figure 3-5. Drift compensated Bragg-grating sensor system with sensing and reference grating elements and interferometric wavelength-shift detection. BBS: Broad Band Source. PZT: Piezoelectric Transducer. PD: Photo Detector. FUNC: Function Generator. FB: Feedback. LIA: Lock-in Amplifier. BP: Band-pass Filter. OSC: Oscilloscope. PM: Phase Meter.

Each grating reflects a narrow-band portion of the interferometer output signal. The OPD and the coherence length of the optical component reflected by the gratings (determined by the bandwidth of the grating) must be calculated in advance so that the OPD is within the coherence length.

The upper Lock-in amplifier was to amplify and low pass filter the reference signal. In addition, in this experiment, the modulation signal was applied to Mach-Zehnder interferometer through the feedback device.

As shown in Figure 3-5, the light from the BBS was filtered by the unbalanced Mach-Zehnder interferometer. The signal reflected from the reference grating was locked, amplified and sent into feedback device system. The feedback output was sent to a PZT, driving it to eliminate the thermal drift of the interferometer, keeping the system at quadrature point to give the best sensitivity. The strain was applied through a clamp. The value of the strain

applied was calculated using a micro-strain (με) unit. One micro-strain equals to a micrometer elongation over one meter length.

According to Equation 3- 6, the phase change is directly proportional to Mach-Zehnder OPD. That means we can change the system's sensitivity through the Mach-Zehnder's OPD adjustment. In order to demonstrate this feature, we set the Mach-Zehnder's OPD as 2.65, 1.7, 1.23 and 0.2mm.

Four groups of strain-to-phase shift results were obtained for these four different imbalance lengths.

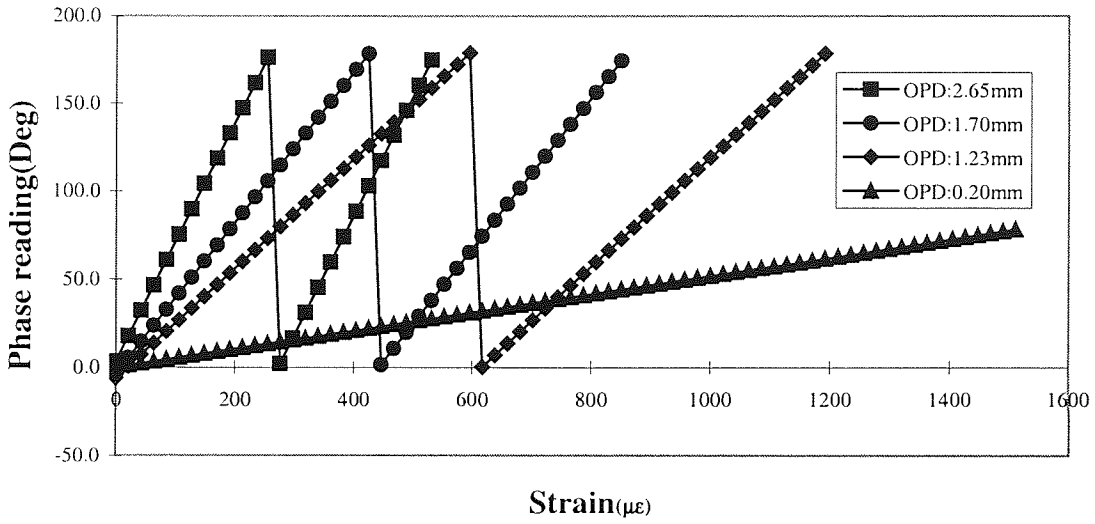

Figure 3-6. Strain-to-phase shift conversion responsivity of different imbalance length.

As we can see in Figure 3-6, the phase shifts show a good linearity with strain applied on the sensing grating and the strain-to-phase shifts responsivity are proportional to the imbalance length of the interferometer. In the cases of long OPD (2.65 and 1.7mm), the phase reading reached the full scale of phase meter rapidly. As seen in Figure 3-6, the phase reading suddenly return to its origin when it has reached the full scale. There is a trade-off between the sensitivity and measure range. In applications that need better sensitivity, a larger OPD should be given at the price of smaller measure range. The extra attention associated with this condition is that continuous monitoring will be needed. In applications when sensitivity is not very demanding, a smaller OPD should be assigned to ensure larger measure range.

To obtain the resolution of the system, we applied gradually the strain to the sensor when the Mach-Zehnder was in different OPD. The resolutions of different imbalance length are listed in Table 3-1.

Table 3-1. Evaluation of the system for different imbalance

Imbalance length (mm)	0.2	1.23	1.7	2.65
Resolution (με)	3.59	1.33	0.98	0.98
Measure Range (με)	7132	1160	839	538

As can be seen, the resolution and dynamic range are all affected by the imbalance length. As the imbalance length becomes larger the resolution increases and the dynamic range decreases. However, we can see that the system resolution can not be improved when it reaches 1με. This is because the resolution is finally limited by the capacity of the feedback device to compensate for the thermal drift. Further increase of the imbalance length only improves the sensitivity of the system but not the system resolution. In addition, it should be noticed that a larger imbalance length of unbalanced interferometer needs a sensing or reference grating of narrower bandwidth. This can be seen from the following:

$$L_c = \frac{C}{\delta f}$$

Equation 3- 4

where L_c is the coherence length of a source, C is the light speed, δf is the 3dB bandwidth of a source. For a light source with central wavelength λ and central frequency f we have

$$f = C / \lambda$$

$$\therefore \delta f = -\frac{C}{\lambda^2}\delta\lambda$$

Equation 3- 5

$$\therefore L_c = -\frac{\lambda^2}{\delta\lambda}$$

Equation 3- 6

In order that the interference occurs, this source coherence length (In this experiment, the sensing and reference grating acted as a narrow-band source. They reflected a partial spectrum of the broad-band-source) must be larger

than the interferometer imbalance length OPD calculated from Equation 3- 3. According to this principle, consideration must be paid to the sensor design if this unbalanced interferometric interrogation technique is used. For sensors requiring good sensitivity, we need a larger OPD. Thus, a narrow-bandwidth grating is essential. Normally, the reflected light from this kind of grating is weak due to the smaller slice they have picked from broadband source. So this kind of sensor is not suitable for the sensing condition where the signal has to be transmitted for a long distance because the implantation of amplifiers in sensor system doesn't have economical advantage. On the other hand, a broadband grating with stronger reflection can be placed in a far distance. However, this system won't have as good sensitivity as systems employing narrow-band gratings.

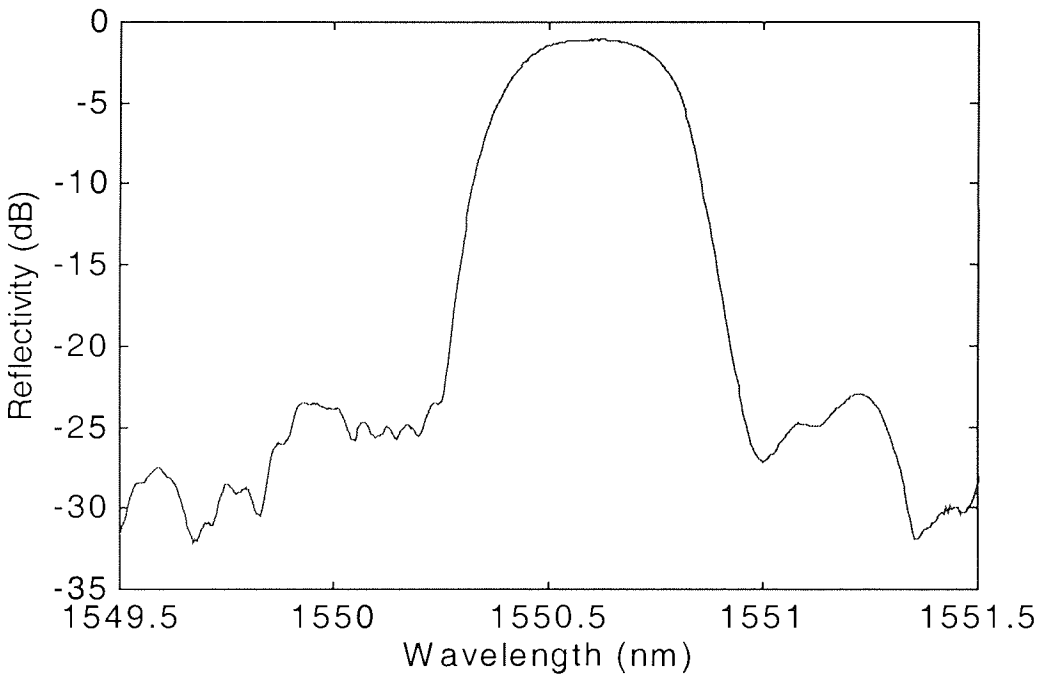

Figure 3- 7. Apodised grating used for sensing.

In order to compare the sensor performance of different type of gratings, another experiment was carried out. Three types of gratings were used in this experiment. The first was the original linear 0.35nm grating. The second was a chirped 6nm grating (1548-1554) with central Bragg wavelength of 1551nm, as shown in Figure 3-8 and a chirped 12nm grating (1538-1550) with central Bragg wavelength 1544nm, as shown in Figure 3-9. The third was an apodised grating as in Figure 3- 7. The grating was apodised using a raised cosine function. We

know from previous knowledge that apodised grating will provide better sidelobe-suppression. The aim of using apodised grating was to exam whether a better resolution would be obtained. The results can be seen in Figure 3- 10 and Figure 3- 11. In Figure 3- 10, we plot the strain-to-phase shift conversion responsivity of uniformed and apodised grating. It was noticed that they have similar responsivity due to the same Mach-Zehnder imbalance length they used. The slight difference was derived from the two grating's central wavelength difference. Both of the system had a resolution of 1με. Although the apodised grating offered better signal to noise ratio due to the efficient sidelobe suppression, it was believed from this result that the system resolution was eventually limited by the thermal drift.

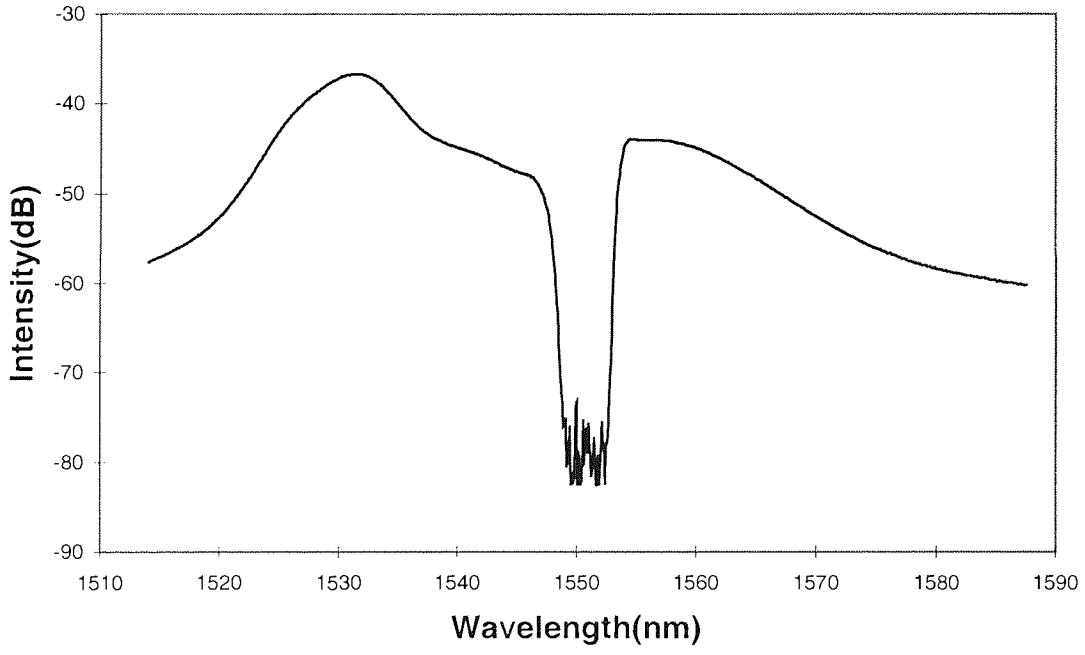

Figure 3-8. Spectrum of 6nm chirped sensing grating.

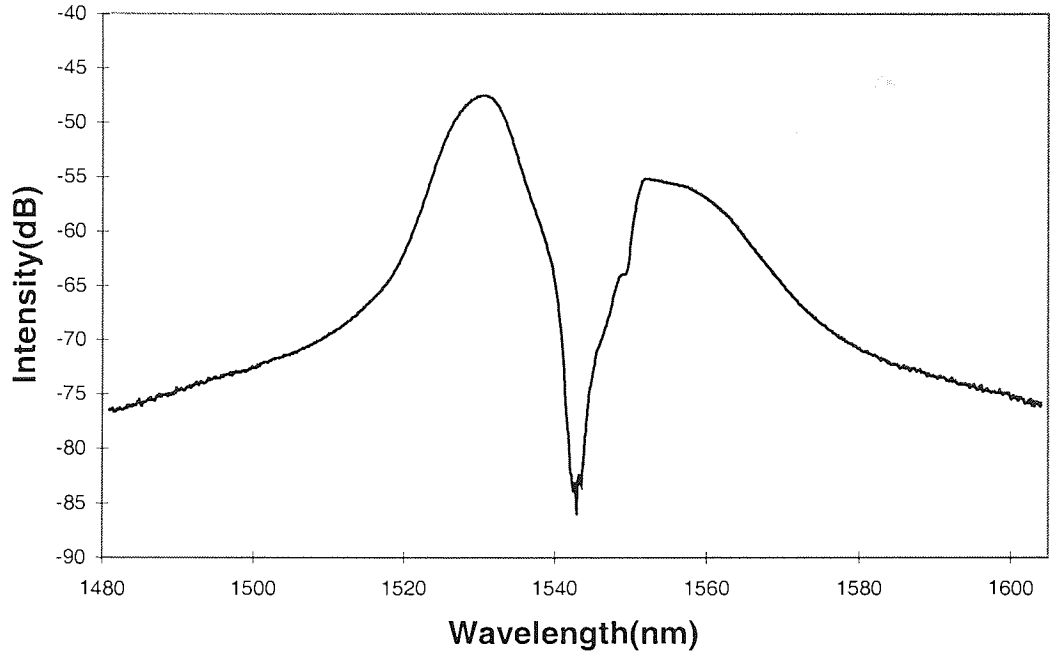

Figure 3-9. Spectrum of 12nm chirped sensing grating.

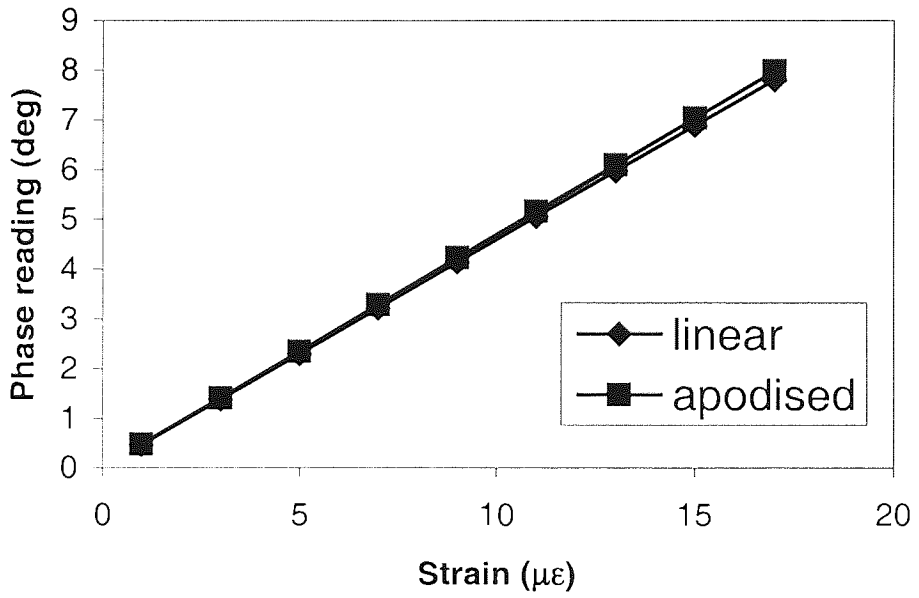

Figure 3- 10. Strain-to-phase shift conversion responsivity of uniform and apodised grating.

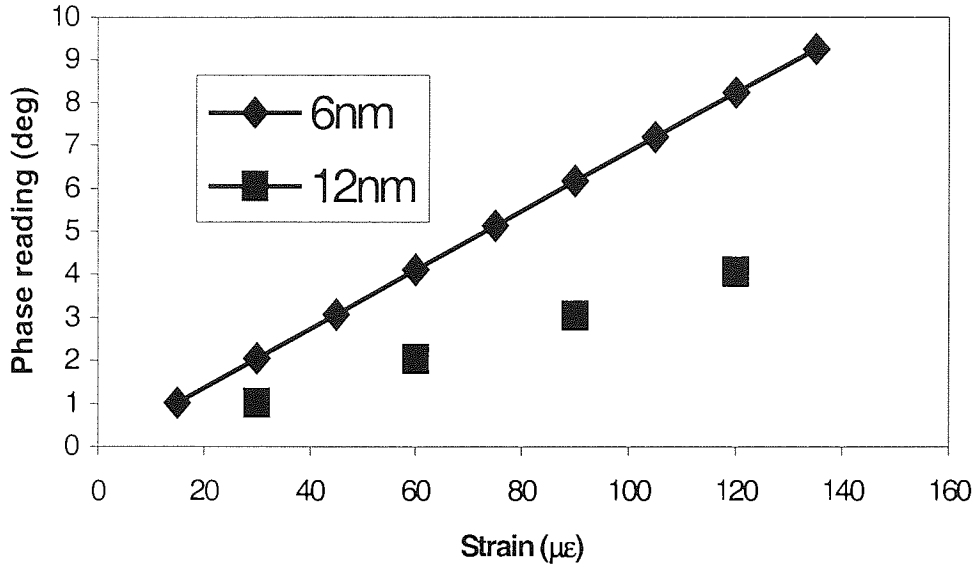

Figure 3- 11. Strain-to-phase shift conversion responsivity of chirped grating.

The calculated maximum OPD of unbalanced Mach-Zehnder interferometer for 6nm and 12nm bandwidth gratings were 0.4mm and 0.2mm respectively. It was noticed from the experiment result, as shown in Figure 3- 11, that the 6nm grating sensing system had a resolution of about 15με and 30με for 12nm system. After examination, it was finally decided that this resolution was limited by the phase meter resolution, which was 0.1 degree. Since a large OPD used in these two systems, a low strain-to-phase shift conversion resulted so that the bottleneck turned out to be the phase meter in this experiment. The advantage of using a chirped sensing grating is that it can reflect much stronger intensity than linear grating. However, the trade off is that we have to set the interferometer at a small imbalance so that the bandwidth of the grating is within the coherent length, in which case the system has smaller sensitivity.

Table 3-2. Evaluation of the system for different sensing grating

Grating	uniformed	Apodised	chirped 6nm	chirped 12nm
Resolution (με)	1	1	15	30
Measure range (με)	390	390	2600	5300

We can chose the type of grating according to Table 3-2 when we build strain sensors. The uniform and apodised gratings have similar resolution. However,

priority should be given to uniformed gratings because of the relative simplicity of fabrication. Chirped gratings are suitable for long distance transmission but at the price of low resolution and sensitivity. The choice should be made at design stage according to special specification.

3.5 Magnetic Field Sensing

In the following sections, we will demonstrate that FBG can be used as a magnetic-field sensor. This sensor was built from the strain sensor we have set up in the previous experiment.

There are several kinds of sensors which works at different sensing region [115], such as low field less than 10^{-6} Gauss, medium field from 10^{-6} Gauss to 10 Gauss and high field above 10 Gauss. Each sensor has its uniqueness and limitation. For fibre-optic magnetic-field sensors, their advantages over electrical magnetic sensor like flux gate sensors are the multiplexing ability low loss signal transmission, large bandwidth and electromagnetic interference immunity. It is necessary to improve the performance of fibre-optic magnetic-field sensors and make it compatible with standard readout device to push them forward towards practical use.

3.5.1 Magnetic Field Sensing using fibre-optic sensor

In measuring magnetic fields there are two basic approaches for the use of single-mode silica and doped silica optical fibre sensors, namely, the Faraday rotation approach and the magnetostrictive jacket or stretcher approach. In the former approach, an external magnetic field H is applied longitudinally to a fibre to produce a rotation in the direction of linear polarisation. Smith [63] reported an electric current measuring in a range of 0-1000A. However, this approach can measure only large currents and magnetic fields. The alternate approach uses a magnetostrictive transducer [116]. It is capable of providing much greater sensitivity in magnetic field measurement and suitable for the grating based optical fibre sensor. We use a metallic glass as the transducer bonded to the fibre Bragg grating. Applied magnetic fields change the length of this material straining the Bragg grating in the longitudinal direction and shifting its

central reflected wavelength. This shift in wavelength may then be detected using interrogation techniques stated before.

There are some reports on electric current or magnetic field sensing using fibre-optic sensors [63,117,118,119]. Like other fibre-optic sensors, FBGs are ideal for use in the electrical power industry due to their immunity to electro-magnetic interference. In addition, FBGs can be written onto standard 1.55 μm wavelength telecommunication fibre, so that long-distance sensing is applicable due to the low transmission loss of the fibre at this wavelength. Loading of power transmission lines [120], winding temperature of electrical power transformers [121] and electrical currents [122] have been measured with the FBG sensors.

Optical fibre sensors exploiting the Faraday effect have been used for measurement of large currents at high voltages in the power distribution industry as early as in late 70's [63]. However, the Verdet constant of most doped silica fibres is very small ($\approx 1.5\times10^{-2}$ min · A^{-1}) that only large currents and magnetic fields can be detected [123]. An alternative method is to measure the large current indirectly by using a hybrid system consisting of a conventional current transformer and a piezoelectric element [124]. The current transformer converts the current change into a voltage vibration and then this voltage change is detected by measuring the deformation of the PZ using an FBG sensor. Interferometric wavelength-shift detection method has been exploited for the detection of wavelength-shift induced by the current and a current resolution of 0.7 A/√Hz over a range of up to 700 A has been obtained with a good linearity. More recently, the resolution has been further improved by replacement of the FBG with an FBG-based Fabry-Perot interferometer (FPI) formed by arranging two FBGs with the same central wavelengths along a length of fibre [125].

In the next few sections, we will concentrate on the magnetostrictive transducer type sensor. Prior to introducing the sensing system, the magnetostrictive transduction effect will be described.

3.5.2 Magnetostriction Effect

Magnetostriction is the relative elastic change in length produced by the influence of a magnetic field. According to the so-called "coherent rotation model," [126] which is valid only when the applied magnetic field is perpendicular to the anisotropy field H_A of the magnetostrictive transducer, the magnetostriction can be written as [126]:

$$\delta\varepsilon = CH^2$$

Equation 3- 7

where $C=3\Lambda_s/2H_A^2$. Λ_s is the saturation magnetostriction coefficient.

In measuring the DC induced magnetostriction, two effects must be considered. They are demagnetisation and mechanical loading. Both reduce the transfer of strain to the FBG sensor.

3.5.3 Demagnetisation

The magnetic field inside a highly permeable material is not equal to the externally applied field. This is because of the demagnetisation effect. According to the so-called 'coherent rotation model' the material possesses uniaxial magnetic anisotropy. It defines an easy axis characterised by an anisotropy field H_A. In the absence of an externally applied magnetic field, the magnetic moments point either in the positive or in the negative sense along the direction of the anisotropy field-the 'easy axis'. The strength of the anisotropy field H_A determines how 'tightly' the moments are held along the easy axis as in Figure 3-12. The demagnetisation is defined from the response of the magnetic field such that if the material has positive magnetic susceptibility, the moments respond in a manner that partially cancels the externally applied field. Considering only one direction, the internal and external fields are related by

$$H_{int} = \frac{H_{ext}}{1 + N\chi}$$

Equation 3- 8

where N is the demagnetisation factor, which depends only on the geometry of the sample, and χ is the volume magnetic susceptibility. To a rough approximation assuming DC fields and neglecting edge effects [127], we have:

$$N = \frac{8 A_m}{L_m^2}$$

Equation 3- 9

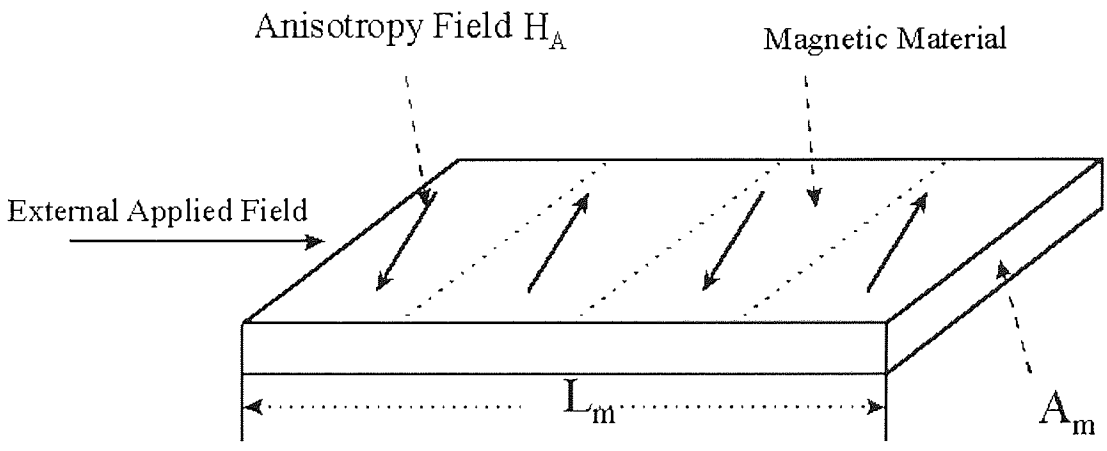

Figure 3-12. Anisotropy field of magnetic material.

3.5.4 Mechanical Loading

The bonding of fibre on the transducer introduces some degree of deleterious mechanical loading. The amount of loading can be estimated by considering the magnetostriction in terms of equivalent forces F_m acting on the transducer. That is,

$$\delta\varepsilon = \frac{F_m}{A_m E_m}$$

Equation 3- 10

where A_m is the area of the transducer and E_m the Young's modulus which is 1.7×10^{11} $N\cdot m^{-2}$ [127]. When a nonmagnetostrictive material such as the fibres bonded to the transducer, the force due to magnetostriction remains the same,

but the same area on which the force must act is larger by an amount equal to the area of the fibre A_f weighted by its Young's modulus E_f. Assuming that the fibre is perfectly bonded (η=1) to the material, the relation between the unloaded strain and the loaded strain is

$$\delta\varepsilon_{loaded} = \frac{\delta\varepsilon_{free}}{1 + A_f E_f / A_m E_m}$$

Equation 3- 11

Therefore, we can rewrite Equation 3- 7 to become:

$$\delta\varepsilon = \frac{3\lambda_{sat}}{2H_A^2} \frac{1}{\left(1 + A_f E_f / A_m E_m\right)\left(1 + N\chi\right)^2} H_{ext}^2$$

Equation 3- 12

Because the strain sensor is used to detect the magnetostriction the strain-to-phase shift relation (Equation 2- 37) is still applied here. Substitute the strain $\delta\varepsilon$ with Equation 3- 7 we get:

$$\delta\varphi_s = -\frac{2\pi n d}{\lambda_B} \xi \cdot c \cdot H^2$$

Equation 3- 13

where c is the coefficient part of H^2 in Equation 3- 12.

3.5.5 Sensor Configurations

It is easy to understand that the sensor transducer will affect the system's performance such as resolution and frequency response. There are three reported types of transducers for FBG based magnetic-field sensors [123]. 1) The bulk magnetostrictive cylinder or mandrel with fibre bounded to its circumference. 2) A metal coating or jacket applied uniformly to the surface of the fibre (or fibre grating). 3) The fibre (or fibre grating) bonded to a metallic strip, as illustrated in Figure 3-13. It was also stated in this report that the sensor response depends on the material and mechanical structure of transducer and the stripline metallic glass offer both high static sensitivity and good frequency response. So we decided to use some longitudinally annealed foil of metallic glass 2605CO provided by AlliedSignal Inc. As in Figure 3-13,

the foil is 5cm long, 1.25cm wide and 25 μm thick. The sensing grating is attached to the magnetostrictive material with a 1.2mm film of Loctite instant adhesive.

In this experimental configuration, a strain sensor formerly built was used. Since we are aiming to build a magnetic-field sensor with high sensitivity, the OPD of the unbalanced Mach-Zehnder interferometer was set to 2.65mm, which was the maximum value. The sensing grating used was the uniformed grating with central wavelength of 1541nm and a bandwidth of 0.35nm. The system could detect a minimum static strain of about 1με. The sensing grating together with the magnetic-field generating coil is shielded to avoid ambient magnetic interference and thermal drift.

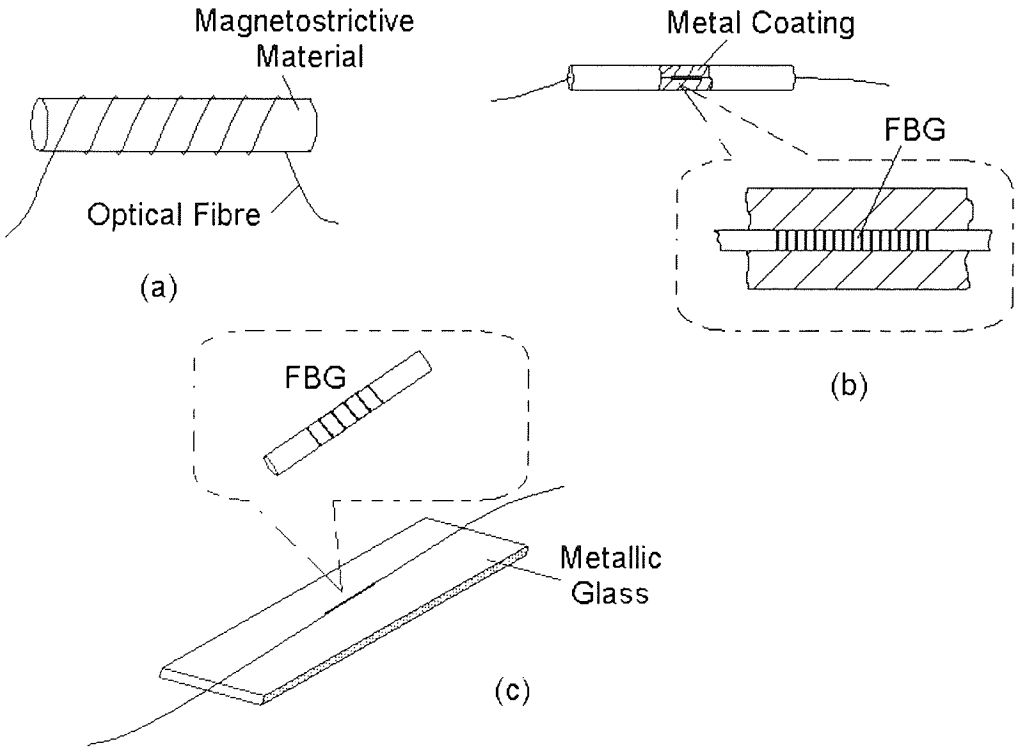

Figure 3-13. Fibre-optic magnetic-field sensor structure.

We estimate the demagnetisation and mechanical loading effects of the transducer to give us an idea of how much strain can be passed to sensing grating. Rewriting Equation 3- 8 for the demagnetisation effect and giving in the value of every term for a typical 2605CO transducer [126].

$$H_{int} = \frac{H_{ext}}{1 + N\chi}$$

N: Demagnetisation factor (≈0.001).

χ: Volume magnetic susceptibility (=2×10^{4} SI units).

For mechanical loading effects

$$e_{loaded} = \frac{e_{free}}{1 + A_f E_f / A_m E_m}$$

Equation 3- 14

A_f is the area of the fibre attached to the transducer weighted by its Young's modulus E_f.

In this circumstance, $e_{loaded}=0.99e_{free}$.

Substitute these into Equation 3- 12 and λ_{sat}=35ppm, H_A=1 Gauss [63,128] for 2605CO. We get

$$\delta\varepsilon = 1.15 \cdot H^2$$

Equation 3- 15

A coil is used to provide a known test magnetic fields and the magnetostriction calculated using Equation 3- 12, where the phase shift is read from the phase meter of a lock-in amplifier. The results are shown below in Figure 3-14.

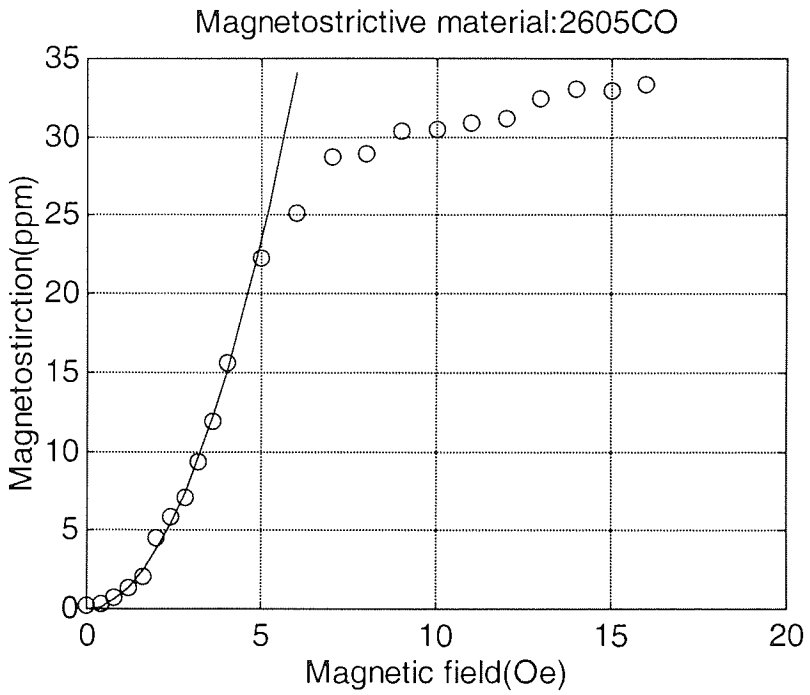

Figure 3-14. Static magnetic-field measurement response. (o experimental data, - a quadratic fit for small values).

The circles are the experimental results for a static magnetic-field measurement. For small fields, it has a quadratic form, which begins to saturate above 3 Gauss. The solid line shows a quadratic fit for small field values. It gives a quadratic coefficient of C=0.97. This is slightly smaller than the value of 1.15 calculated from the anisotropy field of the material. The difference is due to some inefficiency in the transfer of the strain from the magnetostrictive material to the Bragg grating via the bonding material.

The noise component on the measured phase is determined and from this, we find that the sensor minimum detectable field is 0.027 Gauss. This result is not as good as that reported in [123], which is 5×10^{-9} G/m. But this result was achieved using a 1m optical fibre sensor. As we have studied before, the advantages associated with this FBG magnetic-field sensor were the multiplexing potential and absolute measurement. The compact size of FBG sensor can find them great convenience when multi-points sensing are necessary, such as the detection of speed, position or rotation of a magnetic object.

3.5.6 Dynamic Magnetic-Field Sensing

The dynamic response of this readout technique is limited by the maximum frequency at which the interferometer can be ramped (typically 100Hz here). Therefore, for dynamic magnetic field sensing, a different strain sensing scheme is employed, as shown in Figure 3-15.

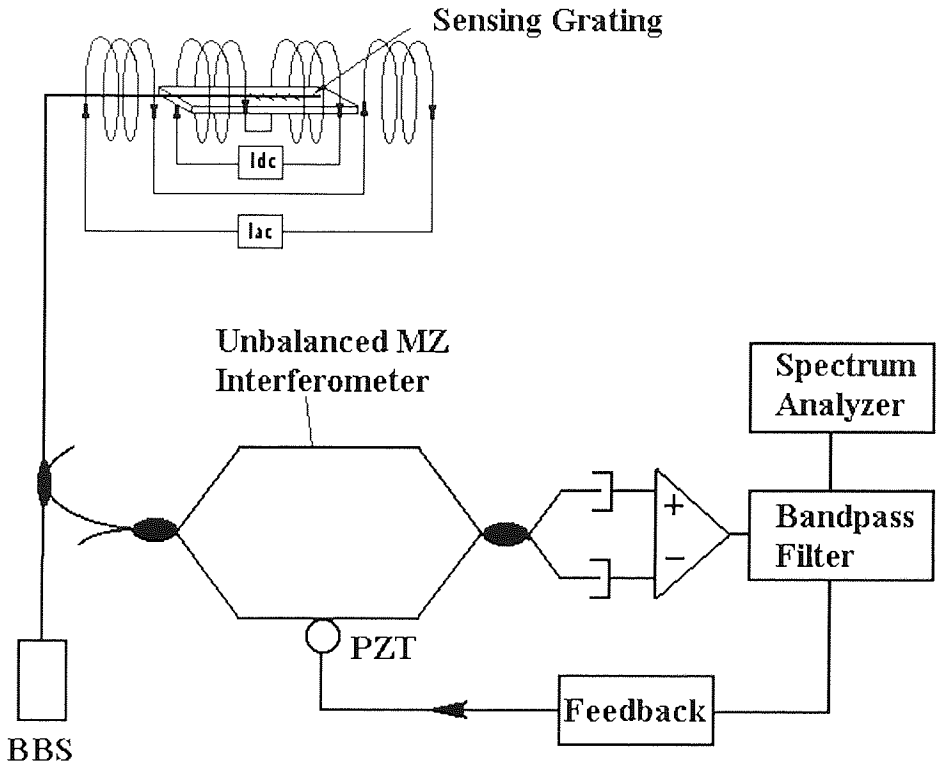

Figure 3-15. Diagram of measuring dynamic magnetic field using magnetostrictive material.

The same broadband source and interferometer were used for the dynamic field measurements. A dynamic field at a frequency of 3kHz was generated using the Helmholtz coil and a bias field was added to this. The bias field of 0.3 Gauss was chosen in this experiment because we could get best sensitivity. With this bias field, we then changed the applied frequency of the dynamic field to measure the frequency response and found a resonance peak at 3kHz.

Finally, we set the DC bias at 0.3 Gauss where the sensor has best sensitivity and the dynamic signal to a frequency of 3kHz. We gradually changed the amplitude of the dynamic signal, measuring the amplitude reading on spectrum analyser. The result, shown in Figure 3-16, is linear to within 99.23% linearity

and signal-to-noise measurements indicates a minimum detectable field of 4.7×10^{-4} Gauss.

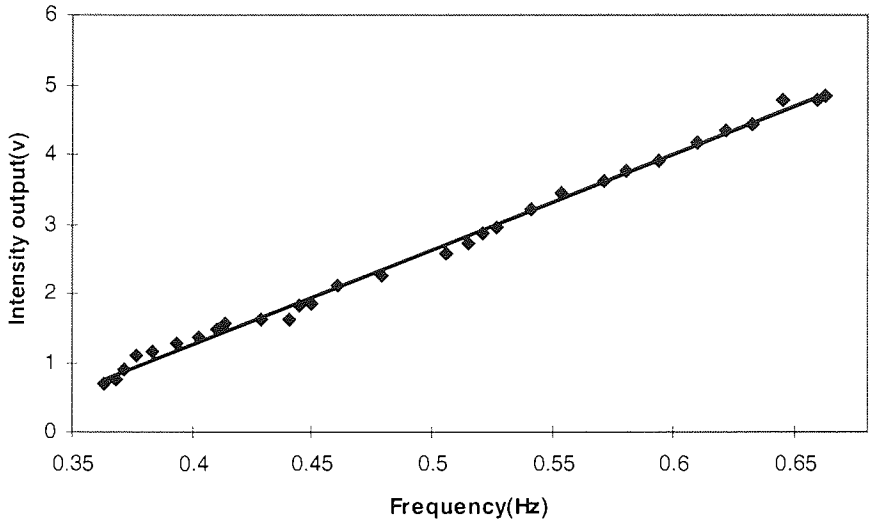

Figure 3-16. Dynamic magnetic-field measurement response.

Certainly, there are some issues to be addressed. First, for static magnetic-field sensing, the resolution is limited by the strain-sensing resolution. Further work need to carried out on the proper isolation of the Mach-Zehnder interferometer from thermal perturbation. Second, this sensor was a one-dimension device. That means only one direction of magnetic field could be detected at one time. It is reasonable that this sensor should be developed to be able to perform multi-axial sensing applications.

3.6 Chapter Summary

The work described in this chapter is on the fabrication of high-resolution strain and magnetic-field sensor. This kind of sensor has the advantage of low signal transmission loss and multiplexing capacity. The magnetic-field sensor was fabricated by attaching a magnetostrictive transducer onto a FBG strain sensor. The transducer translated the strength of magnetic field into the degree of its mechanical extension. As we can imagine, the resolution of this magnetic-field sensor can be limited by factors such as resolution of FBG strain sensor, effectiveness of transducer bonding and transducer characteristic. In this circumstance, a high-resolution magnetic-field sensor consists necessarily of a

high-resolution FBG strain sensor and a sensitive magnetostrictive transducer to be effectively bonded.

The first effort was to build a high-resolution static strain sensor. Interferometric interrogation scheme was employed because of its demonstrated high-resolution for dynamic strain sensing. Although a feedback electronic device was used and several gratings were tested to pursue a better resolution, we derived the conclusion that it is still the environmental thermal perturbation that limits the FBG static strain sensing resolution. A better shielded Mach-Zehnder interferometer should be made for this kind of device.

A successful candidate for magnetostrictive transducer should possess the characteristic of large magnetostriction and good frequency response. A metallic glass 2605CO was selected refer to its superiority over other forms of transducer. After careful bonding, this magnetic-field sensor achieved static resolution of 0.027 Gauss and dynamic resolution of 4.7×10^{-4} Gauss.

In order that this FBG sensor to be commercialised, they have to find themselves useful in several applications. Some of the applications, as we mentioned before are the electromagnetic pollution monitoring, high-voltage risk warning. We also noticed that this sensor has the resolution for Earth's magnetic field detection. This characteristic has enabled them varied applications such as vehicle speed and distribution sensing. Established sensors are magnetoresistive sensors. The distinct advantage of our FBG sensors are their multiplexing ability since a large number of sensor will be needed for this kind of sensing. Each of these magnetoresistive sensors needs at least two pairs of electrical wires. One pair for bridge amplifier, another pair for output signals. So a large amount of wiring work will be needed for large number of sensors. While this FBG sensor can have tens of sensors onto a single fibre and distributed even at a long distance due to the low loss characteristic of optical fibre. Further research need to carry out on the detection of magnetic field's direction in addition to magnetic field strength. In addition, the interrogation mechanism used should be compatible to established standard readout device.

Another report stated that a scanned fibre Fabry-Perot filter could be used for multiplexed sensor interrogation. It has the same 1με resolution we have

demonstrated and a sweep range of 50nm [105]. With the help of this technique, we can envisage a new kind of magnetic-field sensor.

4 FIBRE OPTIC DELAY LINE FILTERS EMPLOYING FIBRE BRAGG GRATINGS

4.1 Introduction

The low loss and broadband characteristic of optical fibre has lead to more and more research in the area of distributing and control of RF, Microwave and Millimetre wave signals using photonic technique. Such as personal communications networks and millimetre-wave LANs [22], microwave signal processing [149, 157] and phased array antennas [129]. Another example is a fibre-optic micro-cellular radio system having been investigated for portable radio communication systems [130]. With the progress in microwave and optical component development, the radio-on-fibre systems at higher frequencies will become practical in the future. In particular, systems using high frequencies such as 60GHz signal are of particular interest as they allow for excellent frequency reuse [131].

4.2 Signal Processing In Optical Domain

Microwave signal processing in optical domain using optical fibre has several advantages over the signal processing in electrical domain using conventional coaxial or waveguide method [132]. These advantages include low and constant attenuation over the entire modulation frequency range, immune to electromagnetic interference, wide bandwidth, low dispersion and high information transfer capacity [133]. With these advantages, these optical-domain-signal-processing techniques are currently being investigated for a number of microwave photonic applications. The advantages have been recognised, particularly for some military systems for which high bandwidth point-to-point fibre links are now being developed [134].

Recirculating and nonrecirculating delay-line filters have been used as the basic format for a variety of devices that have used many different delay media. For example, delay-line filters can be built by simply connecting lengths of coaxial cable or waveguide. Acoustic-wave delay-line devices are perhaps the most widely used approach for signal-processing applications [135,136]. The most versatile and sophisticated of the acoustic delay-line devices are those that use surface acoustic waves (SAW's) [137]. Planar processing techniques can be used to fabricate SAW transversal filters that have thousands of taps and can be operate at frequencies as high as 2 GHz [138]. Superconductive stripline filter was also been reported to achieve a bandwidth of 3 GHz.

There are early reports on processing microwave/millimetre wave signal using optical fibre [139,140]. The low loss and low dispersion of single mode fibre allows signals to propagate large distances without significant attenuation or distortion. This low-loss feature also enables long delay line, which can produce very small filter free spectral response.

Wilner and Van den Heuvel [140], who noted that fibre delay lines were attractive due to their low dispersion, proposed the use of optical fibre as a delay medium for signal processing applications. Ohlhaber and Wilner [141] reported an experimental demonstration of an optical fibre transversal filter. An optical fibre frequency filter was demonstrate by Chang, Cassaboom, and Taylor [142], who illuminated a bundle of fifteen multimode fibres that provided fifteen different delays spaced by 5.2 ns. The outputs from these fibres were incident on a single detector yielding a filter with a transfer function having a fundamental passband at 193 MHz. Many specific applications of optical fibre delay-line filters have since been proposed by Taylor [143] and others. These previous demonstrations of optical fibre delay-line filters have used individual multimode fibre delay paths from source to detector. These devices are therefore subject to the bandwidth limitations of multimode fibre (~1 GHz-km) and, in some implementations, are limited to a small number of taps due to the practical difficulties of uniformly illuminating and detecting light from a large number of bundled fibres. Thus, if the full potential of optical fibre delay lines is to be realised, it is necessary to make devices featuring many taps on a single-mode fibre delay line. In this way, the extremely large bandwidth and low loss of single-mode fibre can be exploited.

The next two sections are devoted mainly to establish the background needs to analyse our FBG based microwave photonic systems. In 4.3 and 4.4, we introduce two characteristics of our microwave photonic system, that is positive and incoherence nature. Following this, in 4.5, we introduce the advantages and disadvantages of FBG transversal filter over other forms of transversal filters. In 4.6, the fabrication of FBG array transversal filter is described in detail. Then the effort is turned to improve the filter performance with filter apodisation and tap multiplexing. Last, suppressed carrier effect is introduced.

4.3 Positive Nature Of Microwave Photonic System

Microwave photonic system is a positive system and has the feature of being consistent with intuition. For example, the following conclusions are demonstrated [144]:

1) At frequencies for which $\omega T=2n\pi$ (n=0,1,2...) the signals add constructively in the system, it is not the case for other frequencies. Therefore, the magnitude of the transfer function should have its maximum value at frequencies which are integer multiples of $1/T$.
2) The impulse response of a positive system is always real and positive-valued. It is equivalent to a system whose power spectrum is positive for all frequencies. Therefore, the transfer function at the origin is maximum and positive. This means we cannot make high-pass filters with positive systems, since these filters should be able to reject the low-frequency components of the input signals.

4.4 Incoherent System

There are two classes of photonic signal processors: coherent types and incoherent types. The advantage with coherent processors is that they can have arbitrary functions, which needs negative coefficients. However, they are sensitive to the phase of the optical carrier, which is difficult to control and stabilise [145]. Incoherent processors operate on the modulation of the light intensity and can provide highly stable transfer functions. For this incoherent processor, the optical source coherence length must be shorter than the time

delay differences encountered in the optical system. This is a vital point. The interference of optical carrier not only induces intensity noise but also degrades the microwave signal.

A unique advantage of optical fibre delay-line signal processing which is different from other delay-line techniques is that the frequency of optical carrier is thousands of times greater than that of the highest signal frequency component. Optical detectors are square-law devices that respond to the incident optical power and none is fast enough to respond to the carrier frequency. This is in contrast to the situation encountered in a surface acoustic-wave delay-line, where electrodes with spacing corresponding to the spatial period of the acoustic carrier directly detect a propagating acoustic wave. The propagating acoustic wave induces a voltage on the electrodes proportional to the amplitude of the acoustic wave at that point.

In principle, coherent processing can be fulfilled within fibre-optic delay-line system. In this case, the relative phases of the optical carrier of each tapped signal must be maintained within a fraction of an optical wavelength. This requires a narrow spectrum source that is highly stable. In addition, differences in optical paths must be constant to within a fraction of an optical wavelength. Such coherent systems can be difficult to implement in practice and are usually more complicated than incoherent systems because of the stringent requirements on the stability of the source and optical delay paths. For this reason, coherent detection is avoided in single-mode fibre delay-lines.

To ensure minimum coherence of optical carrier, spatial and temporal averaging of the carrier can be employed [146]. When a temporally coherent carrier incident on a detector from different angles, there exist a phase variation in the plane of the detector. This phase variation is quite large for small angular separations. Even without averaging, temporal averaging can be used with a broad band source. Even if the outputs from a delay-line processor are spatially coherent, the frequency components of the carrier will beat against each other and be effectively averaged over time. The necessary condition for obtaining temporal averaging is given by:

$$\tau_c \leq T_{\text{int}} \leq T_0$$

Equation 4-1

where T_0 is the time delay between tap signals. T_{int} is the integration time of the detector, and τ_c, the coherent time of the carrier, is given by $\tau_c \sim 1/\Delta\nu$.

Semiconductor laser diodes can present both a broad spectrum and the ability to be directly modulated at speeds up to several gigahertz. Therefore, they are the best choice for optical fibre delay-line applications.

4.5 Features Of FBG Based Fibre-Optic Delay-Line Nonrecirculating Filter

According to impulse response, filters can be classified into two classes, namely, infinite impulse response (IIR) filter and finite impulse response (FIR) filter. We will see that IIR filters are usually implemented using structures having feedback (recursive structures) and FIR filters are usually implemented using structures with no feedback (nonrecirculate structures).

There are many reports on fulfilling the fundamental functions of a transversal filter. They can be classified into conventional electrical transversal filters and photonic transversal filters.

The electrical filters, as mentioned before, can be built using coaxial cable, microwave waveguide, surface acoustic wave technique and superconductor stripline. The advantages with these filters are in that they have mature fabrication technique that can be used for mass-production to reduce the cost. Furthermore, negative coefficient can be achieved. However, compared with photonic filter, electrical filters are inherited narrowband, high loss, and inflexible. In the early stage, there are pioneering scientists building microwave photonic filter using optical fibres [146]. These include discrete high dispersion fibre [147,148], unbalanced Mach-Zehnder structures [149,150,151]. With the invention of FBG, a new type of FBG based microwave photonic filter has emerged [157,152]. This FBG type filter not only has the advantages of large bandwidth, low loss and immunity to electromagnetic interference over electrical filters, but also has the merits of easy apodisation, reconfiguration and tuneablility over optical fibre type photonic filters. Typical schemes of

transversal filters of optical fibre and FBG forms are shown in Figure 4-1. The optical fibre type filter is straightforward in principle. It contains a 1×n splitter, n optical fibre delay-lines of incremental length and an n×1 combiner. The FBG structure consists of a 1×n splitter and a FBG array. The FBGs having the same Bragg wavelength form one set of transversal filter. Each set of transversal filter can have different number of FBGs to achieve different frequency resolution. FBGs can also have different reflectivity to fit apodisation functions. All these will be experimental demonstrated later. Due to this structure difference, FBG has combined the several advantages of performing transversal filter functions such as filter reconfiguration, tap apodisation and tuneability.

Filter reconfiguration means the transversal filter consists of different number of taps to achieve different frequency response. Changing the number of taps, the passband of frequency response become narrower while the rejection band become broader. According to requirements, we can adjust the number of taps to perform either band rejection or band pass. Figure 4-1 shows the structure of optical fibre type and FBG type transversal filter. Using optical fibre, different number of taps can only be achieved by individual sets of filters. While using FBG arrays, different number of gratings can be embedded into the arrays. Each set of gratings can be addressed by choosing individual Bragg wavelength.

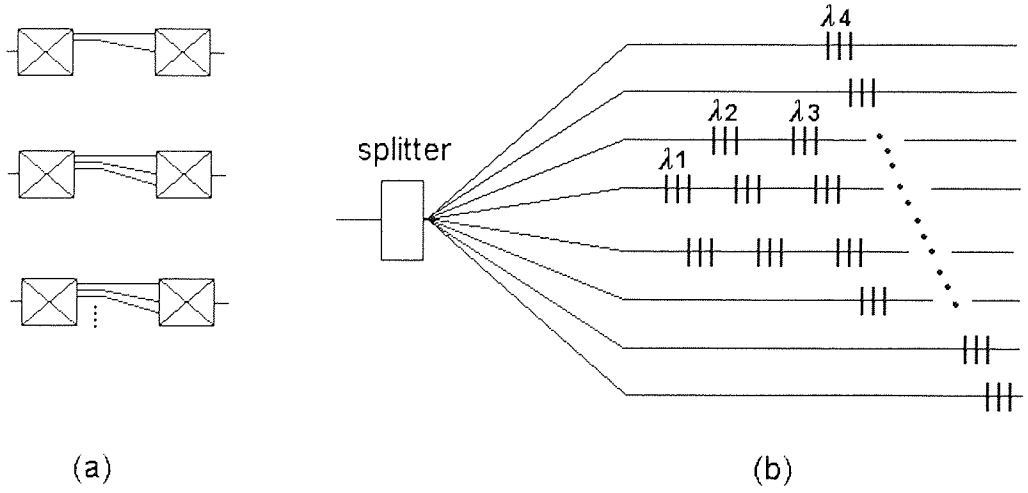

Figure 4-1. Reconfiguration of two different kinds of filters (a) optical fibre filter using discrete set of filters; (b) fibre Bragg grating using different number of gratings.

As for filter apodisation, both simple optical fibre and high-dispersion fibre structure need discrete sets of filters to fulfil. While for FBG structure, the gratings can be made with designed reflectivity to fulfil apodisation.

There are several characteristics of tapped delay line processors, for example time domain resolution and frequency domain resolution. High time domain resolution can be achieved with short sampling time-that is using short unit-length delay line. The processor sampling frequency is determined by the minimum delay step size. The processor sampling frequency is given by

$$f_s = \frac{1}{\tau}$$

Equation 4-2

In other words, high sampling frequencies can be realised with very short delay lines. Grating elements can be used in this situation. Figure 4- 2 shows two fibre-based sampling techniques. The discrete fibre Bragg grating array for time delay processing of signals is shown in Figure 4- 2 (a). In order to achieve high reflectivity, the minimum practical centre-to-centre grating spacing is around 1 mm, resulting in a minimum delay step size of 10ps. This corresponds to a sampling frequency of 100GHz. This 10ps delay step is the practical low limit on the delay step size that can be produced through the use of discrete Bragg grating array delay lines [153].

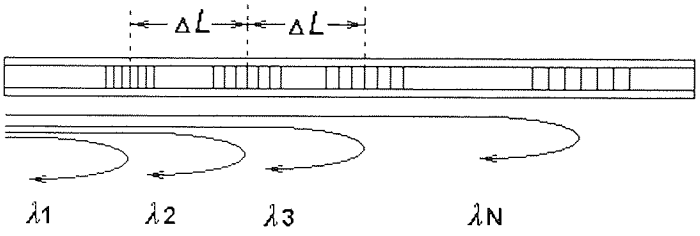

(a) Discrete grating array

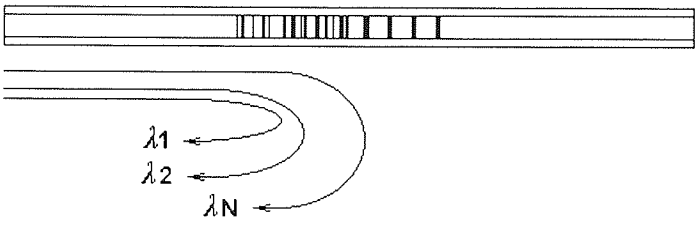

(b) Overlapped grating array

Figure 4- 2. Fibre Bragg grating based sampling element.

There is a new scheme reported [154] to reduce this delay step. As shown in Figure 4- 2 (b). Several uniform grating of different wavelength is overwritten in the same length of fibre. The effective reflection point for each wavelength is controlled by selecting a different source wavelength. In this way, very small delay increments, potentially below 1ps, can be obtained. Such gratings have been designed having a 24mm total length with 14-mm full width at half maximum [154]. The shortest measured delay step is 2ps. This corresponds to a sampling frequency of 500GHz. Note that the microwave photonic system we study here is an incoherent system, so the coherence length of optical source limits the time domain resolution. It is needed that the unit delay length be larger than the optical source's coherence length to avoid optical carrier beat noise.

In order to obtain a high resolution in the frequency domain, a large number of taps is required. According to Equation 2-50, we can simulate the filter frequency response with the filter having different number of taps, as in Figure 4-3.

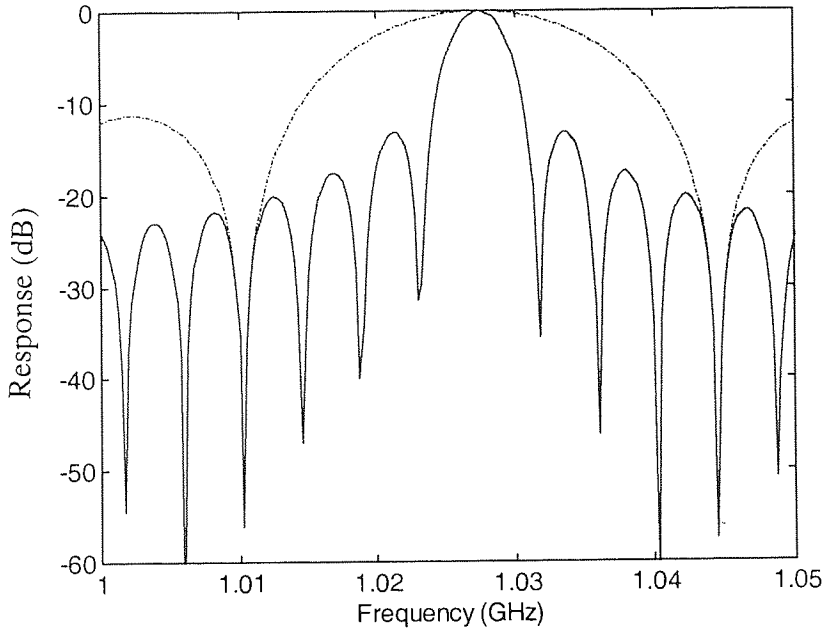

Figure 4-3. Filter frequency response for a filter with 4 taps (broken line) and 16 taps (solid line).

We can easily notice that, in the frequency response, the filter with 16 taps has a narrower passband. That means a better frequency resolution has been achieved with a larger number of taps.

4.6 Filter Set-up And Improvement

The system configuration is shown in Figure 4-4. This transversal filter was designed to have eight taps. Compared with another reported structure [155] in our group, this design combines the advantage of better frequency resolution and performance improvement potential.

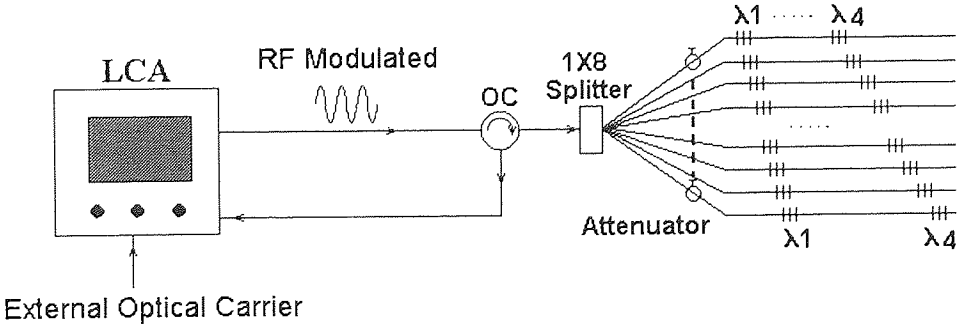

Figure 4-4. Experimental set-up of FBG array microwave transversal filter.

The filter construction was carried out in two steps. First, a 1×4 splitter was selected and one grating spliced onto one output port. The LCA was set to time-domain measurement mode, as in Figure 4- 5. So the LCA show a pulse reflected by this grating. Setting a cursor on the maximum of this pulse, the length reading was the distance from the grating to LCA, which now acted as a reference. One point to note is that the measure range of the LCA should be carefully selected. The measure range should be long enough to include the optical pulse and short enough to give a good resolution. Then knowing the length, second grating of same wavelength was spliced on. Since the accuracy of grating incremental spacing is important to filter performance, the successive grating splicing was divided into two steps. First, the length of the fibre was calculated. Then a fibre of 15 cm longer than the designed length having the second grating was spliced on. Because the grating spacing was usually over three metres in this experiment, we won't acquire grating spacing that is accurate enough if one-step splicing is used. A second pulse would appear on LCA after the fibre was spliced on the splitter. Again, the LCA measure range should be adjusted to include only the second pulse to give a better resolution. Then the accurate distance from the grating to LCA (reference) can be measured using the same method as in measuring the first pulse. Knowing the length to be cut, the first step was to cut the fibre, leaving enough length to be cleaved. Then the fibre was spliced on again. We can normally control the grating spacing accuracy within 1mm of optical path. The third and fourth grating were splice on using the same method.

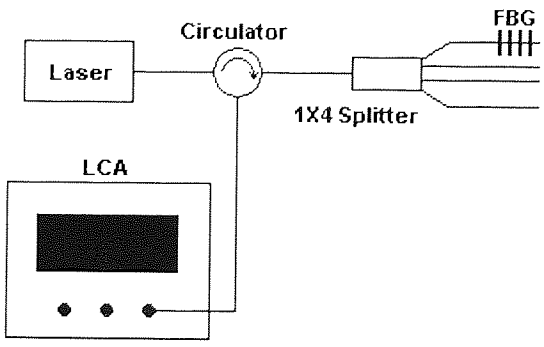

Figure 4- 5. Diagram showing FBG array construction process.

The second step towards the construction of this filter was to built another 4×1 grating array as the first one. Then the first set of 4×1 grating array was spliced onto one output port of a 1×2 splitter. A calculated length of fibre together with the second set of 4×1 array of gratings were spliced. The fibre was selected to let the spacing between the last grating of the first array and the first grating of the second array was the same as other grating spacing. As in Figure 4- 6, $L_1=L_2$.

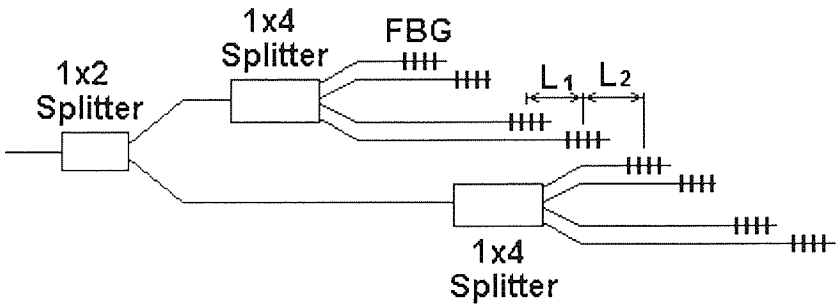

Figure 4- 6. Experimental set-up of 8×1 grating array consists of two 4×1 grating array.

The tuneable source used is an external cavity Fabry-Perot semiconductor laser. The tuning range is from 1530nm to 1560nm with a step as small as 0.001nm. Each of the grating arrays is connected via an adjustable attenuator that adjusts the tap weighting (windowing of pulses) to provide different bandpass spectral profiles. Each of the eight grating arrays correspond to eight taps of the microwave photonics signal. A Lightwave Component Analyser (LCA) provided both electro-optic modulations (EOM) at up to 20 GHz and photodetection and was used to measure the filter response both in time and frequency domain. Finally the filter can be assessed using the LCA and the set-up is as Figure 4-4.

In the experiment, only strong uniform gratings were used. The filter apodisation is achieved through the attenuator on each arm. In practical case, the gratings can be made with desired reflectivity so that various apodisation functions can be fulfilled at the filter fabrication process.

4.6.1 Time Domain Measurement

In order to assess the filter's quality, the filter's time domain measurement was first carried out. In the first instance, there are inevitably variations in the tap intensities. This is mainly caused by the optical carrier partial coherence noise and variations of coupling ratios. The carrier beat noise will be analysed later. The pulse intensity variation can be corrected by adjusting the attenuator on each arm. By adjusting the measure range, the grating's relative distance (relative to LCA) was measured again. This data can be used in the simulation of filter frequency response. Figure 4- 7 is the filter's measured impulse response. Note that the intensities of each pulse were adjusted through attenuators.

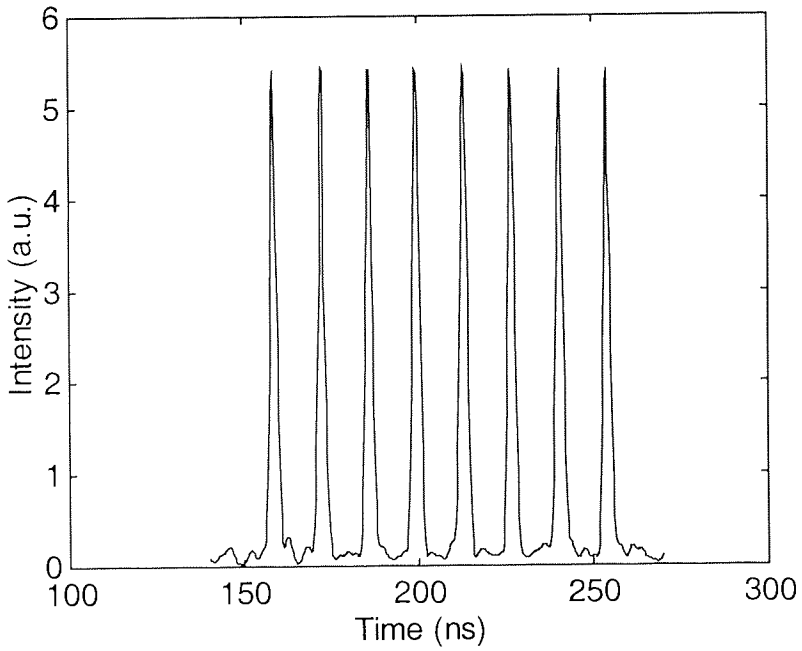

Figure 4- 7. Filter impulse response measurement. The intensity variations have been corrected by adjusting the attenuators.

4.6.2 Frequency Domain Measurement

The LCA can also be used to measure the filter frequency response. When the filter had eight taps, the experimental result, shown in Figure 4-8, fits well with theoretical prediction. We can notice that the experimental curve deviate considerably from theoretical calculated curve at null points. This is because

the theoretical model takes ideal condition that the incremental delay are of absolute accurate and pulse intensities are of absolute equal. This condition can not be satisfied in real implementation and bring about the frequency response deviation at null points.

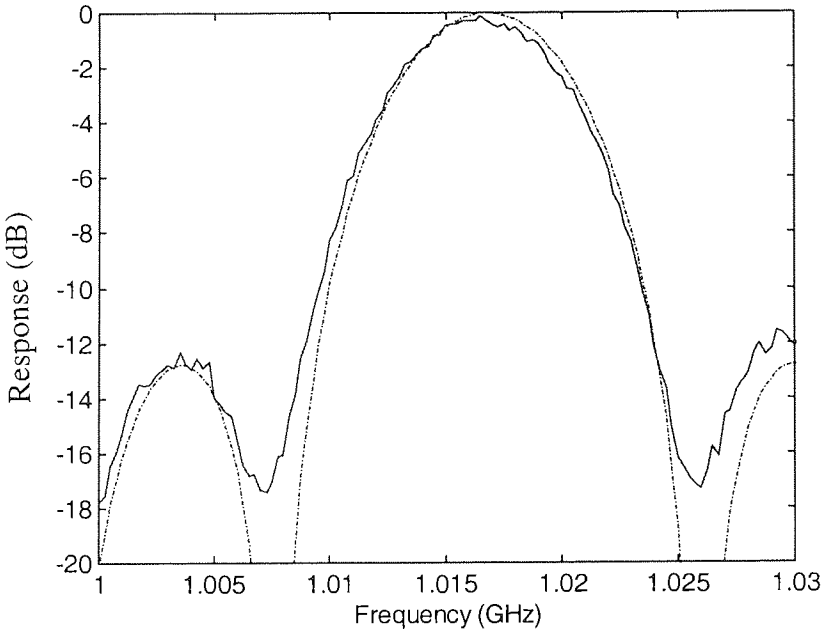

Figure 4-8. Filter frequency response corresponding to the impulse response in Figure 4- 7. Solid line is the measured result. Broken trace is the theoretical simulation.

4.6.3 Apodisation

The aim of filter apodisation is to improve its performance. The primary advantage of FBG type transversal filter over optical fibre-type transversal filter is in its easy apodisation characteristic. Referring to filter window design method, high extinction ratio can be achieved by appropriate weighting of impulse response, as in Figure 4-9 and Figure 4-10. Proper tap weighting (windowing) results in a decrease of the secondary sidelobes to the filter and thus a better extinction ratio. In this experiment, the apodisation is achieved in the following process. First, find the desired intensity of every pulse. This can be facilitated by Matlab software. There are some built-in apodisation functions. With the input of number of pulses, the corresponding pulse intensities are given. The next step was to adjust the intensities of pulses reflected from gratings. In this experiment, the fibre was bent to achieve desired intensity.

This saved a large number of attnuators and we can achieve apodisation functions.

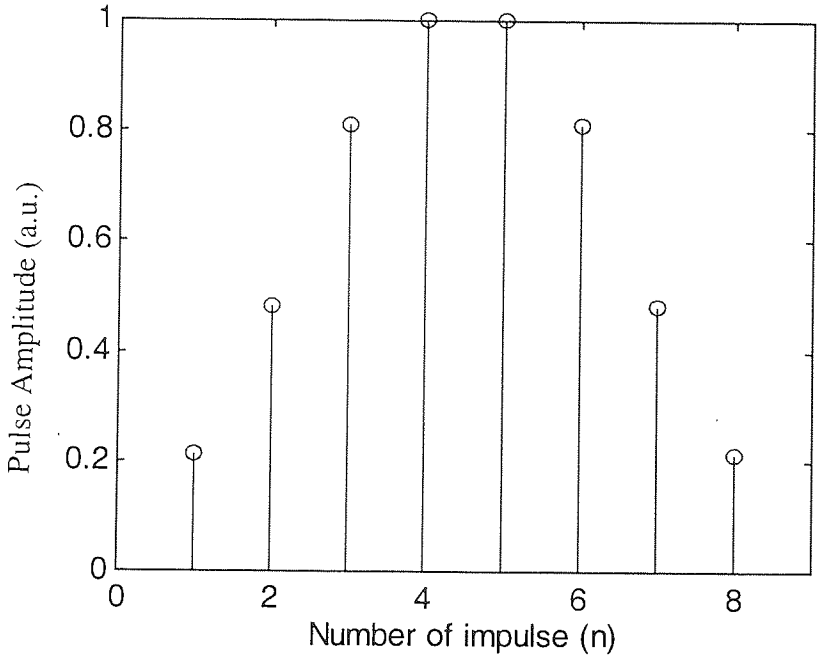

Figure 4-9. Filter impulse response when using Hamming window apodisation.

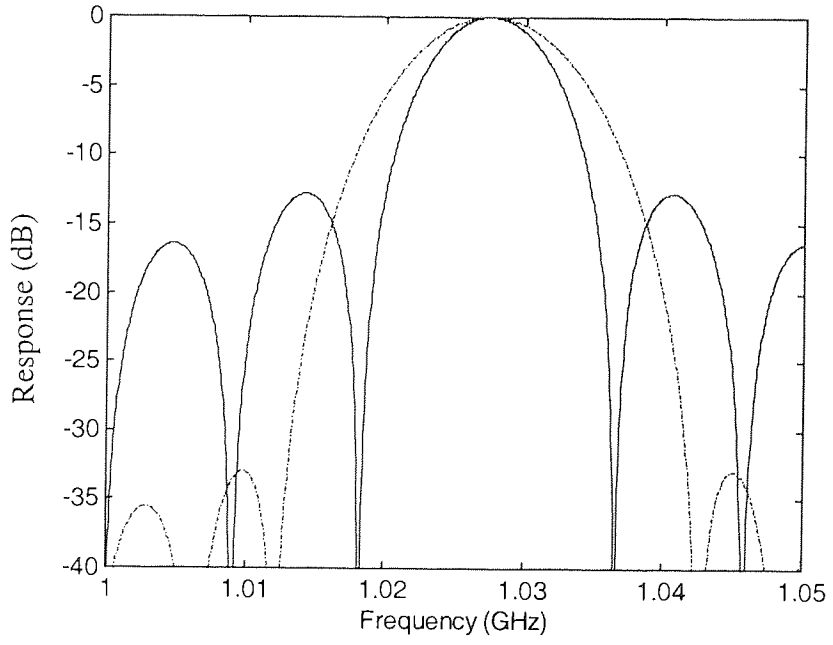

Figure 4-10. Filter frequency response when using Hamming window apodisation (broken line) and equal tap (solid line).

Prior to experimentally fulfil filter apodisation, we listed below several apodisation functions and the comparison of the frequency response when using these functions.

Bartlett profile:

$$f(z) = \sqrt{3}z + \frac{\sqrt{3}}{2} \quad (-\frac{1}{2} \le z < 0)$$
$$f(z) = -\sqrt{3}z + \frac{\sqrt{3}}{2} \quad (0 \le z < \frac{1}{2})$$

Equation 4- 3

Hamming profile:

$$f(z) = \frac{1 + H\cos\left(\frac{2\pi z}{L}\right)}{1 + H}$$

Equation 4- 4

Blackman profile:

$$f(z) = \frac{1 + (1 + B)\cos\left(\frac{2\pi z}{L}\right) + B\cos\left(\frac{4\pi z}{L}\right)}{2(1 + B)}$$

Equation 4- 5

The profiles are plotted in Figure 4- 11.

The filter frequency response when using these apodisation functions is plotted in Figure 4- 12. We can notice the difference of the extinction ratio and bandwidth we have obtained. In Table 4-1, we have listed the results of measured extinction ratio and bandwidth. It is obvious that there is a trade off between filter extinction ratio and bandwidth. Normally, a better extinction ratio results in a larger bandwidth, which means poor frequency resolution.

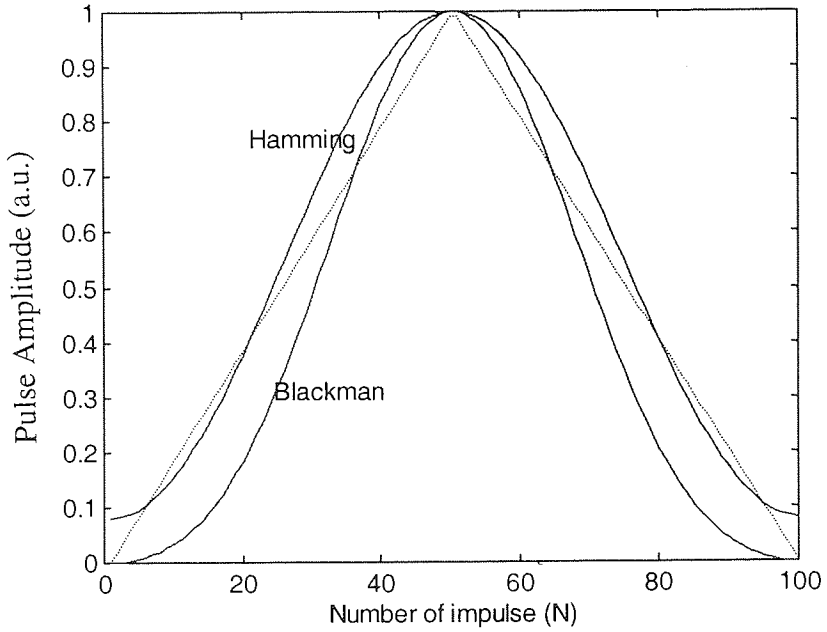

Figure 4- 11. Profiles of three apodisation functions. Bartlett window (triangle with dotted line), Hamming window (outer solid line) and Blackman window (inner solid line).

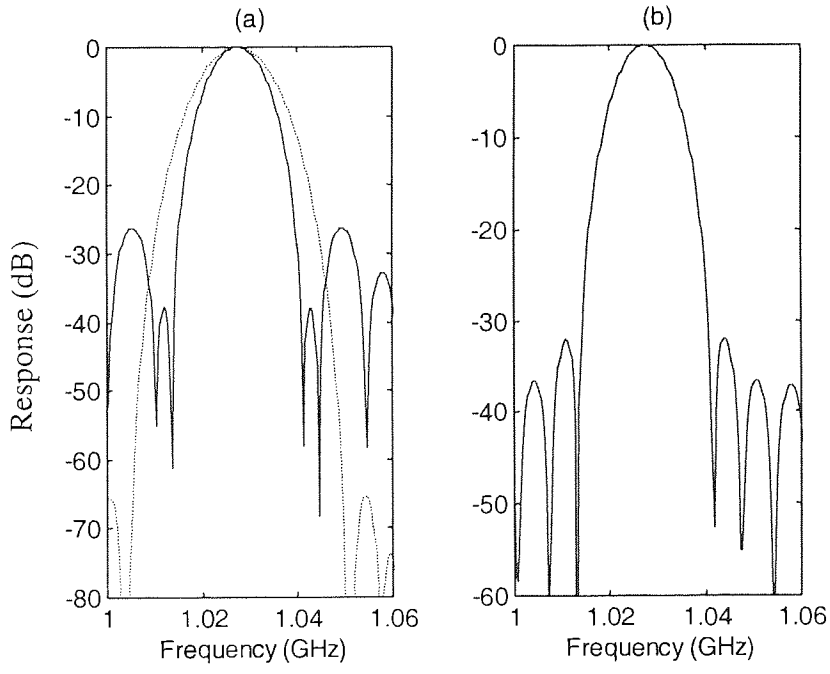

Figure 4- 12. Simulated filter frequency response when using apodisation functions shown in Figure 4- 11. Bartlett window (Solid line in (a)), Blackman window (Broken line in (a)), Hamming window (b).

Table 4-1. List of window function, resulting filter extinction ratio and 3dB bandwidth (tap number = 8).

Name of window	Extinction ratio (dB)	3dB bandwidth (MHz)
Bartlett	26.5	14.3
Hamming	32	13.6
Blackman	65	16.7

Here, experimentally, we adopted a Hamming window profile as shown in Figure 4-9. This was implemented by tuning the attenuator on each grating array. We can see the simulated filter frequency response in Figure 4-10 and the estimated extinction ratio and bandwidth in Table 4-1. The extinction ratio and 3dB bandwidth are given according to our fibre Bragg grating based transversal filter with 8 taps. We have good agreement between theoretical (dashed line) and experimental results (solid line), as shown in Figure 4-13. The measured bandwidth is slightly different with the theoretical prediction, due to small deviations of the tap weighting from the ideal Hamming profile. Note that the extinction ratio has reached 30dB, as compared to the case of equal tap weighting of 13 dB [147,155], and 25dB with Hanning apodisation [156]. Note that this filter response is measured RF intensity response other than amplitude response. As we have said before, the extinction ratio can further be increased by adopting other windowing function at a price of increasing the passband width. However, we have noticed that it is more difficult to achieve the 30-dB extinction ratio when using Hamming window than achieve 13-dB extinction ratio when the filter has equal tap. What we mean difficulty here is that we need to take great care of pulse intensity and grating incremental spacing. That means this higher performance has left fewer margins for us. In order to reach the limit of this margin, we decided that a Blackman apodisation function should be used. This is because a larger extinction ratio (ideally 65 dB) should be derived.

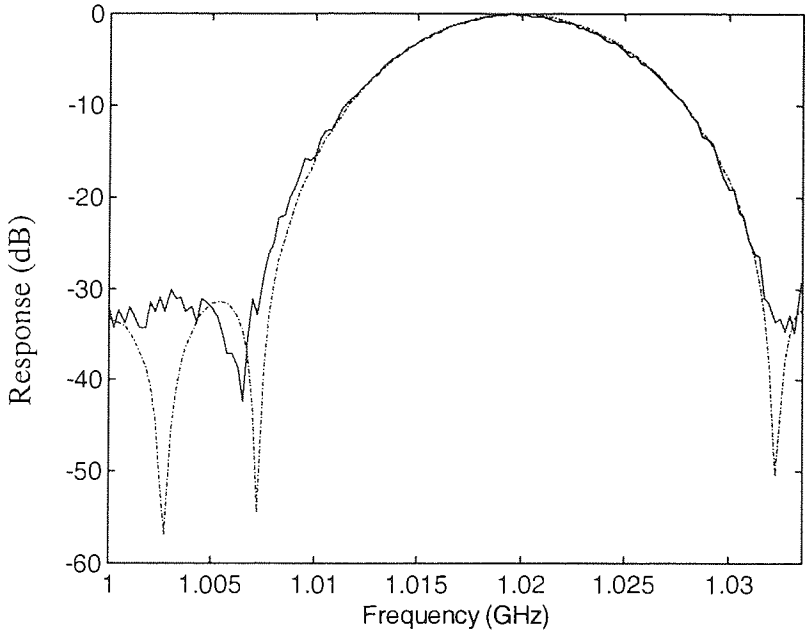

Figure 4-13. Experimental result for the filter with Hamming window function, dashed line: theoretical prediction.

4.6.4 Error Analysis

The same method was used to implement Blackman apodisation as that for Hamming apodisation. The frequency response of the filter is shown in Figure 4- 14. This was the best filter-extinction-ratio we have obtained. However it is still far from the simulated result, which is 65 dB as in Table 4-1. That means the intrinsic noise of this system has limited the filter's extinction ratio level.

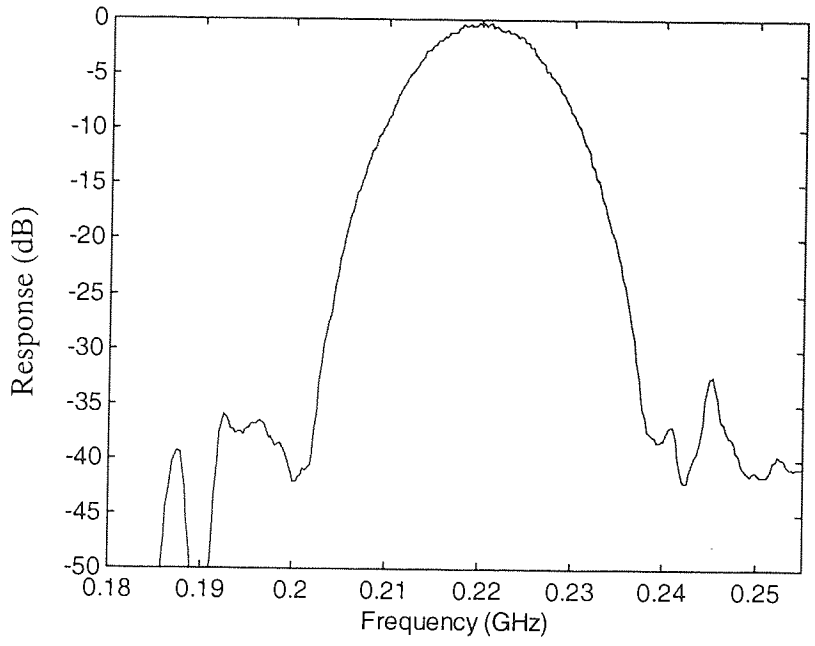

Figure 4- 14. Filter frequency response when using Blackman apodisation.

In addition, it was noticed that the reflected pulse has certain intensity variation despite that the grating has been temperature isolated. It was estimated that this noise originates partly from optical-carrier-partial-interference noise. As we have said before, our system worked in incoherent state. That is, the unit-delay length should be far longer than the coherent length of optical source (2.8m in this instance). In order to study this noise, we select the unit-delay length equal to the coherent length. Therefore, partial interference between the optical carriers is inevitable. The idea of this experiment is to increase the number of optical carriers gradually, and then the intensity of the pulses is recorded to study the intensity variation brought about by partial interference. In the beginning, seven gratings out of a set of eight were attenuated to be off, and the LCA set to measure filter impulse response. The cursor was at the peak of the pulse. The standard deviation of the pulse intensity was calculated. Following this, a second grating is tuned on. Again, the standard deviation of the pulse's intensity was calculated. The other gratings were released in sequence and the measured results are show in Figure 4-15.

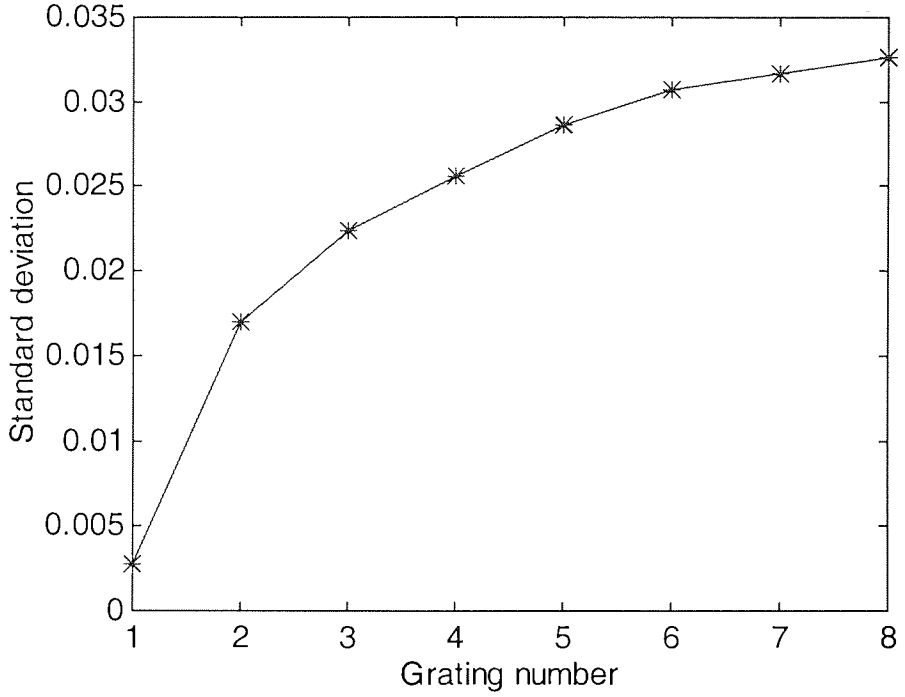

Figure 4-15. Standard deviation of grating reflection intensity against grating number.

In Figure 4-15, Y-axis represents the standard deviation of signal's pulse intensity. It reflects the degree of variation of signal's intensity. X-axis represents the number of gratings used in the system.

When the filter consists of only one grating, the standard deviation of signal pulse intensity (100 values) was 0.0028. This value increase to 0.0169, 0.0224, 0.0256, 0.0287, 0.0307, 0.0317, 0.0326 respectively corresponding to filters with 2, 3, 4, 5, 6, 7, 8 gratings. As we have seen, the degree of variation of signal's intensity increases with the adding of grating element. This can be explained that optical partial interference noise enhances with the increasing of number of optical pulses existed in the system. Therefore, we derive the conclusion that optical-carrier-partial-interference noise degrades the filter's performance. Considering the unit-delay-length variations measured in the experiment and the pulse intensity variation, we obtain the simulation result that the filter can only have a maximum extinction ratio of 35dB, as in Figure 4-16. While the filter with ideal impulse response have extinction-ratio of over 60 dB. This 35dB simulation explains our experimental result in a published paper [157].

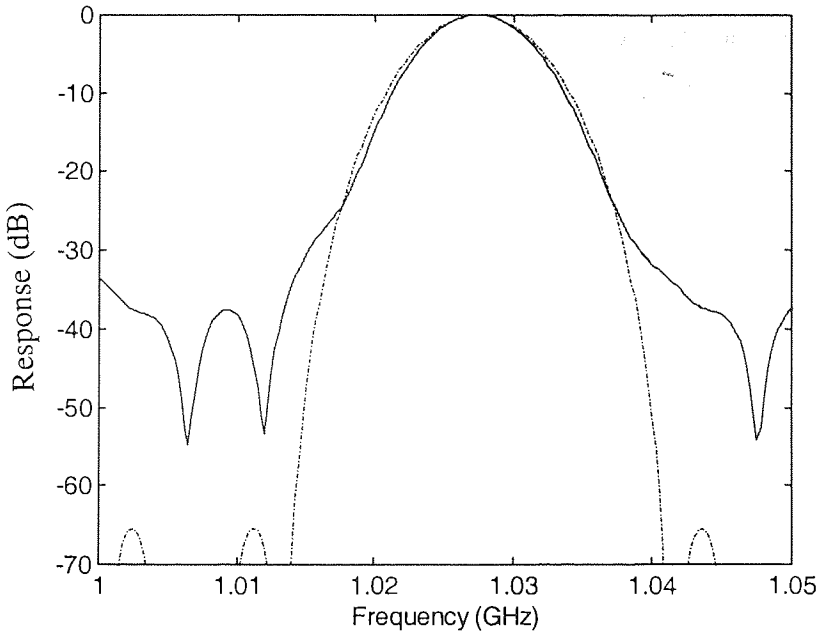

Figure 4-16. Comparison of performance of filter having ideal impulse response (broken line) with that affected by unit-delay-length errors and pulse intensity variations (solid line). (Blackman apodisation).

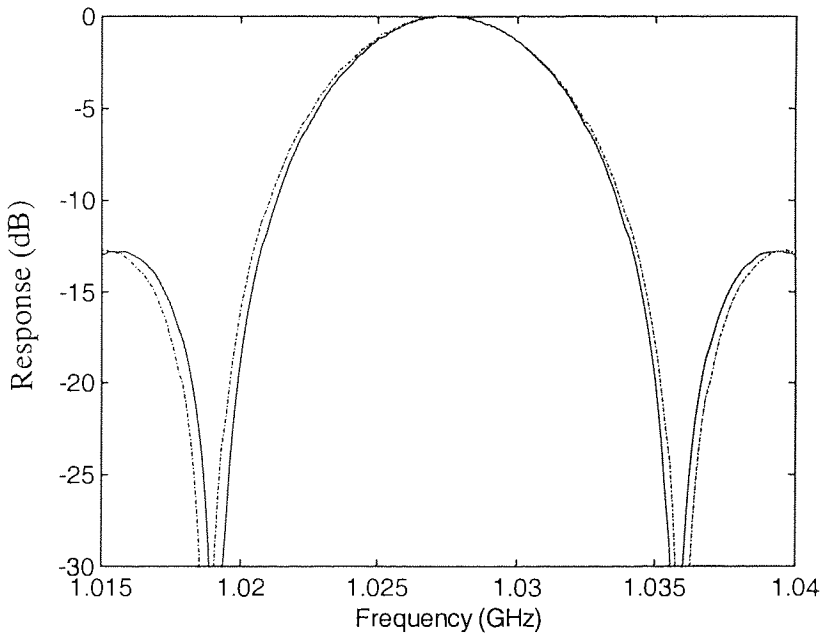

Figure 4-17. Comparison of performance of filter having ideal impulse response (broken line) with that affected by unit-delay-length uneven and pulse intensity variation (solid line). (Equal tap).

Next, the consideration is moved to the degree of effects these detrimental factors can bring about to this system. From the pervious experiment, we felt

less harassment when the filter has equal taps. Therefore, we brought the same grating incremental length and pulse intensity variation into simulation software. As in Figure 4-17, we can notice that there is not much deviation than the Blackman apodisation condition as in Figure 4-16. This illustrates that high performance apodised filters require very tight component tolerance. It was calculated that when Blackman apodisation was used, the grating spacing has a variation of 1 mm optical path and pulse intensity has a variation of 0.1%, the best extinction this filter can achieve is 30 dB. 37-dB filter extinction can be achieved when these two variations are 0.5-mm for optical path and 0.05% for pulse intensity.

4.6.5 Filter Reconfiguration

In some applications, bandstop may be needed instead of bandpass, or different frequency resolution is specified. In other words, filter reconfiguration is required. For this FBG type transversal filter, reconfiguration can be implemented by employing different number of gratings as in Figure 4-1 (b). The filter reconfiguration was demonstrated by setting the operating wavelength at a specific value so that one set of gratings was chosen. First, we tuned the laser to λ_1 so that only the gratings in the first column have unity reflection. Others had no reflection. The measured frequency response is shown in Figure 4-18 (a). We can obtain different filter frequency response by changing source wavelength thus selecting different filter. As in Figure 4-18 (b), the laser was tuned to λ_2 and λ_3 when the number of gratings is three and four. Note we use the same grating spacing in this case so that the filter has same resonance frequency. However, the frequency resolution has changed due to the different number of gratings used.

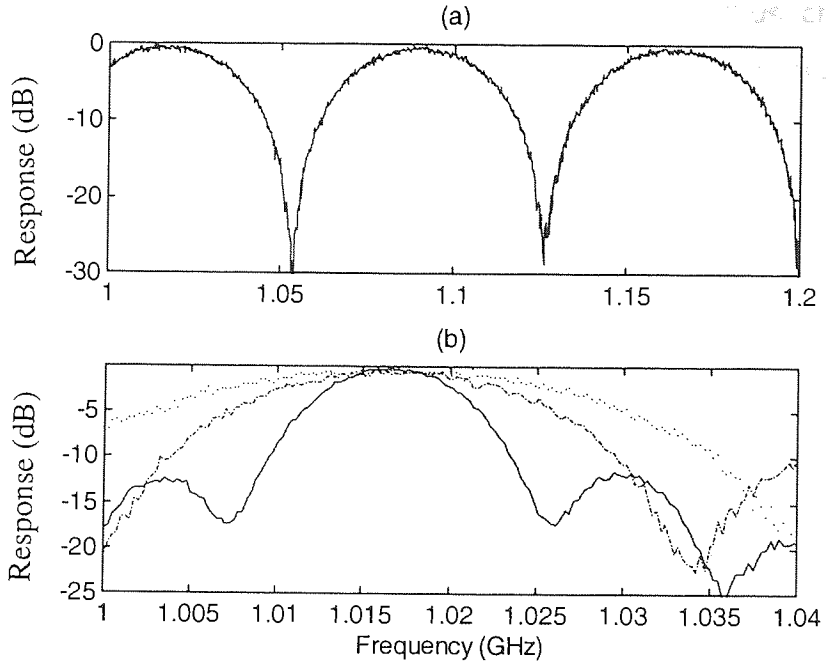

Figure 4-18. Filter frequency response with different number of taps. (a) two taps. (b) three taps (dotted line), four taps (dash dotted) and eight taps (solid).

Figure 4-18 (a) shows the transfer function modulus corresponding to a filter where the incremental spacing was 3m and all two gratings had equal weighting. Refer to Figure 2- 23 (a), we have good agreement with prediction at the rejected frequency. The rejection ratio is 30 dB. Not as good as simulation results because the intensity of the grating reflection changes randomly due to partial coherence interference. In Figure 4-18 (b), we can see that, with the increasing number of taps, the passband became narrower. That means we have better frequency resolution.

4.6.6 Tuneability

In many circumstances, it is desirable that the filter is flexible which means its (free spectral range) FSR is changeable rather than fixed. The FSR is inverse proportional to the incremental length of each grating. Note, as we mentioned before, that this incremental length must be larger than the coherence length of laser source to avoid optical carrier beat noise. In this experiment, the maximum FSR of the filter is determined by the coherence length of laser source, which is around 2.8 m. In order to demonstrate the filter tuneability, we build four sets of grating arrays with incremental length of 2.8m 3m, 3.5m and

4m. Tuned the optical carrier wavelength from λ_1 to λ_2, thus changing the grating increment from 2.8m to 3m. We can easily notice the change of free spectral range from the experimental results in Figure 4-19. Tuning the laser wavelength among the four grating sets, we have filter spectral spacing of 68MHz, 73MHz, 82MHz, and 102MHz.

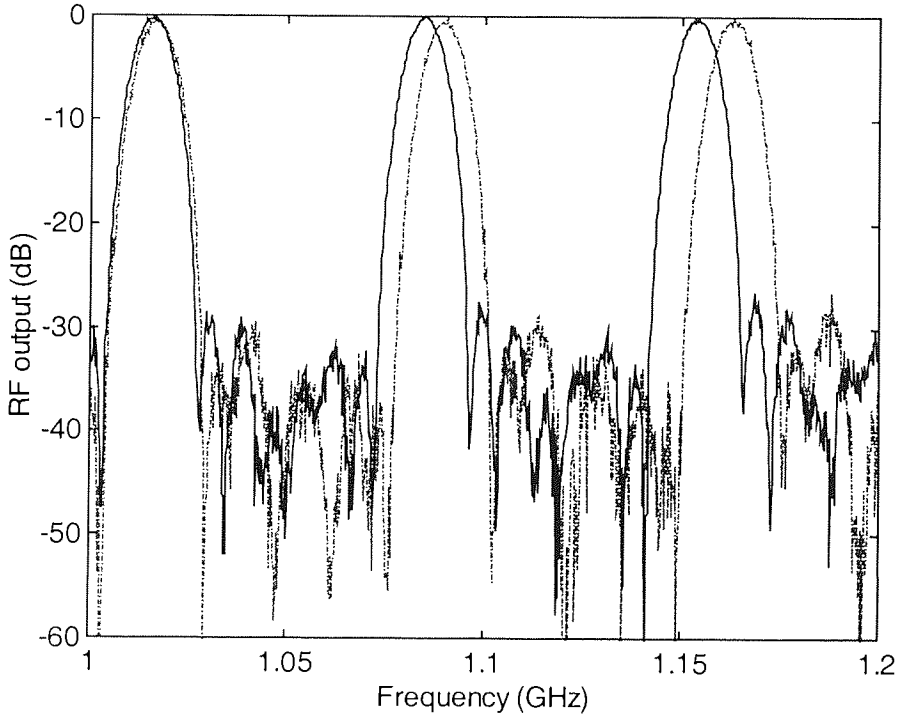

Figure 4-19. Filter response with different FSR of 102MHz (broken line) and 82MHz (solid line).

4.6.7 Tap Multiplexing

The filter frequency-domain resolution is determined by the number of taps. Increasing the number of taps enables improved performance, for example, high frequency domain resolution, increased Q factor and rejection level. Additionally it gives more options in terms of tap apodisation, enabling improved suppression of sidelobes in the frequency response.

A straightforward method is to increase the tap one by one. The obvious disadvantage involved is that it will bring more incremental length variation during the fabrication. The tap multiplexing method is our unique way to solve this problem. Furthermore, it is has an economical advantage in that we use

one fibre Bragg grating instead of eight to double the number of taps. In the next section, the experimental set-up and result is given. Following this, another attempt is to improve the filter extinction ratio.

Tap Multiplexing with Equal Tap

The schematic diagram of the tap multiplexing method is shown in Figure 4-20. Compared with original diagram (Figure 4-4), we noticed that there is a Mach-Zehnder device inserted at the output port of optical circulator. When one optical pulse is injected into the 1×8 splitter, 8 optical pulses reflected from the gratings of the same wavelength. This pulse train (equally positioned in time) goes towards the Mach-Zehnder structure and is further split into 16 equal-intensity pulses. One group of 8 pulses goes directly through the arm that has attenuator on which is used to adjust the pulse's intensity. The other 8 pulses goes through second optical circulator, reflected from another grating which is deliberately placed so that this 8 pulses are evenly queued after the 8 pulses that goes directly through the other arm. At the output, we now have 16 equal-spaced pulses. The measured impulse response and frequency response is shown Figure 4-21 and Figure 4-22.

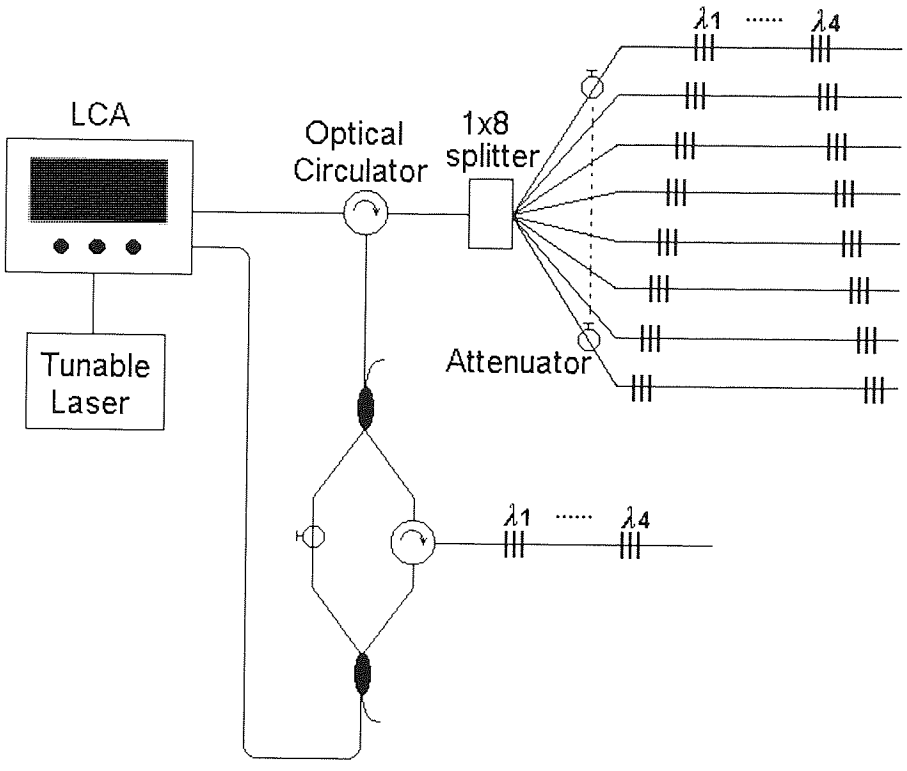

Figure 4-20. Experimental set-up of filter tap multiplexing.

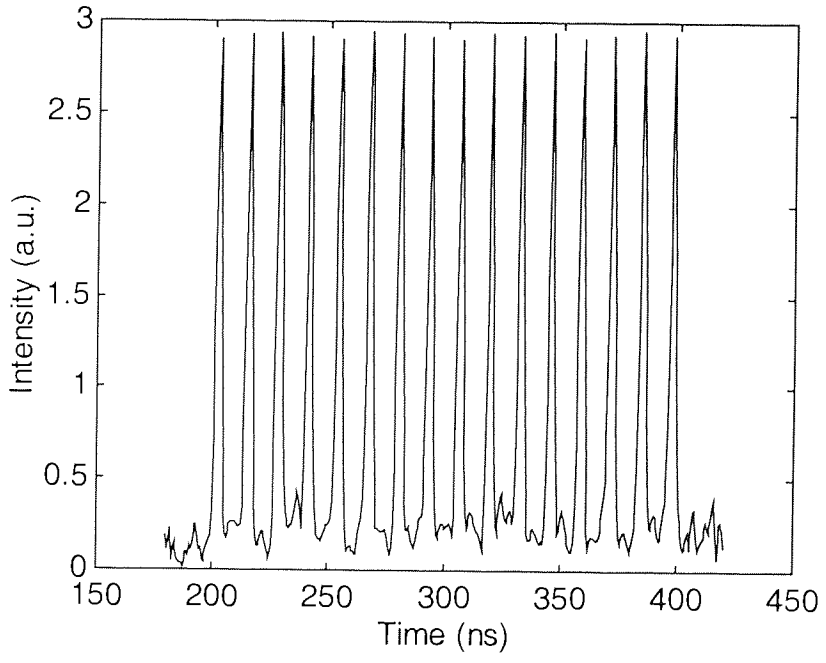

Figure 4-21. Measured impulse response of tap multiplexed filter.

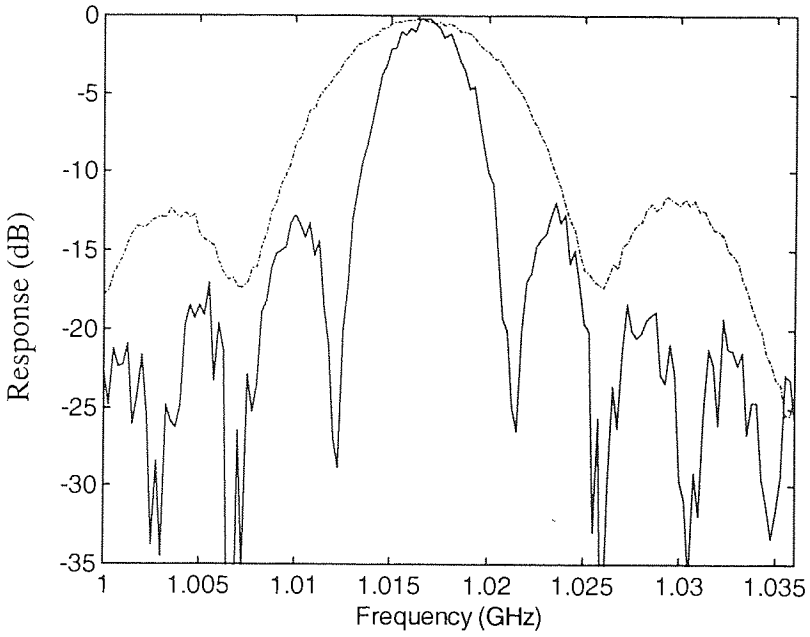

Figure 4-22. Frequency response of tap multiplexed filter (solid line) and original equal-tap filter (broken line).

We can easily notice the resulted better frequency resolution. With doubled number of taps, we should get a doubled better frequency resolution. This is also verified by experimental result (the 3dB bandwidth for original filter is 12.4 MHz, while the tap multiplexed filter has a bandwidth of 6.2MHz).

Tap Multiplexing with Apodisation

An obvious draw back of this tap multiplexing technique is that arbitrary tap weighting can't be achieved directly. For example, we apodised the eight taps using a Blackman function. In Figure 4-23, we see pulses 1~8 are those going directly through the tap-multiplexing device. These eight pulses sampled a whole Blackman function. Pulses 1'~8' are those being delayed. They also sampled a whole Blackman function. The resulting superimposed multiplexed taps drop in the centre, as in Figure 4-24. Other than giving a smooth bandpass frequency response, the modulus have dips on passband which is not ideal.

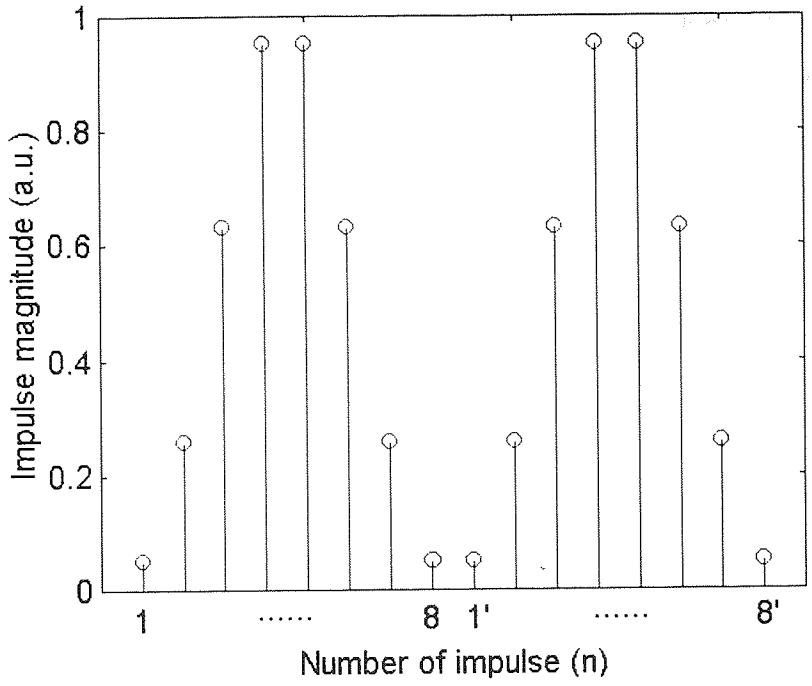

Figure 4-23. Direct tap-weighting result in a middle-dropped weighting shape.

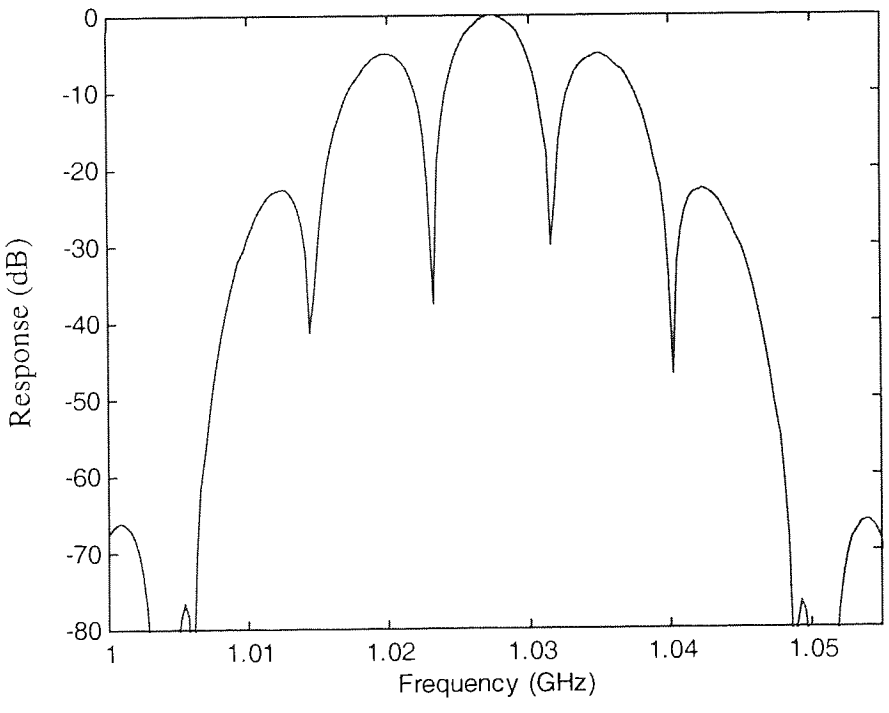

Figure 4-24. Frequency response of a filter with impulse response as shown in Figure 4-23.

A solution to this problem is to insert the delayed pulses into those undelayed. This is achieved by using accurate delay line to ensure that the delayed pulses are placed just in the middle of the correspondent undelayed pulses and the

successive ones. This is shown in Figure 4-25. Pulses 1, 2, 3...8 are undelayed. 1', 2', 3'...8' are delayed pulses. Note, in this condition, the unit delay length of each grating have to be readjusted to avoid optical carrier beating.

Since these pulse pairs (e.g. 1 and 1') have same magnitude, these pulses can't fit exactly of an apodisation. As in Figure 4-25, the dotted line represents a Blackman profile, which should be fitted by those pulses 1, 1', 2, 2'....

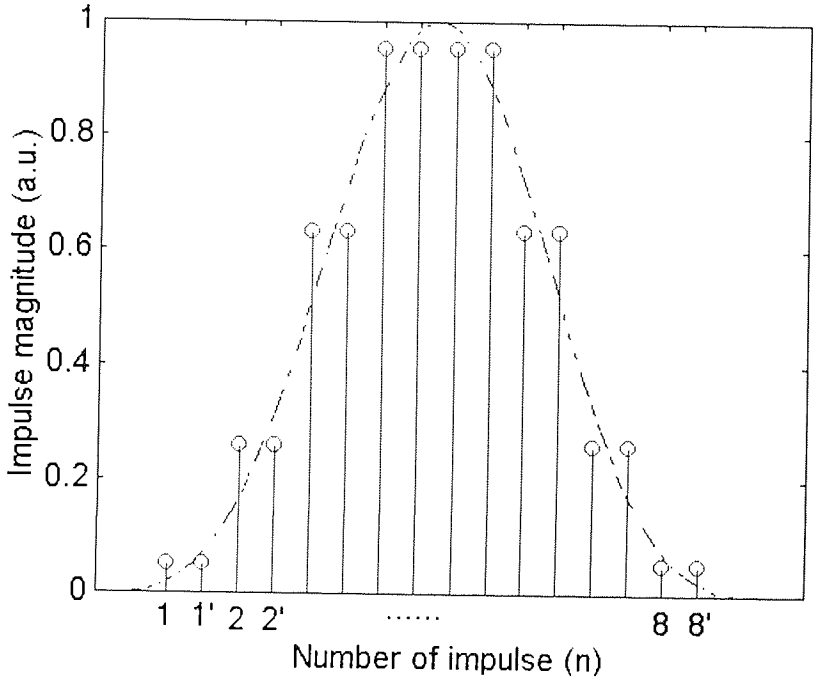

Figure 4-25. Tap-multiplexing by inserting the delayed taps.

This kind of misfit will lead to reduced extinction ratio of the filter frequency response. It is also estimated that the degree of degradation varies with different apodisation shapes. In explaining this, a Bartlett window and a Blackman window were used. Bartlett window corresponding to an pulse intensity 'slow-varying' apodisation profile. It is estimated that the frequency response of this kind of filter will have less degradation. Figure 4-26 shows the frequency response of the filters using Bartlett apodisation profile. We can see 5-dB degradation of extinction ratio from unmultiplexed 26.5 dB to multiplexed 21.5 dB. While for Blackman window profile, as in Figure 4-27, the unmultiplexed filter has a 65-dB extinction ratio. A multiplexed filter has an extinction ratio of only 19dB, leading to a degradation of 46 dB. We have less extinction ratio when we use 'slow-varying' apodisation profile. However, a

better extinction is achieved when we use insertion-multiplexing method since the multiplexed pulse fits better than the 'fast-varying' profile. It is obvious that this 'pulse insertion' method applies to the 'slow-varying apodisation profile.

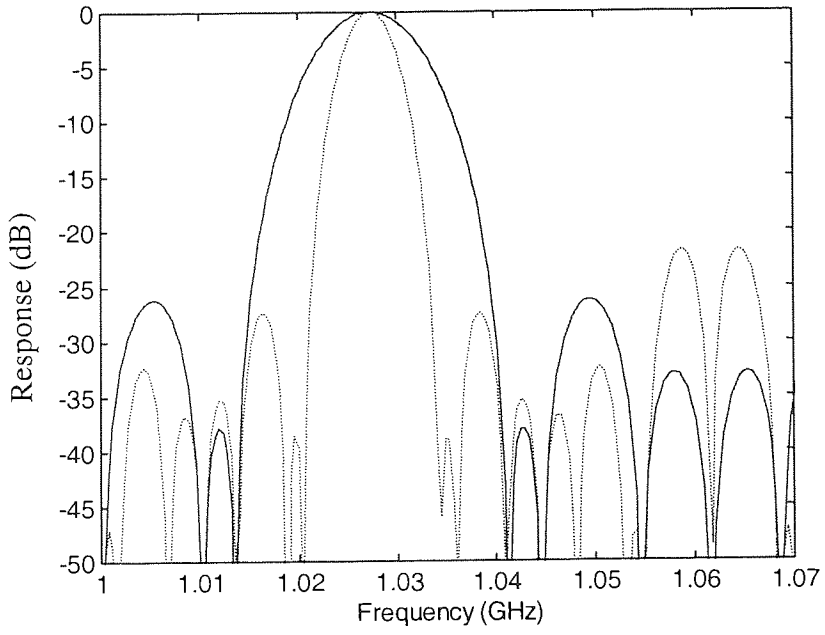

Figure 4-26. Filter frequency response when a Bartlett window was used. (Solid lines: filter having eight gratings, Dotted line: filter using insertion multiplexing method).

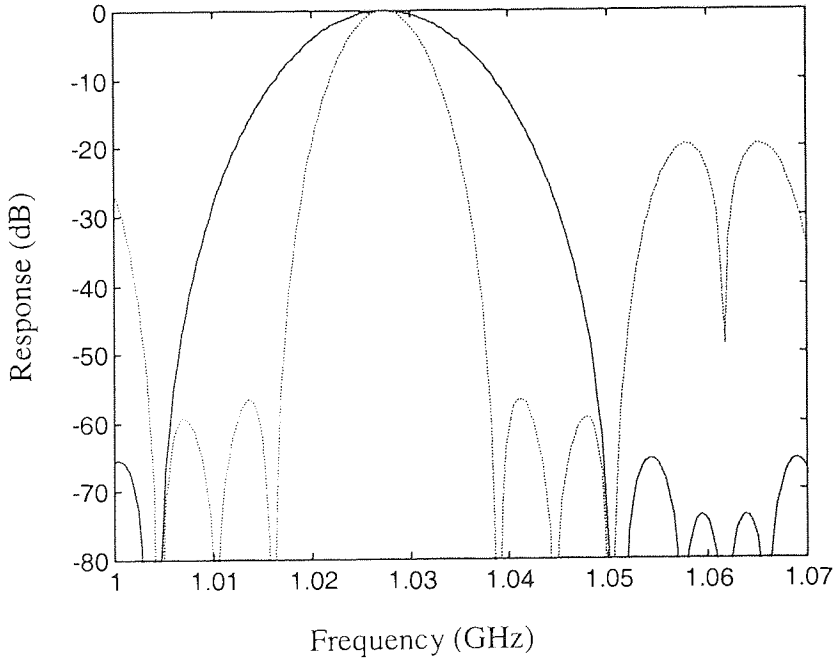

Figure 4-27. . Filter frequency response when a Blackman window was used. (Solid lines: filter having eight gratings, Dotted line: filter using insertion multiplexing method).

4.7 Suppressed Carrier Effect

Since FBG is a dispersive device, microwave photonic system employing FBG may suffer from suppressed carrier effect. That is, RF output may present degradation at certain frequency. Thus, it is obligatory that we know at the design stage what influence the FBG will bring about to this system. In the next few sections, we first introduce the suppressed carrier effect. Then we show in detail how to measure the FBG time delay response and present some simulation result of RF output when microwave photonic system using this grating. Last, we compare this result with measured RF output.

4.7.1 Introduction

An ideal amplitude modulated optical signal will have two sidebands of equal amplitude and opposite phase relative to the optical carrier. Bragg gratings can give rise to degradation in the received microwave signal amplitude by introducing changes in the relative amplitudes and phases of the sidebands. Provided the entire signal spectrum lies in the flat central reflectivity and time delay regions, the microwave signal at the receiver will suffer only a delay. If however parts of the signal lie outside this central region there will be a differential power loss across the spectrum, resulting in a degradation of the detected RF power at the optical receiver.

After reflection from a Bragg grating, the received electrical RF amplitude, generated by this optical signal can be expressed as:

$$A_{RF}(\omega) \propto (R_1 \cos\theta_1 + R_2 \cos\theta_2)\cos(\omega_m t)$$

Equation 4-6

where R_1, θ_1 and R_2, θ_2 are the reflectivity and phase shifts corresponding to the upper and lower sidebands at microwave frequency ω_m. Thus, from the measured reflectivity and group delay characteristics of the grating, we can calculate precisely the received RF amplitude as a function of optical carrier frequency and microwave RF frequency.

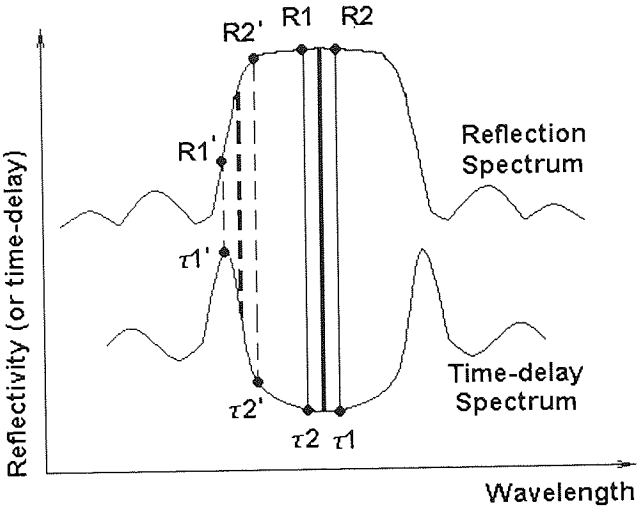

Figure 4-28. Diagram showing that modulated signal with optical carrier at centre of grating reflection and time-delay response (solid vertical lines) and that deviate from central of grating responses (broken vertical lines).

This is shown in Figure 4-28. The three vertical lines represent RF modulated signal with optical carrier at the centre of the grating's reflection and time-delay spectrum. The sidebands are equally placed. The cross points of the two sidebands with grating's reflection spectrum corresponding to R_1 and R_2 in Equation 4-6. The cross points on the time-delay spectrum correspond to τ_1 and τ_2. θ_1 and θ_2 in Equation 4-6 are derived from the multiplication of τ_1, τ_2 with modulation frequency ω_m. We can see from Figure 4-28 that the difference between τ_1' and τ_2' (optical carrier deviate from centre of grating time-delay spectrum) is much larger than that between τ_1 and τ_2 (optical carrier locate at centre of grating time-delay response). The conditions are the same in amplitude response. This, according to Equation 4-6, will result in degradation of received RF signal.

A simulation result can be seen in Figure 4-30. The grating used is a uniform grating. Its reflectivity and time delay response is shown in Figure 4-29. When the wavelength of optical carrier is placed at the centre of grating reflection spectrum (line I), the detected RF signal has relative flat response. If the optical signal shift to both side of central flat region of grating response (line II and III), the RF signal will suffer degradation at certain frequency.

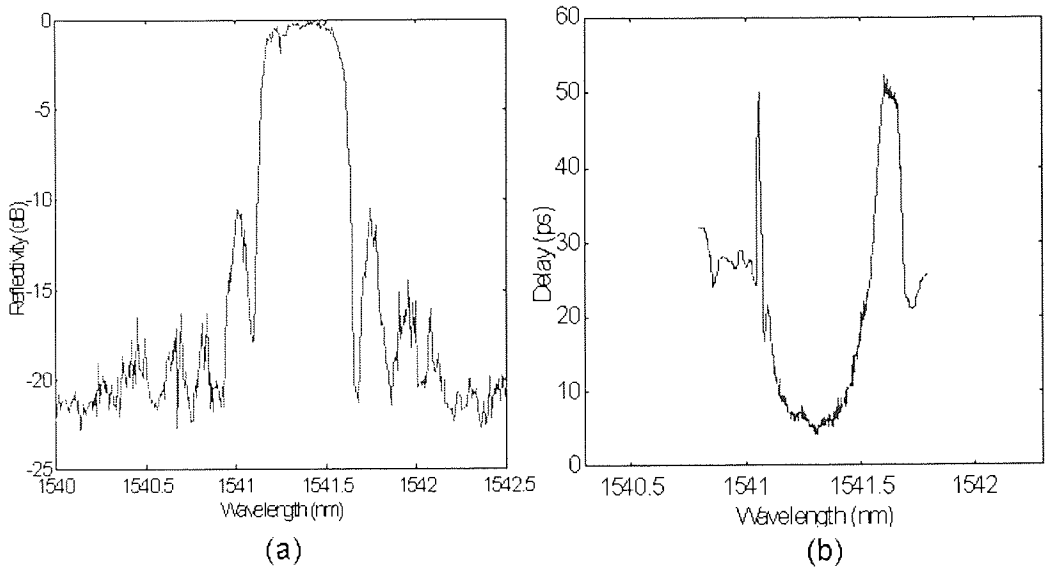

Figure 4-29. Measured reflectivity (a) and time delay response (b) of a uniform fibre Bragg grating.

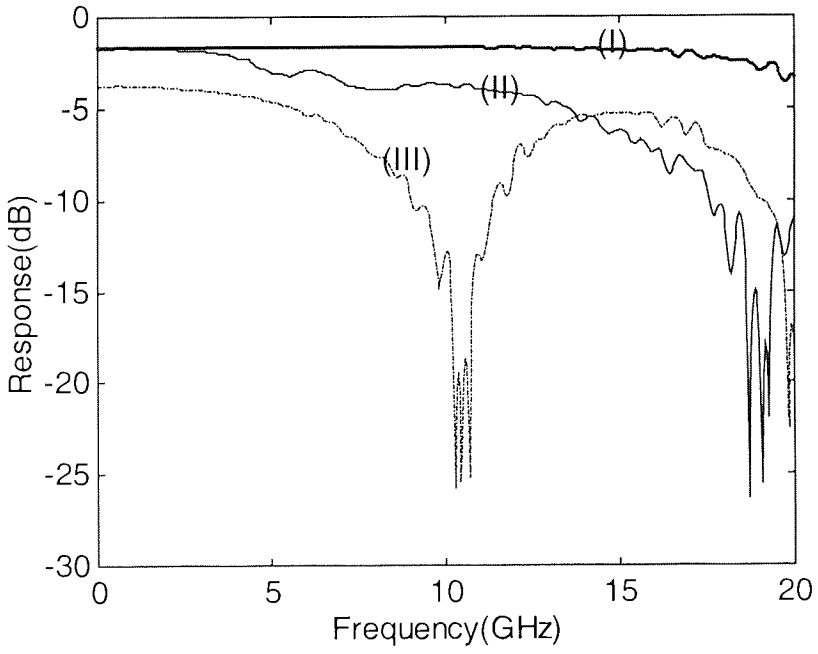

Figure 4-30. Simulation result of RF response when system employed uniform grating with reflection and time-delay response showed in Figure 4-29. (I) λ_c=1541.28 nm, (II) λ_c=1541.1 nm (III) λ_c=1541.7 nm.

4.7.2 Time-Delay Measurement

As we have said before, θ_1 and θ_2 in Equation 4-6 are derived from the multiplication of τ_1, τ_2 with modulation frequency ω_m. So it is necessary to measure grating time-delay response accurately. The set-up for grating time-delay measurement is shown in Figure 4-31. The tuneable laser provided optical carrier, which was modulated by an electro-optical modulator, built in the lightwave component analyser (LCA). The optical carrier together with two sidebands reached port 1 of an optical circulator. The grating was placed at port 2. The reflected signals were fed to LCA to analyse the response. It should be noted that the LCA doesn't work in a sweeping mode as before when we measured the transversal filter frequency response. The RF frequency should be fixed to provide constant modulation.

The grating's time-delay response is wavelength dependant. In this set-up, the measured result from LCA is phase vs. number of points swept. Time delay value can be worked out from $t=\theta/\omega$ if we know the modulation frequency ω. In order to obtain the wavelength information, the tuneable laser and LCA must be synchronised. Before scanning the tuneable laser, a start wavelength λ_1, end wavelength λ_2 and step $\Delta\lambda$ was inputted. The number of points scanned N could be calculated by $N=(\lambda_1-\lambda_2)/\Delta\lambda$. Then LCA was set to sweep using exactly the same number of points. The X-axis corresponded to the start and end wavelength.

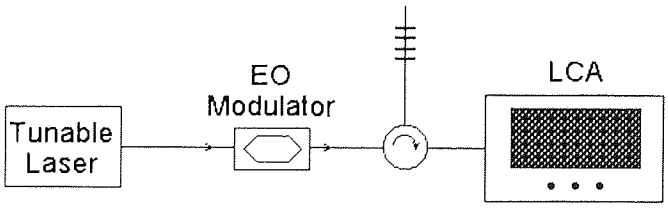

Figure 4-31. Experimental set-up of grating time delay measurement.

The RF modulation frequency should be carefully selected. At a low modulation frequency, the two sidebands are placed relatively close. When the optical carrier scanned the grating, better grating time-delay information can be derived. However, as the measure sensitivity is determined by ωt, where ω is the modulation frequency, t is grating time-delay, a poor sensitivity result in this

case. At a high modulation frequency, we have a better sensitivity from ωt. But the two sidebands are separated at a larger distance. Thus, some detailed grating time-delay information is omitted from averaging.

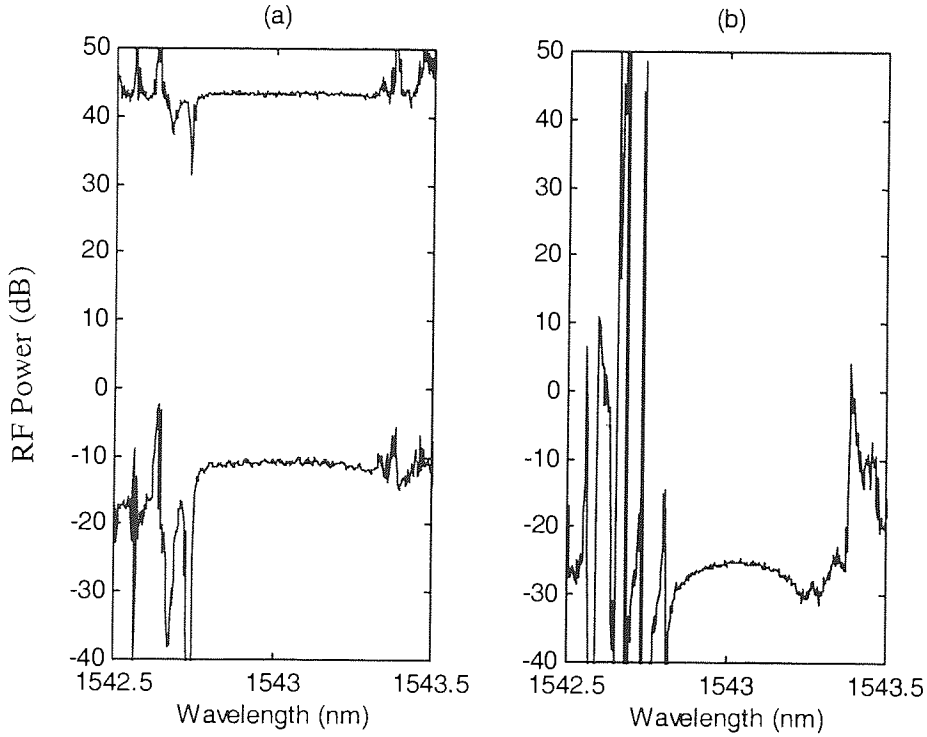

Figure 4-32. Measured results of a grating's time-delay response using different modulation frequency, upper trace in (a) (modulation frequency f=200MHz), lower trace in (a) (f=1GHz), (b) (f=10GHz)

As an example, in Figure 4-32, we used a modulation frequency of 200MHz (upper line in (a)), 1GHz (lower line in (a)) and 10GHz (b). Compared with that results measured with 1GHz, the upper trace in (a) doesn't have accurate details at left band edge. This is due to the poor sensitivity. The trace in (b) doesn't have enough resolution due to the large spacing of the two sidebands. Consideration should be paid with respect to the type of gratings to be measured. A simulation will help to estimate grating's bandwidth and the range of time-delay to be measured, so that a proper measure range can be selected.

4.7.3 RF Signal Degradation Measurement

The experimental set-up for RF signal degradation measurement is the same as shown in Figure 4-31. This time, the wavelength of the tuneable laser is

fixed. The LCA is set to measure frequency response with a sweeping frequency from 130MHz to 20GHz.

The microwave response calculated using Equation 4-6 is verified by comparing with the measured microwave amplitude spectral response at several different optical carrier wavelengths. The grating reflectivity spectra and group delay measurements, given in Figure 4-29, were used in Equation 4-6 to calculate the response for comparison. Both sets of results are plotted at different carrier wavelengths in Figure 4-33. As can be seen we have good agreement between the RF frequency responses calculated from the grating spectra and those directly measured.

Figure 4-33 (a) shows the results taken when the carrier wavelength is 1541.28 nm, in the centre of time delay response area. The two sidebands (± 0.16 nm at 20GHz modulation) are all well within the response region. Therefore, the received RF response is flat at frequencies up to 20 GHz. In Figure 4-33 (b) the carrier wavelength is tuned to 1541.18 nm. As the RF modulation frequency is increased, the upper sideband suffers an increasing delay relative to the carrier. At a frequency of 19GHz, this delay corresponds to a π phase shift and there is a null in the received RF spectrum. As the carrier wavelength is further decreased, the RF frequency at which this null occurs moves to lower frequencies and the RF bandwidth of the grating is reduced. For example, in Figure 4-33 (c), the carrier's wavelength is 1541.165nm. The null appeared at a RF modulation frequency of 16GHz. Similar results are achieved if the carrier wavelength is shifted to longer wavelengths where the opposite sideband suffers an increasing delay. Differences between the two sets of curves are due to environmental changes between their measurement.

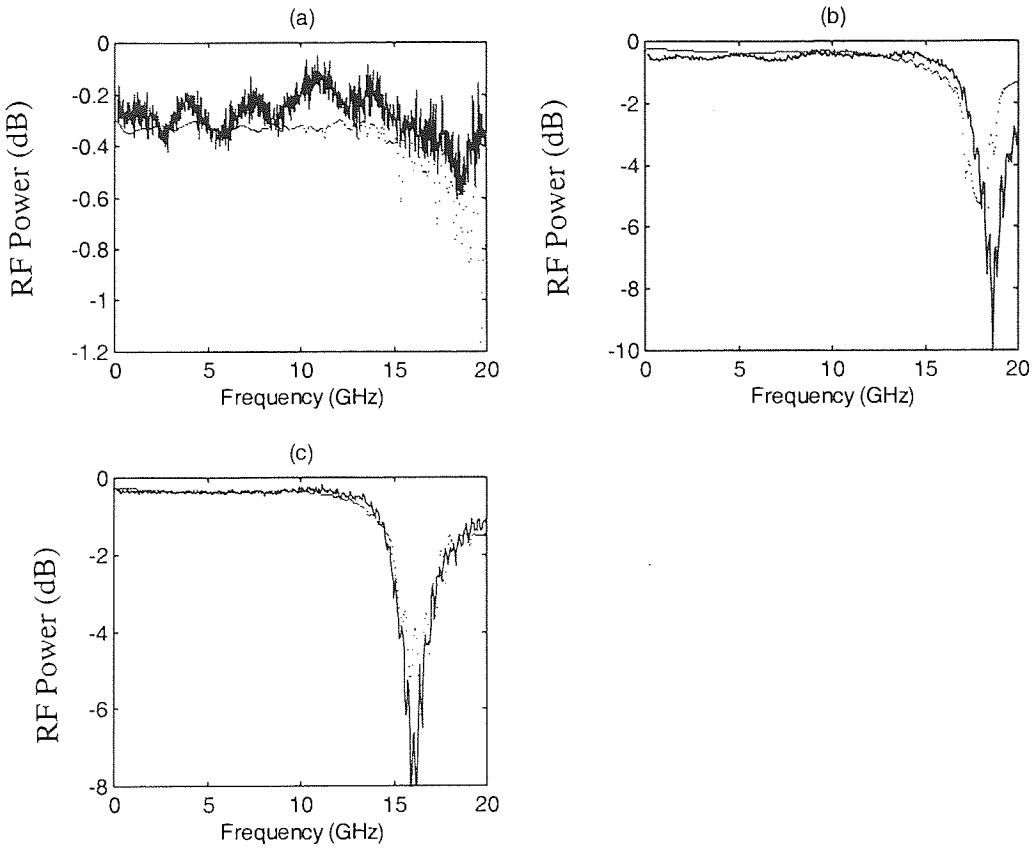

Figure 4-33. RF power against Microwave frequency. Solid lines are measured, dashed lines are calculated. (a) λ_c=1541.28 nm, (b) λ_c=1541.18 nm (c) λ_c=1541.165 nm.

The nulls achieved are only about 8dB deep and have oscillatory features on them. The depth of the nulls will depend on the relative strengths of the two sidebands when they are out of phase. If the two sidebands are of equal amplitude, they will entirely cancel out. In the results presented here, as a sideband approaches the edge of the grating spectrum, its amplitude is reduced and its delay increased. If the opposite sideband retains constant amplitude then the sidebands will only partially cancel out for a π phase change and the null depth will be reduced, as shown in Figure 4-33. Additionally, the group delay characteristic of the grating is not itself a smooth function, particularly at the edges of the grating spectrum. Hence the relative delay in the sidebands does not vary smoothly and the RF spectrum demonstrates some oscillation.

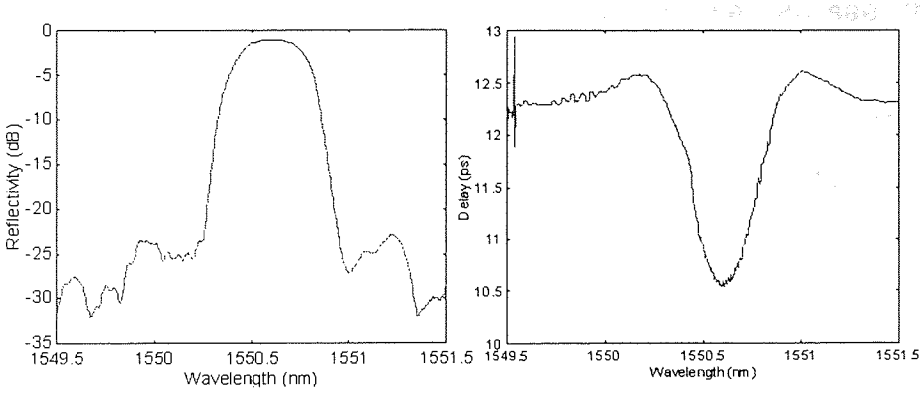

Figure 4-34. A measured reflectivity and time delay response of an apodised uniform Bragg grating.

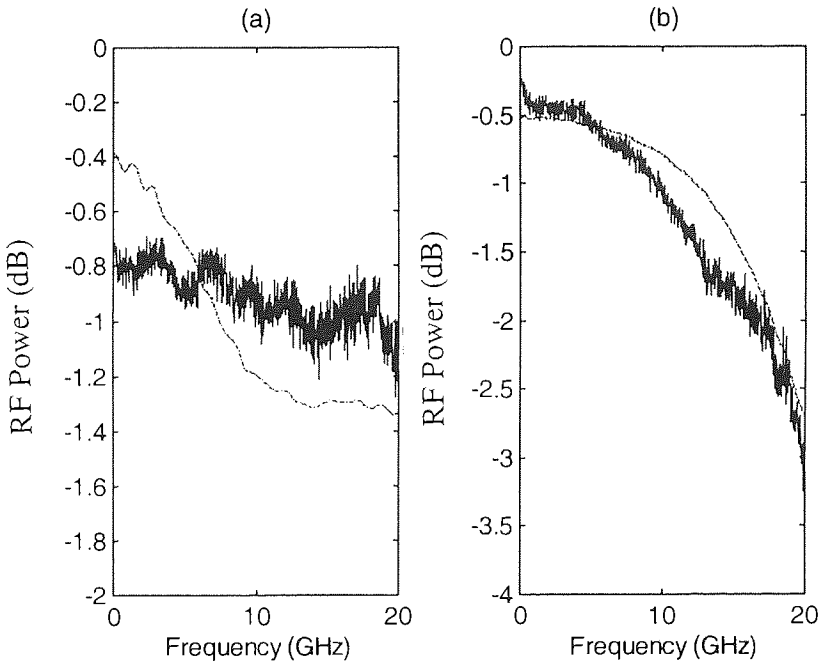

Figure 4-35. RF power against Microwave frequency. Solid lines are measured, dashed lines are calculated. (a) λ_c=1550.6 nm, (b) λ_c=1550.75 nm.

Uniform gratings exhibit large sidelobes in the reflection spectra and oscillations in the group delay response. These features are undesirable and can be significantly suppressed by a suitable apodisation of the modulation depth of the Bragg grating along its length. In Figure 4-34, we show the measured response for a 4.5-mm long grating with a raised cosine apodisation profile. The curves are much smoother and, compared with unapodised grating, the time delay between central wavelength and edge of the grating has been greatly reduced. The microwave responses calculated from this profile and

those directly measured are given in Figure 4-35. As we can see, they are much flatter than those of the unapodised grating are.

An important concern for the practical use of Bragg gratings in microwave photonic system is their sensitivity to temperature. The Bragg grating has temperature sensitivity of approximately 10^{-2} nm/K. For the apodised grating, reflecting a 20GHz microwave signal the bandwidth tolerated before there is a 3dB drop is signal is 0.29nm. Thus, the Bragg grating has a useable temperature range of 29K for a 3dB change in signal power at 20GHz. For unapodised grating used in this experiment, under the same circumstance (at modulation frequency of 20GHz, RF signal drop of 3dB), this bandwidth is 0.1nm, corresponding to a useable temperature range of 10K.

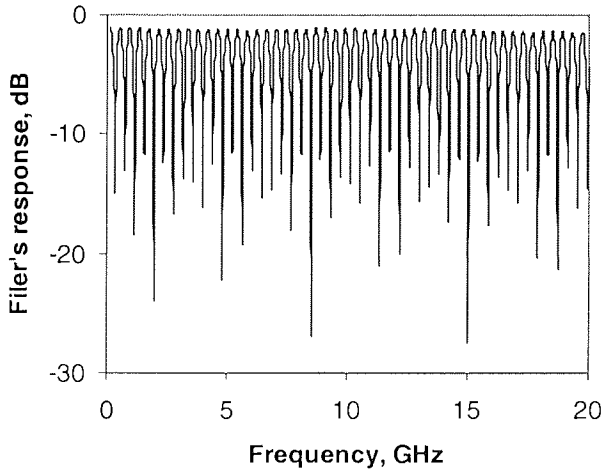

(a)

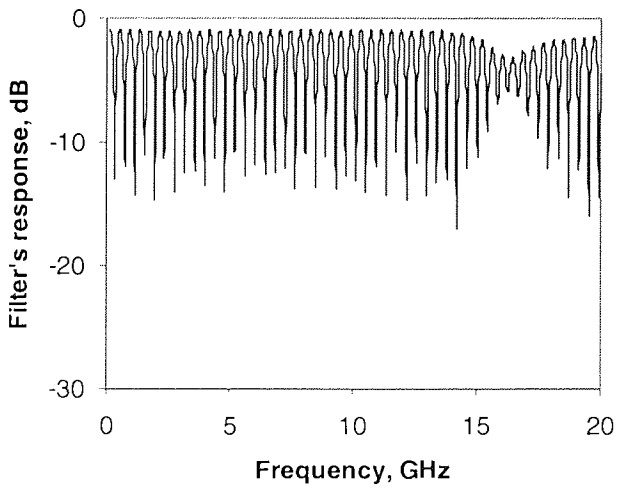

(b)

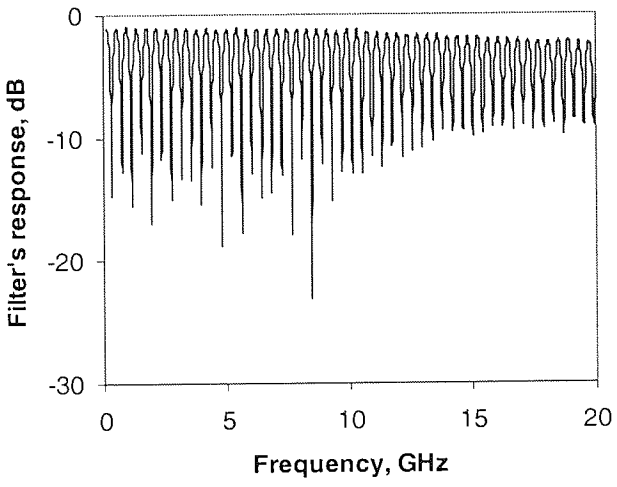

(c)

Figure 4-36. Measured frequency response of an optical fibre grating based notch filter. (a) with unapodised grating, λ_c=1541.28 nm, (b) with unapodised grating, λ_c=1541.18 nm, (c) with apodised grating, λ_c=1550.75 nm

This effect will certainly degrade the performance of a microwave photonic system employing such fibre gratings. If the unapodised fibre grating discussed above is used, the available bandwidth of the system may go down to 16 GHz. The measurement of the microwave response of an optical fibre grating based notch filter was implemented to show the effect of the fibre grating on the filter's frequency response. The measured spectra are shown in Figure 4-36 [[2]]. As can be seen, Figure 4-36 (a) shows a normal notch response with the bandwidth over 20 GHz where the unapodised grating was used and the carrier wavelength set at 1541.28 nm; however, a distorted response is shown in Figure 4-36 (b) where the carrier wavelength was tuned to 1541.165 nm. In Figure 4-36 (c), the apodised grating was used and the carrier wavelength was set as that in Figure 4-35(b). We can notice that, the amplitude and the visibility of the filter's response are slightly reduced as the microwave frequency increases and a nearly flat spectral response was obtained.

[2] Data provided by Dr. Wei Zhang

4.8 Chapter Conclusion

This chapter has worked on the FBG based transversal filter. Much effort has been given to the filter performance improvement. Detailed in this chapter was the first published work on high performance (35-dB extinction ratio) FBG array transversal filter. The use of FBG array instead of another design employing laser array provides the economical advantage. The achieved flexibility of apodisation, reconfiguration, and tuneability led to another step toward the practical use of this FBG based transversal filter in microwave photonic system. By the further improvement of high filter extinction ratio, factors limiting the filter extinction ratio has been studied.

Following this, filter reconfiguration and tuneability has been demonstrated. It has be noticed that very small filter FSR can be implemented because the low attenuation nature of optical fibre. This is another main advantage of FBG based transversal filter. Next, the work was moved onto improving filter frequency resolution. A simple tap multiplexing method was described. We can efficiently simply the filter fabrication process using this method when the filters have equal tap. Another solution was to insert these pulses trying to fulfil filter apodisation. However, it has limited improvement and we draw the conclusion that this method is applicable only when the filters are of equal tap.

Finally, another experiment was introduced to evaluate the RF power degradation effect for microwave photonic system using FBG. We draw the conclusion that for strong grating, the bandwidth of this system is limited by FBG. So great care must be applied when using FBG. It must be ensured that optical carrier located in the middle of the FBG's central flat region. Alternatively, the grating should be apodised to reduce the time delay variance between the central and edge of grating spectrum.

The work highlighted the fact that there are still some issues to be addressed for this FBG type transversal filter. First is the easy mass-producing of many taps without the sacrificing of tap apodisation function. Another issue is the fabrication of accurate delay line. For high performance filter, this delay line accuracy must be in micros. A probable solution is the post-treatment polish. The filter's FSR is limited by the optical source coherence length. For a large FSR, a very small-coherence-length source is needed.

5 THESIS CONCLUSION AND APPENDIX

5.1 Thesis Conclusion

The works discussed in this thesis were the applications of FBG in sensing and microwave photonics, in particular, the fabrication of the microwave photonic transversal filter. In the sensing application, a static strain sensor was first developed and it was transferred into a magnetic-field sensor using magnetostrictive transducer. In the microwave photonic applications, the first effort was to build a high performance transversal filter. Then a tap multiplexing technique was applied to improve its frequency resolution. Another relevant work was carried out to evaluate the RF power degradation effect when a FBG was employed in microwave photonic system. The highlighted advantages of each device and further work leading to improved performance have also been introduced.

The first conclusion drew from work on static strain sensor was that the minimum strain it can detect was 1με. This was limited by the environmental thermal drift. Moreover, the same comment was stated at other reports [158]. The intention of this work was utilising the high-resolution nature of interferometric interrogation technique, which was demonstrated in dynamic strain sensing. In addition, the Optical Path Difference (OPD) of this Mach-Zehnder can vary from -1.65nm to 2.65mm by stretching one arm that enables different sensitivity to this system. However, for static strain sensing, thermal perturbation proved to be a persistent problem during this experiment. A feedback device developed by Physics Department of Heriot-Watt University was employed to compensate for this thermal drift. Efforts have been given in several aspects including the changing of fibre length of PZT, varying proportional constant and integral constant on the feedback device to optimise its performance. Different types of gratings have also been used. It was

estimated that apodised grating should has a better resolution since it bring less noise to the system due to the suppression of sidelobes. However, the results showed no better resolution since this merit was covered by the thermal drift. The intention of using chirped grating was that a better-stabilised system might be derived due to the stronger light it reflected. However, this system needs a longer OPD, thus poor resolution results. We concluded that standard uniform grating will dominate the sensor application due to the relative simplicity of fabrication compared with other reported type of FBG sensors such as FBG fibre laser and phase shift FBG.

The work on FBG magnetic-field sensor was based on the static strain sensor developed in the previous experiment. The reported static and dynamic sensing resolution was the best result for FBG type magnetic-field sensor. The other advantages were the multiplexing potential and compact size. We have noticed that the magnetostrictive transducer 2605CO proved satisfying magnetic-mechanic conversion and it is suitable for both static and dynamic magnetic-field sensoring due to the high magnetostriction and good frequency response. The disadvantage for static magnetic-field sensing was the complexity of the system. Further consideration of this system lead to the replacement of the interrogation system with a scanned Fabry-Perot fibre filter, which can reach a 0.8 $\mu\varepsilon$ resolution and 50nm FSR. With the enhanced function of multiplexing, this kind of sensor can be used for distributed magnetic-field pollution detection or for risk warning such as in high-voltage area.

For the work on microwave photonics, the first published result on high performance transversal filter demonstrate the distinct advantage of FBG transversal filer over fibre optic transversal filter. It is one of the evidence that microwave photonics is coming closer to practical implementation. With a Hamming apodisation function, we acquired a best-of-the-time filter extinction ratio of 30dB. This has stimulated a further work of another Blackman apodisation applied which a 65dB filter extinction ratio should be derived. Instead, a 35dB extinction ration was achieved which was also a best-reported result although far from prediction. For reasoning this error, it was noticed that the pulse could not fit with the ideal apodisation profile all the time. It was first estimated that this pulse intensity variation was caused partly by optical carrier

partial coherence beat noise. In a further experiment, this prediction was proved in that the degree of pulse intensity variation dependant on the number of optical pulses existed in this system. In addition, this filter extinction degradation was, in part the result of unit-delay-line length uneven, which was unavoidable during filter fabrication. It was simulated that with the present fabrication method, this 35dB filter extinction ratio was the best we can achieve. Further work may be carried out to improve the delay-line fabrication and optical carrier partial coherence noise. A proposed plan for unit-delay-line fabrication was the post-polish treatment. Moreover, it was estimated that the pulse intensity variation would be alleviated if a short-coherence-length source was used. However, it was at the price of sacrificing system bandwidth resource.

Another effort was made to improve the filter frequency resolution. A tap-multiplexing scheme was proposed and demonstrated that it was very effective for equal tap filter. It was not only cost-effective but also minimising the delay-line fabrication error, which was demonstrated to be a crucial part for high performance filter. Soon, problem arose when we tried to apodised the filter because of the pulse-shifted nature of this method. An improved scheme was to design the delayed pulses to be inserted into the other pulses. Limited improvement has resulted. Then we reached the conclusion that this tap multiplexing method is not suitable for high performance filter design. The author has proposed the employing of intensity-inverse component, which can give inverse pulse intensity according to the input pulse. However, we haven't found the reports of these devices at that moment but it may be realised in the future.

The last experiment introduced was the evaluation of RF power degradation effect of microwave photonic system using FBG. The intention behind this work was to estimate the spectral location of RF power degradation due to the utilising of a FBG. With the knowledge of the FBG's reflection and time-delay response, the spectral location of RF power degradation can be forecasted. This helps the design of this kind of microwave photonic systems. We have got the result that an apodised grating can push this RF power degradation at a much higher frequency due to the minimised time delay variation at band edge. So our conclusion was that an apodised grating should be used in this

microwave photonic system to increase the system bandwidth. In addition, the gratings should be temperatures controlled because of the thermal-sensitive nature of FBG.

There are increasing research in many groups on the microwave photonic system. One report [159] showed that negative coefficient can be fulfilled using differential detection method, thus make it possible for arbitrary apodisation implementation. Other reports [160] presented a method of over-modulation of optical carrier and time sampling technique [161] to reduce optical carrier beat noise. With all the progress, we have the confidence that microwave photonic system will someday walk out of research laboratory into commercialised system.

Appendix A: Transfer Matrix Method

Coupled-mode theory (CMT) is extensively used for the analysis of fibre Bragg grating structure because of its simplicity and flexibility. The most important parameter is the coupling coefficient between the forward and the backward modes due to the presence of the index perturbation. However, in the case of calculating strong grating, the accuracy is questionable.

Transfer matrix method (TMM) is another powerful tool to the analysis of the grating structures. In this method, one can divide FBG into sections, which are considered homogeneous. If the fundamental matrices for each section are determined, the characteristics of this FBG can be derived by multiplying these fundamental matrices. This is shown in Figure A- 1.

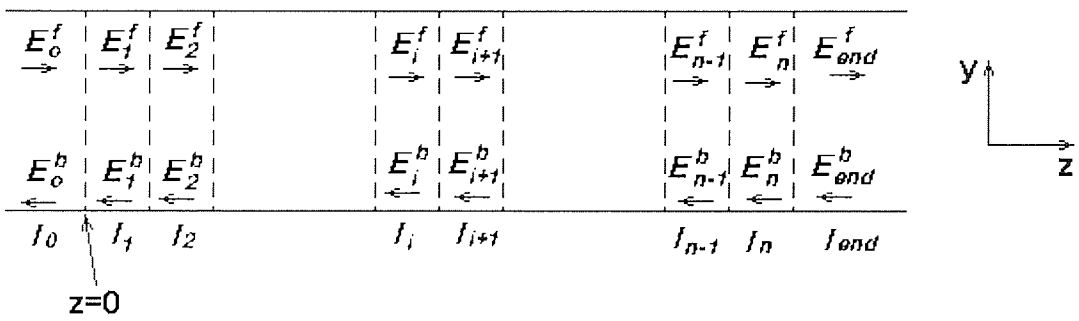

Figure A- 1. FBG in sectioned representation.

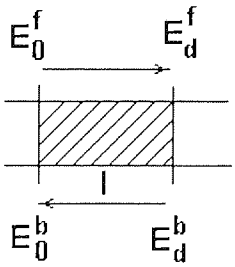

Figure A- 2. A single grating section.

Consider a single grating section shown in Figure A- 2, the amplitudes of forward and backward propagating waves, E^f and E^b are related through the following expression [162]:

$$\begin{pmatrix} E_0^f \\ E_0^b \end{pmatrix} = \begin{pmatrix} T_{11} & T_{12} \\ T_{21} & T_{22} \end{pmatrix} \begin{pmatrix} E_d^f \\ E_d^b \end{pmatrix}$$

Equation A- 1

$$T_{11} = \left[\cosh(\gamma l) + \frac{i\Delta\beta \sinh(\gamma l)}{\gamma l} \right] \exp\left(\frac{i2\pi l}{\lambda_B} \right)$$

Equation A- 2

$$T_{12} = \frac{-\kappa l \sinh(\gamma l) \exp\left(\frac{-i2\pi l}{\lambda_B} \right)}{\gamma l}$$

Equation A- 3

$$T_{21} = T_{12}^*$$
$$T_{22} = T_{11}^*$$

Equation A- 4

κ is the coupling coefficient of the grating. $\Delta\beta$ is the detuning form the Bragg condition, $\gamma^2 = \kappa^2 - \Delta\beta^2$.

The electric field across a boundary is related, so that we can determine the matrix relation across the entire structure by multiplying the relevant matrices together. Assuming that light is incident from only one side of grating, we can apply $E^f_{end}=0$. The following matrix relation can be achieved:

$$\begin{bmatrix} E_o^f \\ E_o^b \end{bmatrix} = T_o T_1 \cdots T_n \begin{bmatrix} E_{end}^f \\ 0 \end{bmatrix}$$

Equation A- 5

Where $T_0, T_1 \ldots T_n$ corresponding the fundamental matrices of each section. Since the incident electric fields E_0^f and E_0^b are expressed in terms of E_{end}^f we can calculate the complex reflection coefficient of a multiplayer structure

$$r = \frac{E_0^f}{E_0^b}$$

Equation A- 6

if we know the refractive index and absorption coefficient in each section. From these data, we can determine both the reflectivity and the phase change.

Appendix B: Simulating Program for Equal-Tap FBG Transversal Filter (Matlab Code)

The program list below can be used for the simulation of transversal filter frequency response when filter has equal tap.

```
function p=TF(f,dl)
%_____________________________________
%p=TF(f,dl)
%simualte the modulus fibre bragg
%grating photonic transversal
%filter
%f: frequency offset(should be vector)
%dl: incremental grating spacing
%_____________________________________
i1=exp(j*2*pi*f*3*1.46/3e8);
i2=exp(j*2*pi*f*(3+dl)*1.46/3e8);
i3=exp(j*2*pi*f*(3+2*dl)*1.46/3e8);
i4=exp(j*2*pi*f*(3+3*dl)*1.46/3e8);
i5=exp(j*2*pi*f*(3+4*dl)*1.46/3e8);
i6=exp(j*2*pi*f*(3+5*dl)*1.46/3e8);
i7=exp(j*2*pi*f*(3+6*dl)*1.46/3e8);
i8=exp(j*2*pi*f*(3+7*dl)*1.46/3e8);
i=abs(i1+i2+i3+i4+i5+i6+i7+i8);
P=i.^2;
p=10*log10(p);
```

Appendix C: Simulating Program for Blackman Apodised FBG Transversal Filter (Matlab Code)

The following program was used for the simulation of transversal filter frequency response when the filter using Blackman apodisation function.

```
function p=TFblackman(f,dl)
%_____________________________________
%p=TFblackman(f,dl)
%simualte the modulus fibre bragg
%grating photonic transversal
%filter using Blackman apodisation
%function
%f: frequency offset(should be vector)
%dl: incremental grating spacing
%_____________________________________
i1=exp(j*2*pi*f*3*1.46/3e8);
i2=exp(j*2*pi*f*(3+dl)*1.46/3e8);
i3=exp(j*2*pi*f*(3+2*dl)*1.46/3e8);
i4=exp(j*2*pi*f*(3+3*dl)*1.46/3e8);
i5=exp(j*2*pi*f*(3+4*dl)*1.46/3e8);
i6=exp(j*2*pi*f*(3+5*dl)*1.46/3e8);
i7=exp(j*2*pi*f*(3+6*dl)*1.46/3e8);
i8=exp(j*2*pi*f*(3+7*dl)*1.46/3e8);
i=abs(0.051*i1+0.258*i2+0.63*i3+0.9511*i4+0.9511*i5+0.63*i6+0.258*i7+0.051*i8);

p=20*log10(i);
```

PUBLICATIONS

1. G. Yu, J. A. R. Williams, W. Zhang, L. Zhang and I. Bennion, "Bragg grating based magnetic-field sensor," Proc. Of Conference PREP'99, Manchester, UK, pp.179-185, 1999.

2. G. Yu, W. Zhang, J. A. R. Williams, "Evaluation of RF power degradation in microwave photonic systems employing uniform fibre Bragg gratings," Opt. Commun., vol. 177, pp. 271-275, 2000.

3. G. Yu, W. Zhang, J. A. R. Williams, "Synthesis of optical transversal filter with tap multiplexing," Proc. Microwave Photonics(MWP) 2000, Oxford, UK, pp. 214-216, 2000.

4. G. Yu, W. Zhang, J. A. R. Williams, "Synthesis of microwave transversal filter with in-fibre Bragg grating array," Proc. Appl. Opt. Opto-electron. Conference, Loughborough, UK, pp.23-24, 2000.

5. W. Zhang, G. Yu, J. A. R. Williams, "Tap multiplexed fibre grating-based optical transversal filter," Electron. Lett., vol. 36, pp.1708-1710, 2000.

6. G. Yu, W. Zhang, J. A. R. Williams, "High-performance microwave transversal filter using fibre Bragg grating arrays," IEEE Photon. Technol. Lett., vol. 12, pp. 1183-1185, 2000.

REFERENCES

1 "Fiber Optics for illumination," Stockeryale product catalogue.

2 A. D. Kersey, M. A. Davis, H. J. Patrick, M. LeBlanc, K. P. Koo, C. G. Askins, M. A. Putnam and E. J. Friebele, "Fiber grating sensors," ' *J. Lightwave Tech.*, vol. 15, pp 1442-1463, 1997.

3 C. R. Giles, 'Lightwave applications of fiber Bragg gratings,' *J. Lightwave Tech.*, vol. 15, pp 1391-1404, 1997.

4 G. Meltz, W. W. Morey and W. H. Glenn, 'Formation of Bragg gratings in optical fibers by a transverse holographic method,' ", *Opt. Lett.*, vol. 14, pp. 823-825, 1989.

5 F. Ouellette, 'Dispersion cancellation using linearly chirped Bragg grating filters in optical waveguides,' *Opt. Lett.*, vol. 12, pp. 847-849, 1987.

6 H. Singh, M. Zippen, "Apodized fiber Bragg gratings for DWDM applications using uniform phase mask," 24th European conference on optical communication, vol. 1, pp.189-190, 1998.

7 F. Bilodeau, D. C. Johnson, S. Theriault, B. Malo, J. Albert, and K. O. Hill, "An all-fibre dense wavelength-division multiplxer/demultiplexer using photoimprinted Bragg gratings," *IEEE Photon. Technol. Lett.*, vol. 7, pp 388-390, 1995.

8 C. R. Giles, "Lightwave applications of fiber Bragg gratings," *J. Lightwave Tech.*, vol. 15, pp 1391-1404, 1997.

9 F. Bilodeau, D. C. Johnson, S. Theriault, B. Malo, J. Albert, and K. O. Hill, "An all-fibre dense wavelength-division multiplxer/demultiplexer using photoimprinted Bragg gratings," *IEEE Photon. Technol. Lett.*, vol. 7, pp 388-390, 1995.

10 F. Bakhti, P. Sansonetti, C. Sinet, L. Gasca, L. Martineau, S. Lacroix, X. Daxhelet and F. Gonthier, "Optical add/drop multiplexer based on UV-written Bragg grating in a fused 100% coupler," *Electron. Lett.*, vol. 33, pp. 803-804, 1997.

11 Y. Ito, Y. Ebine, "Radio on fiber system for triple band transmission in cellular mobile communication," *PROC. MWP 2000,* pp. 35-38, Oxford.

12 P. J. Matthews and P. D. Biernacki, "Recent progress in dispersion-based photonic beamforming," ," *PROC. MWP 2000,* pp. 1-4, Oxford.

13 S. Iezekiel and N. Bourhill, "Optical control of millimetre-wave p-HEMTs with applications to fibre radio," *PROC. MWP 2000,* pp. 55-58, Oxford.

14 T. Nagatsuma, A. Hirata, Y. Royter, M. Shinagawa, T. Furuta, T. Ishibashi and H. Ito, "A 120-GHz integrated photonic transmitter," *PROC. MWP 2000,* pp. 1-4, Oxford.

15 G. Yu, W. Zhang, J. A. R. Williams, "Synthesis of microwave transversal filter with in-fibre Bragg grating array," *Proc. Appl. Opt. Opto-electron. Conference*, Loughborough, UK, pp.23-24, 2000.

16 D. B. Hunter, R. A. Minasian, "Photonic signal processing of microwave signals using an active-fiber Bragg-grating-pair structure," *IEEE Trans. Microwave Theory Tech.*, vol. 45, no. 8, pp 1463-1466, 1997.

17 J. Capmany, D. Pastor and B. Ortega, "New and flexible fiber-optic delay-line filters using chirped Bragg gratings and laser arrays," *IEEE Trans. Microwave Theory Tech.*, vol. 47, no. 7, pp 1321-1326, 1999.

18 W. Zhang, G. Yu, J. A. R. Williams, "Tap multiplexed fibre grating-based optical transversal filter," *Electron. Lett.*, vol. 36, pp.1708-1710, 2000.

19 H. Kogelnik, "Coupled wave theory for thick hologram gratings", *Bell. Syst. Techn. J.*, vol 48, pp 2904-2947, 1969.

20 A. Yariv, "Coupled-mode theory for guided-wave optics", *IEEE J. Quantum. Electron.*, vol QE-9, pp 919-933, 1973.

21 T. Erdogan, 'Fiber Grating Spectra,' *J. Lightwave Tech.*, vol. 15, pp 1277-1294, 1997.

22 Bennion, J.A.R. Williams, L. Zhang, K. Sugden and N.J. Doran "UV- written in-fibre Bragg gratings", *Optical and Quantum Electronics*, vol. 28, pp 93-135, 1996.

23 J. Hong, Weiping Huang and T. Makino, "On the transfer matrix method for distributed-feedback waveguide devices" *J. Lightwave Technol.* Vol. 10, pp. 1860-1868, 1992.

24 M. Yamada, and K. Sakuda, "Analysis of almost-periodic distriburted feedback slab waveguides via a fundamental approach," *Appl. Opt.*, vol. 26, pp. 2167-2169, 1994.

25 D. P. Hang and P. S. J. Russell, "Photoinduced refractive-index changes in germanosilicate fibres," *Opt. Lett.*, vol. 15, pp. 102-104, 1990.

26 R. M. Atkins, V. Mizrahi and T. Erdogan, "248 nm induced vacuum UV spectral changes in optical fibre preform cores: Support for a colour centre model of photosensitivity," *Electron. Lett.*, vol. 29, pp. 385-387, 1993.

27 L. Dong, J. L. Archambault, L. Reekie, P. S. J. Russel and D. N. Payne, "Photoinduced absorption change in germanosilicate preforms: Evidence for the colour-centre model of photosensitivity," *Appl. Opt.*, vol. 34, pp. 3436-3440, 1995.

28 B. Poumellec, P. Guenot, I. Riant, P. Sansonetti, P. Niay, P. Bernage and J. F. Bayon, "UV induced densification during Bragg grating inscription in Ge:SiO_2 preforms," *Opt. Mater.*, vol. 4, pp. 441-449, 1995.

29 B. Poumellec, I. Riant, P. Niay, P. Bernage and J. F. Bayon, "UV induced densification during Bragg grating inscription in Ge: SiO_2 preforms: interferometric microscopy investigations," *Opt. Mater.*, vol. 4, pp. 404-409, 1995.

30 B. Poumellec, P. Niay, M. Douay and J. F. Bayon, "The UV induced refractive index grating in Ge: SiO_2 preforms: Additional cw experiments and the macroscopic origin of the change in index," *J. Phys. D: Appl. Phys.*, vol. 29, pp. 1842-1856, 1996.

31 M. Douay, W. X. Xie, T. Taunay, P. Bernage, P. Niay, P. Cordier, B. Poumellec, L. Dong, J. F. Bayon, H. Poignant and E. Delevaque, "Densification involved in the UV-based photosensitivity of silica glasses and optical fibres," *J. Lightwave Technol.* , Vol. 15, pp. 1329-1342, 1997.

32 J. Albert, B. Malo, K. O. Hill, F. Bilodeau, D. C. Johnson and S. Theriault, "Comparson of one-photon and two-photon effects in the photosensitivity of germanium-doped silica optical fibers exposed to intense ArF excimer laser pulses," *Appl. Phys. Lett.*, vol. 67, pp. 3529-3531, 1995.

33 H. Poignant, J. F. Bayon, E. Delevaque, M. Monerie, P. Niay, P. Bernage and M. Duay, "Influence of the H_2 loading on the kinetics of type II A fibre Bragg grating photoinscription," *IEEE Colloquium Optical Fibre Gratings, London, England, Feb. 1997.*

34 T. Taunay, P. Niay, P. Bernage, M. Douay, W. X. Xie, D. Pureur, P. Cordier, J. F. Bayon, H. Poignant, E. Delevaque and B. Poumellec, "Bragg grating inscriptions within strained monomode high NA germania doped fibres: Part I-Experimentation," *J. phys. D: Appl. Phys.*, Sept. 1996.

35 P. Niay, P. Bernage, S. Legoubin, M. Douay, W. X. Xie, J. F. Bayon, T. Georges, M. Monerie and B. Poumellec, "Behavior of spectral transmissions of Bragg gratings written in germania0doped fibers: Writing and erasing experiments using pulsed a cw UV exposure," *Opt. Commun.*, vol. 113, pp. 176-192, 1994.

36 D. L. Williams, B. J. Ainslie, J. R. Armitage, R. Kashyap and R. J. Campbell, "Enhanced UV photosensitivity in boron codoped germanosilicate fibres," *Electron. Lett.*, vol. 29, pp. 1191-1193, 1993.

37 A. Tomita and P. J. Lemaire, *Electron. Lett.*, vol. 21, pp. 71-73, 1985.

38 F. Ouellette, K. O. Hill and D. C. Johnson, "Enhancement of second-harmonic generation in optical fibres by hydrogen heat treatment," *Appl. Phys. Lett.*, vol. 54, pp. 1086, 1989.

39 G. D. Maxwell, R. Kashyap and B. J. Ainslie, "UV written 1.5 μm reflection filters in singlemode planar silica guides," *Electron. Lett.*, vol. 28, pp. 2016-2018, 1992.

40 K. O. Hill, F. Bilodeau, B. Malo, J. Albert, D. C. Johnson, Y. Hibino, M. Abe and M. Kawachi, "Photosensitivity of optical fibre and silica on silica/silicon waveguides," *Opt. Lett.*, vol. 18, pp. 953, 1993.

41 P. J. Lemaire, R. M. Atkins, V. Mizrahi, and W. A. Reed, "High pressure H_2 loading as a technique for achieving ultrahigh UV photosensitivity and thermal sensitivity in GeO_2 doped optical fibers," *Electron. Lett.*, vol. 29, pp. 1191-1193, 1993.

42 S. Yoshida, S. Kuwano and K. Iwashita, "Gain-flattened EDFA with high Al concentration for multistage repeater WDM transmission systems," *Electron. Lett.*, vol. 31, pp. 1765-1767, 1995.

43 L. Dong, J. L. Cruz, L. Reekie, M. G. Xu and D. N, Payne, "Enhanced photosensitivity in tin-codoped germanosilicate fibers," *IEEE Photon. Tech. Lett.*, vol. 7, pp.1048-1050, 1995.

44 L. Dong, P. J. Wels, D. P. Hand and D. N. Payne, "UV-induced refractive index change in Ce^{3+}-doped fibres," *in Conference on Lasers and Electro-Optics, 1991 (Optical Society of America, Washington, DC, 1991) pp. 68-71*

45 K. O. Hill, B. Malo, F. Bilodeau, D. C. Johnson, T. F. Morse, A. Kilian, L. Reimhart and K. Oh, "photosensitivity in Eu^{2+}:Al_2O_3 –doped0core fibre: Preliminary results and application to mode converters," in *Tech. Dig. Optic. Fibre Conf. (OFC'1991),* OSA, 1991, PAPER PD3, pp. 14-17.

46 L. Dong, J. L. Archambault, E. Taylor, M. P. Roe, L. Reekie and P. S. J. Russell, "photosensitivity in tantalum-doped silica optical fibers," *J. Opt. Soc. Amer. B,* vol. 12, pp. 1747-1750, 1995.

47 E. M. Dianov, K. M. Golant, R. R. Khrapko, A. S. Kurkov, B. Leconte, M. Douay, P. Bernage and P. Niay, "Grating formation in a germanium free silicon oxynitride fibre," *Electron. Lett.*, vol. 33, pp. 236-238, 1997.

48 E. M. Dianov, K. M. Golant, R. R. Khrapko and A. L. Tomashuk, "Nitrogen doped silical core fibres: A new type of radiation resistant fibre," *Electron. Lett.*, vol. 31, pp. 1490-1491, 1995.

49 K. O. Hill, Y. Fujii, D. C. Johnson, and B. S. Kawasaki, "Photosensitivity in optical fibre waveguides: Application to reflection filter fabrication," *Appl. Phys. Lett.,* vol. 32, pp. 647-649, 1978.

50 G. Meltz, W.W. Morey and W.H. Glen, "Formation of Bragg gratings in optical fibres by a transverse holographic method," *Opt. Lett.,* vol. 14, pp 823-825, 1989.

51 K.O. Hill and G. Meltz "Fiber Bragg grating technology fundamentals and overview", *J. Lightwave Tech.*, vol. 15, pp 1263-1276, 1997.

52 K. O. Hill, B. Malo, F. Bilodeau, D. C. Johnson, and J. Albert, "Bragg gratings fabricated in monomode photosensitive optical fibre by UV exposure through a phase mask," *Appl. Phys. Lett.*, vol. 62, pp. 1035-1037, 1993.

53 D. Z. Anderson, V. Mizrahi, T. Erdogan, and A. E. White, "Production of in-fibre gratings using a diffractive optical element," *Electron. Lett.*, vol. 29, pp. 566-568, 1993.

54 J.D. Prohaska, E. Snitzer, S. Rishton and V. Boegli, "Magnification of mask-fabricated fibre Bragg gratings", *Electron. Lett.*, vol. 29, pp 1614-1615, 1993.

55 Q. Zhang, D.A. Brown, L. Reinhart, T.F. Morse, J.Q. Wang, G. Xiao, "Tuning Bragg wavelength by writing gratings on prestrained fibres", *IEEE Photon. Technol. Lett.*, vol. 6, pp 839-841, 1994.

56 A. Othonos and X. Lee, "Novel and improved methods of writing Bragg gratings with phase masks," *IEEE Photon. Technol. Lett.*, vol. 7, pp1183-118, 1995.

57 S. Thibault, J. Lauzon, J. F. Cliche, J. Martin, M. A. Duguay and M. Tetu, "Numerical analysis of the optimal length and profile of a linearly chirped fibre Bragg grating for dispersion compensation," *Opt. Lett.*, vol. 20, pp. 647-649, 1995.

58 K. O. Hill, F. Bilodeau, B. Malo, T. Kitagawa, S. Theriault, D. C. Johnson and J. Albert," *Opt. Lett.*, vol. 19, pp. 1314-1316, 1994.

59 K. O. Hill, S. Theriault, B. Malo, F. Bilodeau, T. Kitagawa, D. C. Johnson, J. Albert, K. Takiguchi, T. Kataoka and K. Hagimoto, "Chirped in-fibre Bragg grating dispersion compensators: Linearisation of dispersion characteristic and demonstration of dispersion compensation in 100km, 10Gbit/s optical fibre link", *Elec. Lett.* Vol. 30, no. 21, pp. 1755-1756, 1994.

60 R. Kashyap, A. Swanton and D. J. Armes, "Simple technique for apodising chirped and unchirped fibre Bragg gratings," *Elec. Lett.* Vol. 32, no. 13, pp. 1226-1228, 1996.

61 J. Albert, K. O. Hill, B. Malo, S. Theriault, F. Bilodeau, D. C. Johnson and L. E. Erickson, "Apodisation of the spectral response of fibre Bragg gratings using a phase mask with variable diffraction efficiency," *Elec. Lett.* Vol. 31, no. 3, pp. 222-223, 1995.

62 J. A. Bucaro, H. D. Dardy and E. Carome, "Fiber optic hydrophone," *J. Acoust. Soc. Amer.*, Vol. 62, pp. 1302-1304, 1997.

63 A. M. Smith, "Polarization and magnetooptic properties of single mode fiber," *Appl. Opt.*, Vol. 17, pp. 52-56, 1978.

64 Yariv A and Winsor H, "Proposal for detection of magnetostrictive perturbation of optical fibers," *Opt. Lett.*, Vol. 5, pp. 87-89, 1980.

65 A. Dandridge, A. B. Tveten, G. H. Sigel, Jr., E. J. West and T. G. Giallorenzi, "Optical fibre magnetic field sensor," *Electron. Lett.*, vol. 16, pp. 408-409, 1980.

66 K. Bohm, Pl Martin, K. Petermann, E. Weidel and R. Ulrich, "Low-drift fiber gyro using a superluminescent diode," ," *Electron. Lett.*, vol. 17, pp. 352-353, 1981.

67 J. N. Fields and J. H. Cole, "Fiber microbend acoustic sensor," *Appl. Opt.*, Vol. 19, pp. 3265-3267, 1980.

68 W. B. Spellman, Jr. and R. L. Gravel, "Moving fiber-optic hydrophone," *Opt. Lett.*, Vol. 5, pp. 30-31, 1980.

69 A. B. Tveten, A. Dandridge, C. M. Davis and T. G. Giallorenzi, "Fiber optic accelerometer," ," *Electron. Lett.*, vol. 16, pp. 854-855, 1980

70 G. Yu, J. A. R. Williams, W. Zhang, L. Zhang and I. Bennion, "Bragg grating based magnetic-field sensor," Proc. Of Conference PREP'99, Manchester, UK, pp.179-185, 1999.

71 W. Ecke, K. Usbeck, V. Hagemann, R. Mueller and R. Willsch, "Chemical Bragg grating sensor network basing on side-polish optical fiber", *SPIE*, Vol. 3555, pp. 457-466, 1998.

72 L. A. Ferreira, A. B. Lobo Ribeiro J. L. Santow and F. Farahi, "Simultaneous displacement and temperature sensing using a white light interrogated low finesse cavity in line with a fiber Bragg grating," *Smart Mater. Struct.* Vol. 7, pp. 189-198, 1998.

73 P. M. Cavaleiro, F. M. Araujo and A. B. Lobo Ribeiro, "Metal-coated fibre Bragg grating sensor for electric current metering," *Elec. Lett.* Vol. 34, no. 11, pp. 1133-1735, 1998.

74 'Fibre-optic grating strain indicator: FLS3500', Electrophotonics Co, Canada.

75 C. Miller, T. Li, F. B. Miller, K. A. Hsu, "Stable, accurate, highly multiplexed fibre Bragg grating interrogation system" Micron Optics Inc, USA, 1997.

76 G. A. Ball and W. W. Morey, "Compression-tuned single-frequency Bragg grating fiber laser," *Opt. Lett.*, vol. 19, pp. 1979-1981, 1994.

77 M. Bugaud, P. Ferdinand, S. Rougeault, V. Dewynter-Marty, P. Parneix and D. Lucas, " Health monitoring of composite plastic waterworks lock gates using in-fibre Bragg grating sensor," *Smart Mater. Struct.*, vol. 9, pp. 322-327, 2000.

78 K. Wood, T. Brown, R. Rogowski and B. Jensen, "Fibre-optic sensors for health monitoring of morphing airframes: 1. Bragg grating strain and temperature sensor" *Smart Mater. Struct.*, vol. 9, pp. 163-169, 2000.

79 Y. J. Rao, D. J. Webb, D. A. Jackson, L. Zhang, and I. Bennion, "In-fibre Bragg-grating temperature sensor system for medical applications", *J. Lightwave Tech.*, vol. 15, pp 779-785, 1997.

80 T. A. Berkoff and A. D. Kersey, "Fibre Bragg grating array sensor system using a bandpass wavelength division multiplexer and interferometric detection," *Photon. Technol. Lett.*, vol. 8, pp 1522, 1996.

81 T. A. Berkoff *et al*, "Hybrid time and wavelength division multiplexed fibre grating array," in *Porc. SPIE*, vol. SPIE-2444, pp. 288, 1995.

82 A. B. L. Ribeiro, Y. J. Rao, L. Zhang, I. Bennion and D. A. Jackson, "A combined spatial- and time-division-multiplexing tree topology for fibre grating sensor systems," *Appl. Opt.*, vol. 35, pp. 2267-2273, 1996.

83 G. A. Ball W. W. Morey and P. K. Cheo, "fibre laser source/analyzer for Bragg grating sensor array interrogation," *J. Lightwave Tech.*, vol. 12, pp 700-703, 1994.

84 R. M. Measures, A. T. Alavie, R. Maaskant, M. Ohn, S. Karr, S. Huang, "Bragg grating structural sensing system for bridge monitoring," *Proc. SPIE*, vol. 2294, pp. 53-60.

85 Y. Ogawa, J. I. Iwasaki, K. Fnakamura, "Multiplexing load monitoring system of power transmission lines using fibre Bragg grating," *Proc. Of the 12th International Conference on Optical Fibre Sensors,* Williamsbrug, USA, pp. 468-471, 1997.

86 N. Takahashi, K. Yoshimura, S. Takahashi and K. Imamura, "Development of an optical fibre hydrophone with fibre Brag grating," *Ultrasonics,* Vol. 38, pp. 581-585, 2000.

87 V. V. Spirin, M. G. Shlyagin, S. V. Miridonov, F. J. Mendieta Jimenez, R. M. Lopez Gutierrez, "Fibre Bragg grating sensor for petroleum hydrocarbon leak detection," *Opt. Lasers Eng.*, vol. 32, pp. 497-503, 2000.

88 M. Pacheco, F. Mendoza Santoyo, A. Mendez and L. A. Zenteno, "Piezoelectric-modulated optical fibre Bragg grating high-voltage sensor," *Meas. Sci. Technol.*, vol. 10, pp. 777-782, 1999.

89 M. E. Jones, "Optical fibre grating-based strain and corrosion sensors," *Proc. SPIE.*, vol. 2948, pp. 94-100, 1996.

90 J. A. Greene, M. E. Jones, P. G. Duncan, C. L. Kozikowski, T. A. Bailey, R. G. May, and K. A. Murphy," *Proc. SPIE.*, vol. 3024, pp. 260-266, 1997.

91 Y. L. Lo and F. Y. Xiao, "Measurement of corrosion and temperature using a single-pitch Bragg grating fibre sensor," *J. Intelligent Mater. System Struct.*, vol. 9, pp. 800-807, 1998.

92 S. M. Melle, K. Liu and R. M. Measures, "A passive wavelength demodulation system for guided-wave Bragg grating sensors" *Photon. Technol. Lett.*, vol. 4, pp 616-518, 1992.

93 A. D. Kersey, T. A. Berkoff and W. W. Morey, "High-resolution fibre grating based strain sensor with interferometric wavelength-shift detection", *Electron. Lett.*, vol. 28, pp. 236-238, 1992.

94 G. Brady, K. Kalli, D. J. Webb and D. A. Jackson L. Reekie and J. L. Archambault, "Simultaneous interrogation of interferometric and Bragg grating sensors", *Opt. Lett.*, vol. 20, pp. 1340-1342, 1995.

95 L. N. Binh, N. Q. Ngo and S. F. Luk, "Graphical representation and analysis of the Z-shaped double-coupler optical resonator,"*J. Lightwave Tech.*, vol. 11, no. 11, pp 1782-1792, 1993.

96 S. Tedjini, A. Ho-Quoc, and D. A. M. Khalil, "All-optical networks as microwave and millimeter-wave circuits," *IEEE Trans. Microwave Theory Tech.*, vol. 43, no. 9, pp. 2428-2434, 1995.

97 W. Zhang, J. A. R. Williams, I. Bennion, "Recirculating fibre-optic notch filter employing fibre grating," *IEEE Photon. Technol. Lett.*, vol. 11, pp 836-838, 1999.

98 G. Yu, W. Zhang and J. A. R. Williams, "High Performance Microwave Transversal Filter using Fiber Bragg Grating Arrays,"

99 D. B. Hunter, R. A. Minasian and P. A. Krug, "Tuneable optical transversal filter based on chirped gratings," *Electron. Lett.*, vol. 31, pp. 2205-2206, 1995.

100 J. Capmany, D. Pastor, and B. Ortega, "New and flexible fibre-optic delay-line filters using chirped Bragg gratings and laser arrays," *IEEE Trans. Microwave Theory Tech.*, vol. 47, pp. 1321-1326, 1999.

101 V. Polo, F. Ramos, J. Marti, D. Moodie, and D. Wake, "Synthesis of photonic microwave filters based on external optical modulators and wide-band chirped fibre gratings," *J. Lightwave Technol.*, vol. 18, pp. 213-220, 2000.

102 W. W. Morey, G. Meltz, W. H. Glenn, "Fibre optic Bragg grating sensors," *PROC SPIE*, vol. 1169, pp. 98-107, 1989.

103 A. D. Kersey, T. A. Berkoff and W. W. Morey, "High-resolution fibre grating based strain sensor with interferometric wavelength-shift detection," *Electron. Lett.*, vol. 28, pp. 236-238, 1992.

104 A. D. Kersey, "Interrogation and multiplexing techniques for fibre Bragg grating strain-sensors," *PROC SPIE*, vol. 2071, pp. 30-48, 1993.

105 A. D. Kersey, M. A. Davis, H. J. Patrick, M. LeBlanc, K. P. Koo, C. G. Askins, M. A. Putnam, and E. J. Friebele, "Fiber grating sensors," *J. Lightwave Tech.*, vol. 15, pp 1442-1463, 1997.

106 Y. J. Rao, "Recent progress in applications of in-fibre Bragg grating sensors," *Optics and Lasers in Engineering*, vol. 31, pp. 297-324, 1999.

107 M. Bugaud, P. Ferdinand, S. Rougeault, V. Dewynter-Marty, P. Parneix and D. Lucas, "Health monitoring of composite plastic waterworks lock gates using in-fibre Bragg grating sensors," *Smart Mater. Struct.*, vol. 9, pp. 322-327, 2000.

108 M. A. Davis, A. D. Kersey, J. Sirkis and E. J. Friebele, "Shape and vibration mode sensing using a fibre-optic Bragg grating array," *Meas. Sci. Technol.*, vol. 7, pp. 759-765, 1996.

109 N. Takahashi, K. Yoshimura, S. Takahashi and K. Imamura, "Development of an optical fibre hydrophone with fibre Bragg grating," *Ultrasonics,* vol. 38, pp. 581-585, 2000.

110 M. G. Xu, H. Geiger, J. P. Dakin, "Optical in-fibre grating high pressure sensor," *Electron. Lett.*, vol. 29, pp. 398-399, 1993.

111 T. A. Berkoff, A. D. Kersey, "Experimental demonstration of a fibre Bragg grating accelerometer," *IEEE Photon. Tech. Lett.,* vol. 8, pp.1677-1679, 1996.

112 E. J. Friebele, C. G. Askins, A. B. Bosse, A. D. Kersey, H. J. Patrick, W. R. Pogue, M. A. Putnam, W. R. Simon, F. A. Tasker, W. S. Vincent and S. T. Vohra, "Optical fibre sensors for spacecraft applications," *Smart Mater. Struct.*, vol. 8, pp. 813-838, 1999.

113 A. D. Kersey, M. A. Davis, T. A. Berkoff, D.G. Bellemore K. P. Koo, R. T. Jones, "Progress towards the development of practival fibre Bragg grating instrumentation systmes," *Proc. SPIE*, vol. 2839, pp. 40-63, 1996.

114 W. L. Schulz, E. Udd, J. M. Seim, G. E. McGill, "Advanced fibre grating strain sensor systems for bridges, structures, and highways," *Proc. SPIE*, vol. 3325, pp. 212-221, 1998.

115 M. J. Caruso, T. Bratland, C. H. Smith and R. Schneider, "A new perspective on magnetic field sensing," *Techn. Articles,* Honeywell, SSEC, Nonvolatile Electronics, Inc. 2001.

116 Yariv A and Winsor H, "Proposal for detection of magnetostrictive perturbation of optical fibers," *Opt. Lett.*, Vol. 5, pp. 87-89, 1980.

117 A. Dandridge, A. B. Tveten, G. H. Sigel, Jr., E. J. West and T. G. Giallorenzi, "Optical fibre magnetic field sensor," *Electron. Lett.*, vol. 16, pp. 408-409, 1980.

118 C. J. Nielsen, "All fibre magnetometer with magnetic feedback compensation," *Proc. SPIE*, vol. 56, pp. 286-293, 1985.

119 D. Y. Kim, H. J. Kong, and B. Y. Kim, "Fibre-optic DC magnetic field sensor balanced detection technique," *IEEE Photon. Tech. Lett.*, vol. 4, pp.945-948, 1992.

120 Y. Ogawa, J.I. Iwasaki, K. Nakanura, " A multiplexing lad monitoring system of power transmission lines using fibre Bragg grating, " *Proc. Of the 12th International Conference on Optical Fibre sensors, Williamsburg, USA, 1997, pp. 468-471.*

121 T. E. Hammon, A. D. Stokes, "Optical fibre Bragg grating temperature sensor measurements in an electrical power transformer using a temperature compensated fibre Bragg grating as a reference," *Proc. Of the 11th International Conference on Optical Fibre Sensors,* Sapporo, Japan, pp. 566-569, 1996.

122 P. M. Cavaleiro, F. M. Araujo and A. B. Lobo Ribeiro, "Metal-coated fibre Bragg grating sensor for electric current metering," *Electron. Lett.*, vol. 34, pp. 1133-1135, 1998.

123 T. G. Giallorenzi, J. A. Bucaro, A. Dandridge, G. H. Sigel, Jr., J. G. Cole, S. C. Rashleigh, and R. G. Priest, "Optical fibre sensor technology," *IEEE J. Quantum Electron.*, vol. QE-18, pp. 626-665, 1982.

124 P. J. Henderson, N. E. Fisher, D. A. Jackson, "Current metering using fibre grating based interrogation of a conventional current transformer," *Proc. Of the 12th International Conference on Optical Fibre Sensors,* Williamsbrug, USA, pp. 186-189, 1997.

125 Y. J. Rao, P. J. Henderson, N. E. Fisher, D. A. Jackson, L. Zhang, I. Bennion, "Wavelength-division-multiplexed in-fibre Bragg grating Fabry-Perot sensor system for quasi-distributed current measurement," *Proc. Annual Conference on Appl. Opt. Optoelec. (IOP)*, Brighton, pp. 99-104, 1998.

126 E. Udd, "Fiber optic sensors, an introduction for Engineers and Scientists"

127 Wohlfarth E P, " Ferromagnetic materials, a handbook on the properties of magnetically ordered substances" Vol.2

128 Yariv A and Winsor H, "Proposal for detection of magnetostrictive perturbation of optical fibers," *Opt. Lett.*, Vol. 5, pp. 87-89, 1980.

129 P. J. Matthews and P. D. Biernacki, "Recent progress in dispersion-based photonic beamforming," *MWP 2000,* pp. 1-4, Oxford, Sept. 11, 2000.

130 H Ogawa, "Application of optical techniques to microwave signal processing (MSP)-Optical-microwave signal processing," *IEICE Trans. Electron.*, vol. E79-C, no. 1, pp.87-97, 1996.

131 S. Iezekiel and N. Bourhill, "Optical control of millimetre-wave p-HEMTs with applications to fibre radio," *PROC. MWP 2000,* pp. 55-58, Oxford.

132 H. F. Taylor, "Fibre and integrated optical devices for signal processing," *Proc. SPIE.*, vol. 176, pp.17-27, 1979.

133 H. F. Taylor, S. Gweon, S. P. Fang, and C. E. Lee, "Fibre optic delay-line for wideband signal processing", *SPIE*, vol. 1562, pp. 265275, 1991.

134 W. D. Jemison, P. R. Herczfeld, W. Rosen, A. Vieira, A. Rosen, A. Paolella, A. Joshi, ""*Microwave,* June 2000, pp. 44-51.

135 W. P. Mason, "multiple reflection ultrasonic delay lines", *Physical acoustics*, 1964, vol. 1, pp. 485.

136 G. D. Boyd, L. A. Coldren, and R. N. Thurston, "Acoustic waveguide with a cladded core geometry", *Appl. Phys. Lett.,*1975, vol. 26, pp. 31.

137 L. T. Claiborne, G. S. Kino, and E. Stern, Eds., "Special issue on surface acoustic waves", *proc. IEEE*, 1976, vol. 64.

138 C. C. W. Ruppel and T. A. Fjeldly, "Advances in surface acoustic wave technology, systems and applications-2," *International J. of High Speed Electronics and Systems*, Vol. 10, No. 3, (2000), PP. 553-602.

139 C. T. Chang, J. A. Cassaboom, H. F. Taylor, "fibre-optic delay-line devices for R. F. Signal processing," *Electron. Lett.*, vol. 13, pp. 678-680, 1977.

140 K. Wilner and A. P. Van Den Heuvel, "fibre-optic delay-lines for microwave signal processing," *Proc.IEEE*, vol. 64, pp. 805-807, 1976.

141 R. L. Ohlhaber and K. Wilner, "Fibre-optic delay lines for pulse coding", *Electro-optical Syst. Des.*, 1977, vol. 9, pp. 33.

142 C. T. Chang, J. A. Cassaboom, and H. F. Taylor, "fibre-optic delay-line devices for R.F. signal processing", *Electron. Lett.*, 1977, vol. 13, pp. 678.

143 H. F. Taylor, "Fibre and integrated optical devices for signal processing", *Proc. SPIE*, 1979, vol. 176, pp. 17.

144 B. Moslehi, J. W. Goodman, M. Tur, H. J. Shaw, "Fibre-optic lattice signal processing", vol. 72, no. 7, pp.909-931, 1984.

145 F. Coppinger, S. Yegnanarayanan, P. D. Trinh and B. Jalali, "All-optical incoherent negative taps for photonic signal processing," *Electron. Lett.*, vol. 33, pp. 973-975, 1997.

146 K. P. Jackson, S. A. Newton, B. Moslehi, M. Tur, C. C. Cutler, J. W. Goodman, and H. J. Shaw, "Optical fibre delay-line signal processing" *IEEE Trans. Microwave Theory Tech.*, vol. MTT-33, no. 3, pp 193-209, 1985.

147 M. Y. Frankel and R. D. Esman, "Fibre-optic Tuneable microwave transversal filter", *IEEE Photon. Tech. Lett.,* vol. 7, no. 2, pp 191-193, 1995.

148 D. Norton, S. Johns, C. Keefer and R. Soref, "Tuneable microwave filtering using high dispersion fibre time delays", *IEEE Photon. Tech. Lett.,* vol. 6, no. 7, pp 831-832, 1994.

149 J. Capmany, J. Cascon, J. L. Martin, S. Sales, D. Pastor, J. Marti, "Synthesis of fibre-optic delay line filters", *J. Lightwave Tech.,* vol. 13, no. 10, pp 2003-2012, 1992.

150 T. A. Cusick, S. Iezekiel, R. E. Miles, S. Sales, J. Capmany, "Synthesis of all-optical microwave filters using Mach-Zehnder lattices", *IEEE Trans. Microwave Theory Tech.*, vol. 45, no. 8, pp 1458-1461,1997.

151 J. Capmany and J. Cascon, "Direct form-I fibre-optic discrete-time signal processors using optical amplifiers and embedded Mach-Zehnder structures," *IEEE Photon. Tech. Lett.,* vol. 5, no. 7, pp 842-844, 1993.

152 R. A. Minasian, "Photonic signal processing of high-speed signals using fiber gratings," *Opt. Fiber Technol.* Vol. 6, pp. 91-108, 2000.

153 A. Molony, L. Zhang, J. A. R. Williams, I. Bennion, C. Edge, and J. Fells, "Fibre Bragg-grating true time-delay systems: Discrete-grating array 3-b delay-lines and chirped-grating 6-b delay lines," *IEEE Trans. Microwave Theory Tech.*, vol. 45, pp. 1527, 1997.

154 Y. Yoffe, K. Alameh, and R.Minasian, "Superposed WDM grating unit for short time delay processing of signals," *Microwave Opt. Technol. Lett.*, pp. 390, 2000.

155 W. Zhang and J. A. R. Williams, "Fibre optic bandpass transversal filter employing fibre grating arrays", *Electron. Lett.,*vol. 35, pp. 1010-1011, 1999.

156 J. Capmany, D. Pastor, and B. Ortega, "New and flexible fibre-optic delay-line filters using chirped Bragg gratings and laser arrays," *IEEE Trans. Microwave Theory Tech.*, vol. 47, pp. 1321-1326, 1999.

157 G. Yu, W. Zhang, J. A. R. Williams, "High-performance microwave transversal filter using fibre Bragg grating arrays," *IEEE Photon. Technol. Lett.*, vol. 12, pp. 1183-1185, 2000.

158 Y. J. Rao, "Recent progress in applications of in-fibre Bragg grating sensors," *Optics and Lasers in Engineering*, vol. 31, pp. 297-324, 1999.

159 F. Coppinger, S. Yegnanarayanan, P. D. Trinh and B. Jalali, "All-optical incoherent negative taps for photonic singnal processing," *Electro. Lett.*, Vol. 33, pp. 973-975, 1997.

160 I. Seto, T. Tomioka and S. Ohshima, "Error-free transmission of radio QPSK signals in an optical subcarrier multiple access system suppressing optical beat interference with over-modulation," *Proc. MWP 2000,* pp. 43-46, Oxford.

161 Y. Shoji and H. Ogawa, "Optical subcarrier multiplexing system using time sampling multiplexer to suppress optical beat interference," ," *Proc. MWP 2000,* pp. 47-50, Oxford.

162 M. Yamada and K. Sakuda, "Analysis of almost-periodic distributed feedback slab waveguides via a fundamental matrix approach," *Appl. Opt.,* Vol. 26, No. 16, pp. 3473-3478, 1987.